UNIVERSITY OF CALIFORNIA
RIVERSIDE

From Molecules to Devices: Using Small Molecules to Create Photomechanical Actuators

A Dissertation submitted in partial satisfaction
of the requirements for the degree of

Doctor of Philosophy

in

Chemistry

by

Brandon Lui

December 2022

Dissertation Committee:
Dr. Christopher J. Bardeen, Chairperson
Dr. James Davies
Dr. Jingsong Zhang

The Dissertation of Brandon Lui is approved:

_____

_____

_____

Committee Chairperson

University of California, Riverside

Acknowledgements

I would like to express my gratitude and appreciation for my PhD adviser, Christopher J. Bardeen. His mentorship, guidance, and patience greatly influenced the scientist that I am today. Over the past 5 years, I have spent many hours looking through the window in the hallway of Chemical Science to see if Chris was in his office. If he was, I would pop in to ask a question. He would always make time to answer my questions, no matter how busy he was or how trivial the question. Through our conversations at various stages in my academic career, he challenged me and taught me how to think critically. He has fundamentally changed the way I approach science, for the better. But beyond chemistry and through observations of his actions, he has taught me how to be more patient with challenging and difficult situations. One of the most important philosophies that Chris has imparted on me over the years is that nothing is a waste of time, so as long as you have learned something from it. For that, I thank him.

Dr. Kerry Hanson is the staff scientist of the Bardeen lab and had warmly welcomed me since my first day of joining the lab. She played an important role in my scientific development throughout my PhD career by providing feedback on my experiments, written reports, exams, etc. Beyond the professional realm, she is also a fantastic friend – I thank her for the conversations about film, pop culture, and various other topics we have shared throughout the years which broke up the monotony of work. I am grateful for both Chris and Kerry for being supportive of my goals and ambitions throughout my academic journey. This would not have been possible without the two of you.

I would like to thank all Bardeen lab members, past and present, for providing their comradery and friendship. To Dr. Fei Tong, Dr. Hossein Mostafavi, Dr. Xinning Claire Dong, Dr. Wangxiang Luke Li, Dr. Adam Berges, and Nathan Tierce: I thank you all for being my senior graduate students when I was a young and new student of the lab. You all have helped me succeed in the Bardeen lab, and for that I am grateful. I could only hope that I was as helpful for all the students that came after me as you all were for me. I would like to extend my gratitude towards Dr. Thomas Gately, Taylor Lewis, Touhid Bin Anwar, Jacob Rodriguez, Pranaya Ghate, Kevin Lam, Marielle Sewell, and Sophie Weiss for their digressions and conversations in lab.

To my dear friends and esteemed coworkers, Dr. Pablo Unzueta and Dr. Cameron Cook, I'd like to thank the two of you for all the times spent in and outside of lab. I will remember our walks to lunch and Spring break trips fondly. More importantly, I would like to express how privileged it was to have had the opportunity to grow along the two of you as a scientist and as a person. We have come a long way since our undergraduate studies together at Cal Poly Pomona. I know you two will be wildly successful in your future endeavors.

To my family: my mother and father, Elaine and Frank; my sister Jennifer, brother-in-law Benson, and nephew Jeremy, I thank you all for your patience and support while I set off on my journey in my PhD studies. I hope to repay it back some day. To my dogs Koda, Ellie, Marlin, Riley, and Meeko, I am grateful for their emotional support and their never-ending supply of positive energy.

Finally, to the reader, thank you for having spent your time reading this far. Beyond this section is my thesis – a collection of short stories that has defined me as a researcher thus far into my scientific career. I have spent the past 5 years submerged in the field of photochemistry and photophysics, making novel devices that transforms light into mechanical work. I hope you enjoy reading this as much as I enjoyed performing the experiments.

Some chapters in this dissertation are adapted from the following references:

Chapter 3:

Lui, B. F.; Tierce, N. T.; Tong, F.; Sroda, M. M.; Lu, H.; Read De Alaniz, J.; Bardeen, C. J. Unusual Concentration Dependence of the Photoisomerization Reaction in Donor-Acceptor Stenhouse Adducts. *Photochemical and Photobiological Sciences* **2019**, *18* (6), 1587–1595. https://doi.org/10.1039/c9pp00130a.

Chapter 4:

Lui, B. F.; Bardeen, C. J. Using Small Molecule Absorbers to Create a Photothermal Wax Motor. *Small* **2021**, *2105356*, 1–7. https://doi.org/10.1002/smll.202105356.

ABSTRACT OF THE DISSERTATION

From Molecules to Devices: Using Small Molecules to Create Photomechanical Actuators

by

Brandon Lui

Doctor of Philosophy, Chemistry
University of California, Riverside, December 2022
Dr. Christopher J. Bardeen, Chairperson

Photomechanical materials interact with light to elicit a mechanical response. They are the basis of a new class of smart materials which can serve as the active element in actuators, thus creating light-powered devices. The origin of the mechanical response is a volume change induced by a solid→solid or solid→liquid phase transition in the material. This light-induced volume change can be performed two different ways: through a photochemical reaction or through the photothermal effect. In this thesis, both pathways are discussed, and photomechanical actuation is demonstrated in piston-type actuators and polymer films. In Chapter 3, the photoisomerization kinetics of a third-generation donor acceptor Stenhouse adduct (DASA) are examined over a range of concentrations. DASAs are a novel photoswitch which absorb in the visible and near-infrared spectral regions. It switches efficiently at micromolar concentrations in both liquid solution and in polymers, but as the photochrome concentration is increased there is a dramatic inhibition of the photoisomerization. The physical origin of the inhibition of photoswitching at high

photochrome concentrations must be understood if the DASA class of molecules is to be used for applications like photomechanical actuation. In Chapter 4, a photothermal solid→liquid transition is studied because of its large volume expansion. Photoactive composites made of small molecules doped in a phase change material (PCM) are used in a commercial wax actuator to generate useful mechanical work. It is demonstrated that small molecules can act as absorbers to enable a photothermal solid→liquid melting transition in eicosane, a low molecular weight PCM. The stability, work density, and efficiency of the actuator containing these PCMs are investigated, and it is found that the actuators are competitive with electrically powered devices. In Chapter 5, further investigation of the small molecule-PCM composite is conducted using a custom-built actuator to gain insight on how the actuator should be optimized to maximize its work output. This new actuator consists of a simpler geometry which allows for the comparison with theoretical work density models. In Chapter 6, an azobenzene derivative (AZO) that can undergo photochemical melting at room temperature, is investigated as a potential candidate for photomechanical actuation. AZO is incorporated in a variety of polymer hosts to create thin films capable of bending when irradiated with light. We find that doping polymers with AZO can provide a general strategy to make photomechanical polymers using a reversible photochemical reaction that induces a solid→liquid phase transition.

Table of Contents

List of Figures

1. Introduction

1.1 Transforming photons to mechanical work: light-powered devices

Smart materials are materials whose properties can be altered by some external stimulus such as mechanical stress, temperature change, electrical or magnetic fields, pH, or light.[1] Of these stimuli, light is an attractive option because it is a noninvasive stimulant and can manipulate objects with high accuracy and without physical contact.[2] Much effort has been made to convert light, or photons, into renewable energy (e.g., solar cells, photovoltaics, etc.),[3] but photons can be directly converted into mechanical work through the photomechanical effect. The photomechanical effect is the conversion of photons to some physical deformation of the material like bending, twisting, peeling, expanding, or rolling.[4]

Currently, energy is transported by electrons or by chemical fuels. Photons are a low-loss way to transport energy, but there is no photonic analog to an electric motor, which converts electrons to work. Over the past decades there has been an increase of interest in =light-activated smart materials that can output mechanical work by deforming their shape due to the absorption of light. The benefit of using light for these applications is that these actuators and devices can be powered wirelessly and remotely, removing the need for physical connections.

1.2 Background of photochromic systems

Organic molecules can be synthetically modified to tune their spectral properties. They can also be tuned to undergo specific photochemical processes. Photochromic

molecules are molecules that undergo some sort of chemical change when exposed to light. In some cases, these changes can result in a deformation in the solid-state bulk material, which leads to a mechanical response. These molecules, often referred to as photoswitches, have been studied for their broad range of applications including molecular actuators,[5] drug delivery nanocarriers,[6] and data storage devices.[7] Some of the more valuable photoswitches are ones that could reversibly switch, which introduces an on/off mechanic; a desirable feature in certain applications (e.g., actuators). However, unidirectional chemical reactions have also been used to demonstrate photomechanical work.[8] Some examples of organic photoswitches that have been studied extensively are azobenzenes, spiropyrans, donor accepter Stenhouse adducts, and diarylethenes. These molecules demonstrate versatility and chemical stability, making them suitable candidates in the aforementioned applications.

Although the maturing field of photomechanical materials have made many advances in creating and characterizing light-powered devices throughout the past decade, there still remain some challenges in graduating these devices to be useful outside of a controlled research environment. There are gaps of knowledge in the literature on the optimization of an actuator's light-to-work efficiency, temporal response, and precision. The work done in this thesis aims to not only bridge these gaps, but to also create new materials and devices that allow photons to replace electrons. These materials' photochemistry and photophysics are characterized along with the work outputs, efficiencies, and response times of their respective actuators that are comprised of these light-activated molecules and composites.

1.3 Molecular photophysics

In the simplest case, a two-state model can be used to describe a photochemical reaction: **A→B** where **A** and **B** are arbitrary molecules. For a reversible reaction, the reaction is flipped, **B→A**. In the event that a photochemical reaction does not occur, the molecule that is excited from $S_0 \rightarrow S_n$ can relax back down to its initial ground state through a variety of photophysical mechanisms like internal conversion, phosphorescence, or fluorescence.[9] **Figure 1.1** illustrates an example of a Jablonski diagram with the different radiative and nonradiative photophysical pathways available.

The emission of a photon (luminescence) from an electronic excited state is divided into two categories: fluorescence and phosphorescence. Although both fluorescence and phosphorescence are classified as radiative processes due to the emission of light, they differ in that fluorescence is considered a spin-allowed process while phosphorescence is spin-forbidden. Starting at the ground state, a pair of electrons are spin up and spin down; upon excitation with light, one electron is excited to the excited state while maintaining its spin orientation. Since the spin of the electron in the excited state is opposite to that of the ground state, the relaxation to the ground state is a spin-allowed process and emission of a photon occurs (i.e., fluorescence). Emission lifetimes are typically on the scale of nanoseconds.[10] Although most fluorophores emit from the lowest energy excited state (S_1),[11] there are molecules that violate this rule and emit from the second excited state, S_2, such as azulene, derivatives of azulene, and azobenzene.[12–15]

Phosphorescence is the emission of a photon from the triplet T_1 state to ground state S_0. Similar to the start of the fluorescence process, upon excitation from $S_0 \rightarrow S_1$, the spin

of the electron pair in the ground state and excited state are opposite to that of each other. However, a spin flip occurs from S_1 to T_1 in a process called intersystem crossing (**Figure 1.1**, green arrow). From this T_1 state, the emission of a photon to the ground state is possible and is referred to as phosphorescence (**Figure 1.1**, orange arrow), though this process is spin-forbidden. As a result, the phosphorescence lifetimes are much longer compared to fluorescence and are on the order of milliseconds to seconds.[10]

Relaxation from an excited state without the emission of a photon is considered a nonradiative process. Examples of this include internal conversion and vibrational relaxation. The time scales of these processes are on the order of picoseconds, which are much faster than that of fluorescence and phosphorescence, so internal conversion is generally finished prior to emission of a photon. Molecules that undergo rapid internal conversion typically release an excess amount of heat into its local environment.

In special cases like in highly concentrated liquid samples or molecular solids, electronic interactions between nearby neighboring molecules can delocalize the excited states (exciton formation).[16] These interactions can form molecular aggregates which morph the excited state energy landscape, giving rise to different reactivities.[17] This can be detrimental for photomechanical purposes because often, photomechanical systems necessitate a high density or high concentration of photoswitches which propagates the mechanical response.

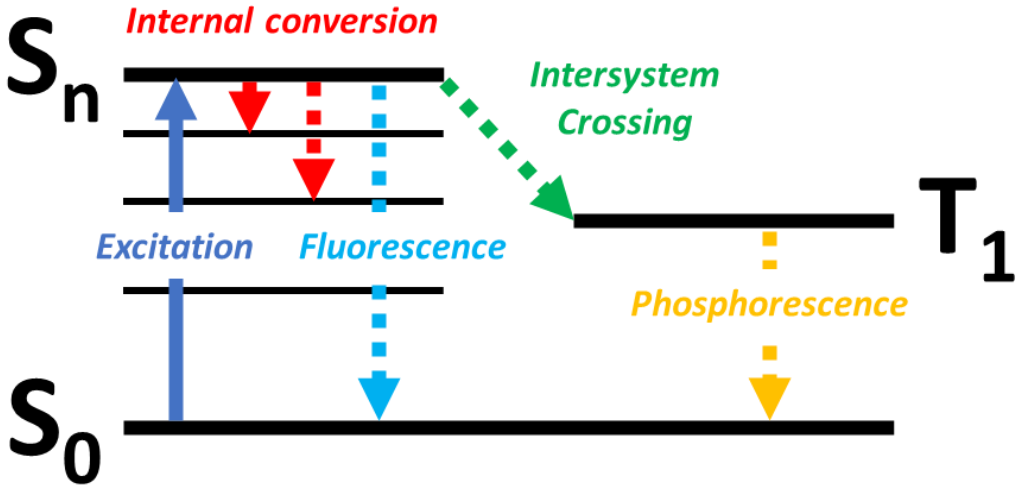

Figure 1.1 An example of a Jablonski diagram illustrating the different relaxation pathways back down from the S_n state: internal conversion from a singlet state (red), fluorescence from a singlet state (blue), intersystem crossing from a singlet to triplet state (green), and phosphorescence from a triplet to singlet state (yellow).

A common sign of aggregation is broadening of the steady-state absorption spectrum. This behavior can be rationalized using Kasha's model for molecular excitons.[18] From **Figure 1.2**, a binary example of two different aggregates is shown: H-aggregation and J-aggregation. Both molecular aggregates have access to different excited states that otherwise was not available to the monomer. In the case of H-aggregation, the dimers are cofacial (parallel) with one another, and what dictates an allowable transition is the phase of the oscillation of the dipoles of the individual monomers. When they are oscillating in-phase (i.e., the same direction), a transition is allowed – in the case of H-aggregation, the dipoles are in-phase when they are both up or both down. However, they experience large electron-electron repulsion, hence why there is a higher energy transition (blue shift). In

the case of J-aggregation, the dipoles are in-phase when they are lying head-to-tail; there is a smaller electron-electron repulsion interaction, hence a smaller energy transition (red shift) is observed.

Although only H and J-aggregation are shown in **Figure 1.2**, a combination of the two can exist where there are intermediate structures of the dimers (e.g., two monomers lying perpendicular to one another or rotated anywhere between 0-180°).

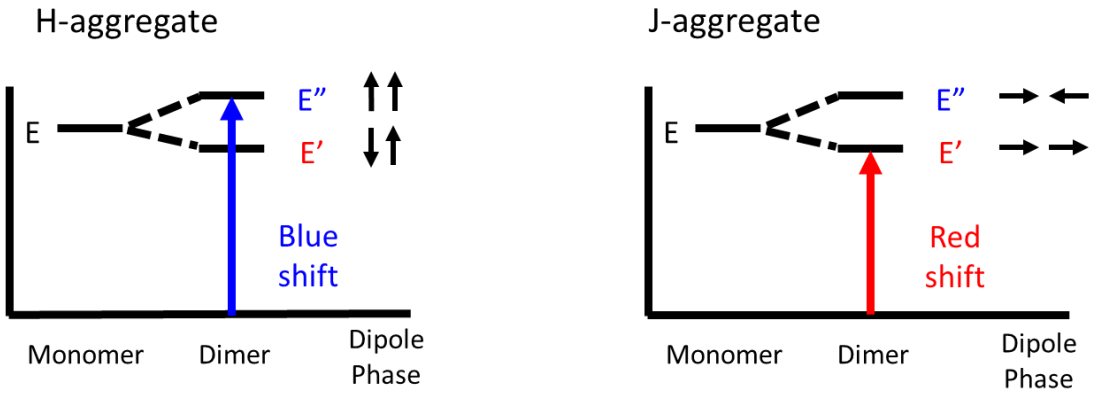

Figure 1.2 Selection rules for H- and J- aggregation. A blue shift to the higher energy singlet state, E”, is observed in H-aggregation due to the in-phase dipole vectors, i.e., the positive and negative ends of both dipoles lie complementary to each other. A red shift is observed (lower energy shift) for J-aggregation because the in-phase dipole vectors are lying head-to-tail and thus exhibit smaller electron-electron repulsion compared to H-aggregation.

1.4 Molecular photochemistry: reversible two-state photoswitches

Unlike the photophysical processes discussed in the previous section, a change in bonding occurs during a photochemical reaction. From **Figure 1.3**, when molecule **A** absorbs a photon, the molecule is excited from its ground state to some excited state (blue arrow, **Figure 1.3**). The electron then relaxes down to some crossing point (red arrow, **Figure 1.3**) and completes the reaction by relaxing to the ground state of molecule **B**

(purple arrow, **Figure 1.3**). Thus, a photochemical transformation occurs which results in the production of the photoproduct, **B**.[19] The reverse reaction, **B→A**, would follow the same mechanism.

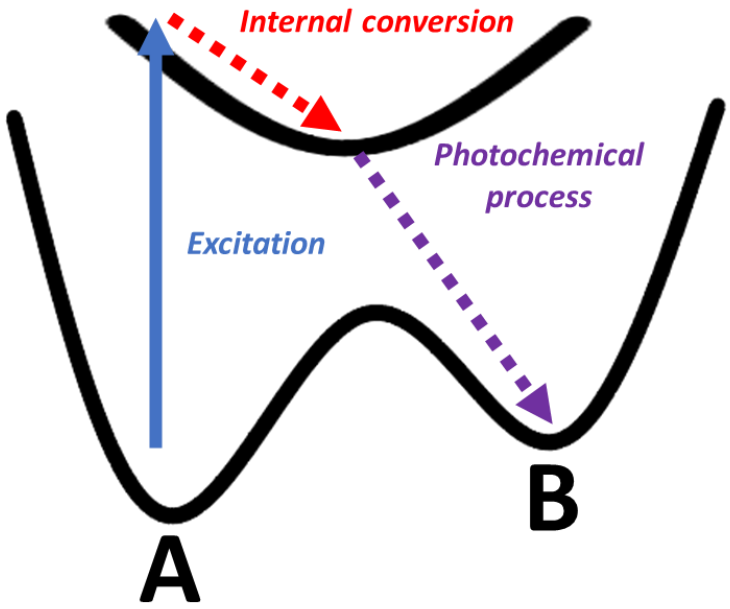

Figure 1.3 A schematic of a photochemical reaction of **A→B**. Upon excitation, the electron goes from the ground state of A to the excited state. It then arrives at a crossing point through internal conversion and then completes its reaction by relaxing to the ground state of **B**.

Reversible photoswitches fall in one of three categories: 1) Thermal (T-type), 2) Photon (P-type), or 3) Hybrid (P/T-type). Some examples of "two-state" or "single-step" switches are shown in **Figure 1.4**. These molecules undergo their forward and reverse reactions in separate and singular steps, hence their classification as "two-state" switches. T-type switches, like dihydroazulenes, uses light to induce a forward reaction but have a thermal back reaction.[20] P-type switches, like diarylethenes, are controlled entirely by

photons, which allows this class of photochromic molecules to have a photochemically reversible reaction.[21] Hybrid type switches, like azobenzenes, uses both mechanisms to reverse their reactions. They utilize light to induce a forward reaction but can undergo both a thermal *and* photochemical reversion back to the initial state.

In terms of potential industrial relevance, P-type and hybrid type switches have been studied extensively for these purposes owing to their high chemical stability and versatility.[22] Their chemical simplicity and structural stability make them suitable candidates for robust applications such as chemical sensors, data storage devices, and molecular machines.

1.5 Multistage photoswitches: donor accepter Stenhouse adducts

The two-state photoswitches mentioned in the previous section are relatively simple: the forward and reverse reactions are completed in single but separate steps. These switches have all been employed in a variety of applications due to their ability to change their volumes from a photochemical isomerization or dimerization reaction. However, the tradeoffs are that these volume expansions are not very large and these unique photoswitches require high energy UV light to propel their photochemical transformations. This inherently limits the applications of these molecules in biomedical applications and materials engineering due to the risk of photodegradation of materials from prolonged exposure to UV photons.

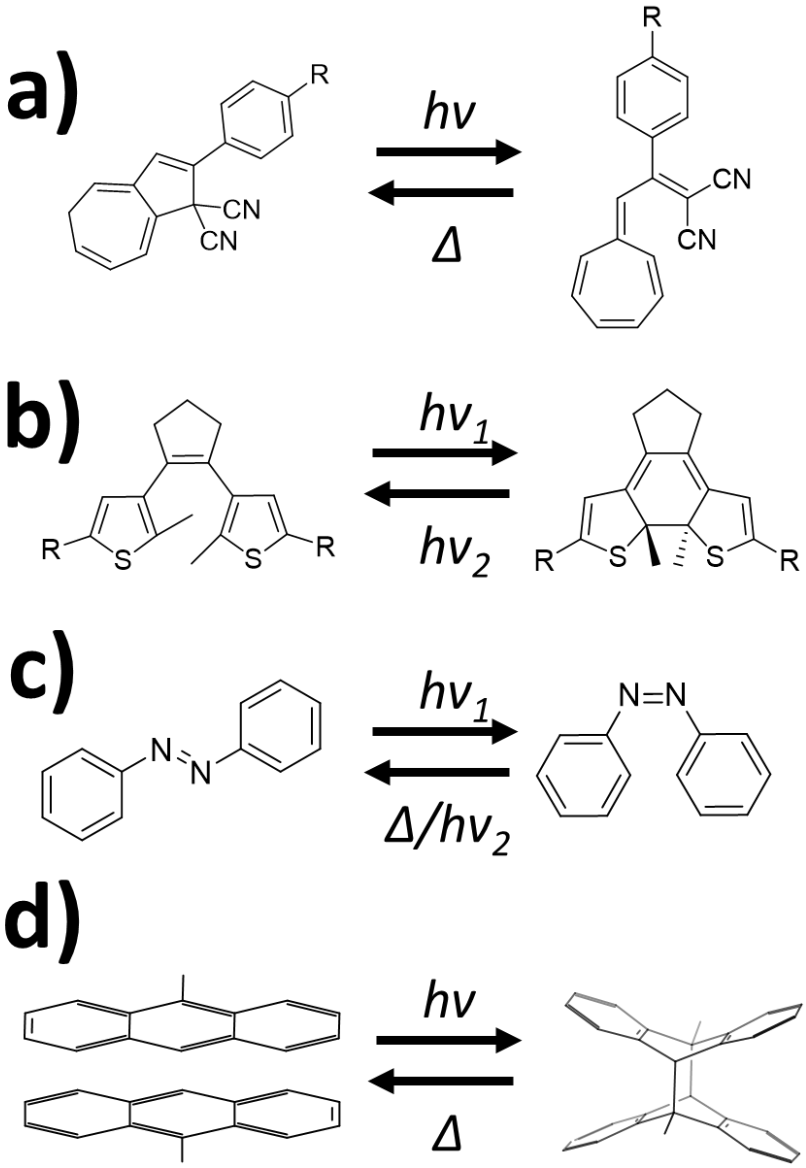

Figure 1.4 A collection of different types of reversible "two-state" photoswitches. **a)** Dihydroazulene, a T-type switch, undergoes a ring opening reaction upon irradiation with light but has a thermal back reaction. **b)** Diarylethene, a P-type switch, undergoes a ring opening and ring closing mechanism upon irradiation with two distinct wavelengths of light. **c)** Azobenzene, a hybrid type switch (P/T-type), undergoes a trans-cis isomerization upon exposure to light. It can revert back to the trans isomer using a different wavelength of light or with heat. **d)** 9-methylanthracene, a T-type switch, undergoes a [4+4] cycloaddition of two anthracene monomers.

The common strategy of circumventing the issues that the two-stage photoswitches face is to synthetically modify the existing library of photoswitches by attaching functional groups that red shift the absorption of these molecules into the visible region. However, a different approach has been taken where an entirely new class of molecules were synthesized and are activated by visible light.[23] These molecules, called donor acceptor Stenhouse adducts (DASAs), possess numerous attractive properties because they undergo reversible switching, display dramatic geometric and polarity changes, and exhibit negative photochromism (color→colorless change).[24]

DASA's unique multistage switching enables a large molecular volume contraction when it undergoes photochemistry. The multistep mechanism of a third generation DASA is shown in **Figure 1.5**. Briefly, DASA begins as a linear molecule. Upon absorption of a photon, the actinic step i.e., light involving step, is initiated. During this step, a Z→E isomerization along the C_2-C_3 bond occurs, followed by a thermal ground state C_3-C_4 bond rotation and 4π electrocyclization to finish the reaction. In this final phase of electrocyclization, DASA is in a radically different geometry: it is a smaller, bicyclic structure compared to its initial larger linear form. Although there exist some subtle differences in functional groups and kinetic rates among the different generations of DASAs, this mechanism is general for this family of molecules.[25–27]

DASA's various intermediates can be monitored using ultrafast spectroscopic methods in conjunction with computational chemistry,[17,25,26,28] but the detailed mechanistic understanding of the excited state processes which trigger the different reactive pathways is still being heavily investigated. DASAs are known to have inhibited reactivities in high

concentrations[17] and are sensitive to ionic concentrations in its local environment.[29] Although photothermal actuation has been demonstrated with DASAs before, it was found that the incorporation of DASAs was not the major contributing factor in the photomechanical behavior.[30] With all the attractive properties that DASA possesses from its large shape change to its chemical reversibility, it would be beneficial to understand and to be able to tune its photochemistry so that DASA may be added to the photomechanical toolbox.

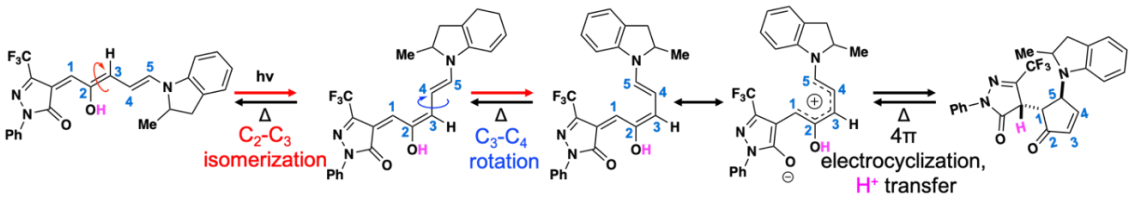

Figure 1.5 The photoisomerization of a third generation DASA molecule. The reaction is initiated by the absorption of a photon and a Z→E isomerization along the C_2-C_3 bond occurs, followed by a thermal C_3-C_4 rotation and 4π electrocyclization.[17] (Reproduced with the permission of Springer Nature).

1.6 Photomechanical systems: translating molecular motion to macroscopic movement

The conversion of light (photons) to mechanical work is defined as photomechanical work. The most common way to achieve photomechanical work is through a solid→solid phase transition via a photochemical reaction, but phase transitions can also be induced by increasing the temperature of a material using photons through the photothermal effect. Regardless of whichever method is used to induce a phase transition, the method of action is the same: volume expansion or contraction is the driving force of the actuation.

In the case of photochemical actuation, light is used to propagate a mechanical response via a photochemical reaction. For example, in diarylethene molecular crystals (**Figure 1.4b**), photoisomerization drives anisotropic expansion in the crystal lattice which translates to macroscopic expansion in the bulk crystal.[31] 9-methylanthracene (**Figure 1.4d**) dimerizes upon excitation with UV light and the crystal structure is deformed, driving expansion in a single plane of the crystal lattice.[32] So the mechanism for photochemical actuation can be summarized as some chemical bonding change which dramatically alters the material's bulk properties.

The areas where photochemistry would be most useful is if the application is in an extreme environment or under extreme conditions, e.g., underwater or in outer space, where it may be difficult to deliver heat or electricity to the system. Photoreactive molecules could be cleverly patterned into distinct shapes or arrays using photolithography to create smart displays or interfaces that can be selectively turned "on" or "off" depending on the area or irradiation.[33,34] An additional benefit of a photochemical reaction is that it is a faster process (femtoseconds – picoseconds) compared to thermal relaxation (picoseconds).[10] However, correlation of a molecule's photochemical transformation and its bulk material response must be investigated further to make conclusive claims about the speed of a photochemical-mechanical response.

In the case of photothermal actuation, the benefit is that heat can be passively diffused or dissipated over larger distances and areas compared to photons, which require uninterrupted interfacing between the light source and the active material. A smaller area could be illuminated with a laser source and thermal dissipation can be exploited to melt

the surrounding material without the need to deliver photons directly to the specific area. This distinct advantage that the photothermal effect possesses could be used to induce phase changes in bulk materials (~centimeter pathlengths) that far exceeds the optical penetration possible for positive photochromic reactions (submicron pathlengths), which are inherently limited by the optical properties of the materials itself. Such large discrepancies in the volume of materials undergoing a phase change directly effects the work output; photothermal actuation typically realizes larger volume expansion due to the fact that more of the active material is being melted.

1.6.1 Solid→solid photochemical phase transitions: molecular crystals

Some photochemical transformations can result in a mechanical response in the solid-state bulk material. In most cases the photochemical "engine" is embedded in a host matrix, often a polymer network,[35] an ordered composite,[31] or gel-like structure.[36] Another pathway of achieving photomechanical work is using molecular crystals by themselves, which circumvents the need to embed the active material inside of a host matrix.[37] In principle, this would have the highest mechanical work output because the system does not have to deform an inert matrix or casing. It is assumed that the work density is directly related to the density or concentration of molecules in the material, thus the more molecules there are, the higher the work output.[2]

In the most ideal case, a photomechanical system would be a dense molecular crystal in which the molecules undergo large geometric or volumetric deformations, which result in dramatic macroscopic changes. This expansion along a single crystal lattice causes contraction on another, which causes strain within the crystal and ultimately deforms the

bulk material and produces work. These crystals can expand from as little as 0.1% to as high as 43%.[31,38] **Figure 1.6** demonstrates both template-assisted photomechanical work output and molecular crystals themselves expanding and morphing the bulk structure. In both cases, anisotropic expansion is observed along a specific crystal axis, therefore the work output is sensitive to the crystal orientation.

However, the use of photomechanical molecular crystals has limited actuating capabilities due to some practical reasons. First, growing large crystals is both difficult and time consuming. Second, larger crystals tend to shatter due to the internal strain/stress created by the photochemical reaction, which overcome the weak intermolecular interactions (i.e., van der Waals interaction or hydrogen bonds) that hold the crystal together. And lastly, orienting the crystals in a cooperative fashion to achieve photomechanical work is a challenging endeavor.[39] Nevertheless, these molecular crystals are still studied for their potential in optoelectronics, optophotonics, and metamaterials.[40]

1.6.2 Solid→liquid phase change materials: photochemical phase transitions

In the case where an isotropic volumetric expansion is desired, solid→liquid photochemical phase change materials (PCMs) can be utilized. There have been recent studies that have made progress in synthesizing photochemical PCMs and utilizing them in applications such as actuation and energy storage devices.[41–43] The benefit of using a solid→liquid transformation is that liquids are often less dense, thus eliciting a larger volume expansion. However, a couple of shortcomings of photochemically driven solid→liquid transformations include difficulty of achieving deep optical penetration to reach high conversion rates and controlling the isotropic transformation of the phase

change. Most recent work in regard to synthesizing photochemical PCMs involve using azobenzene as the parent structure and some examples of the transformations are seen in **Figure 1.7**.

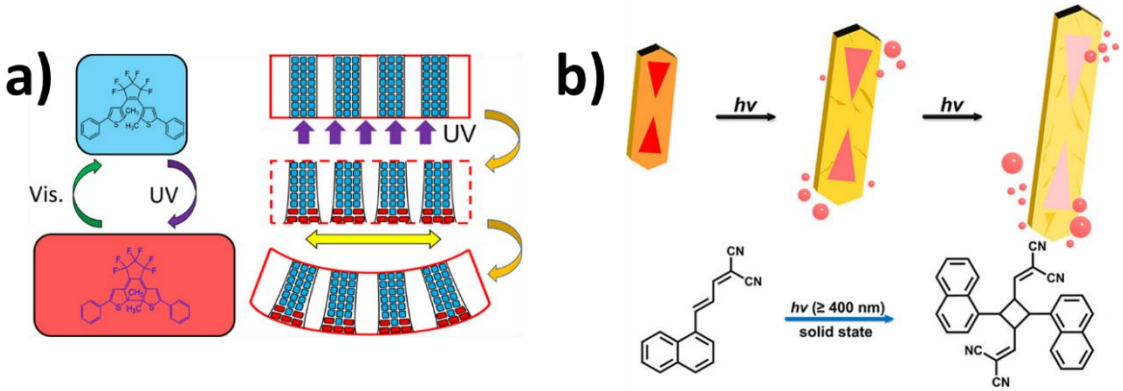

Figure 1.6 a) 1,2-bis(2- methyl-5-phenyl-3-thienyl)perfluorocyclopentene nanorods that undergo a ring-opening and ring-closing photoisomerization reaction. The ring-closed isomer is larger than the ring-opened form, which are embedded inside an inorganic template.[31] The template deforms due to the asymmetric expansion of the photoproduct. **b)** (E)-3-(naphthalen-1-yl)acrylaldehyde malononitrile undergoes a [2+2] photocycloaddition reaction and dramatic directional expansion is observed in the microcrystals grown from this photochrome.[38] (Reproduced with the permission of American Chemical Society).

Azobenzene has a long history of being the photochemical engine for many photoactive materials, and thus many synthetic modifications have been explored to tune the properties of azobenzene derivatives.[22] It is worth noting that neat azobenzene (**Figure 1.4c**) is incapable of completing its trans-cis isomerization in the solid crystalline state due to steric hinderance. To avoid this issue, a methyl[44,45] or ethyl[42] group can be added at the meta position on one of the phenyl rings to change the crystal packing to allow for the isomerization in the solid state. The mechanism for a photochemical melt differs from the solid→solid transformations mentioned in **section 1.6** in that the intermolecular forces holding the crystal together (e.g., van der Waals forces, hydrogen bonds, etc.) are disrupted

when the photochemistry occurs, and the crystal liquefies. So, although many variants of azobenzene-based photomeltable materials exist, none of their physicochemical properties have been characterized extensively and perhaps another photoswitch may serve as a better basis for such applications (e.g., diarylethenes, DASAs, spiropyrans, etc.).

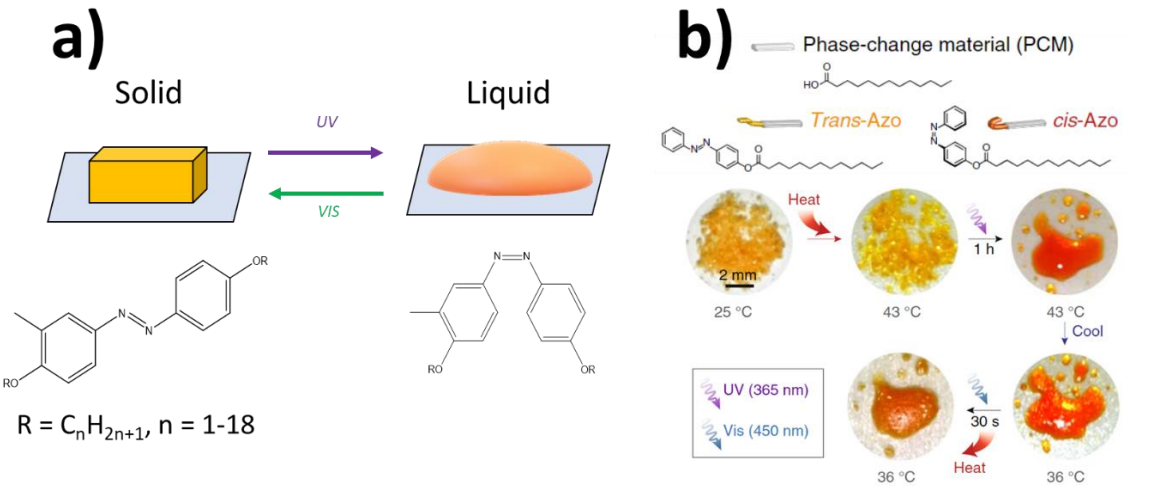

Figure 1.7 Some azobenzene derivatives that can undergo photochemical melts. **a)** an alkoxy azobenzene derivative synthesized by Norikane et al. which can undergo reversible liquefication.[44] (Image adapted and reproduced with the permission of the Society of Photopolymer Science and Technology). **b)** An azobenzene derivative with a tridecanoic acid tail synthesized by Han et al. undergoing reversible liquefication.[46] (Adapted and reproduced with the permission of Spring Nature).

1.6.3 Solid→liquid phase change materials: photothermal phase transitions and waxes

Lastly, the photothermal effect can also be used to induce a solid→liquid phase transition to promote photomechanical work. The photothermal effect differs from a photochemical reaction in that no chemical reaction occurs upon absorption of a photon. Instead, some absorber interacts with the incoming photon upon laser excitation and the electron is promoted to an excited state but relaxes back down through a nonradiative pathway, like internal conversion or vibrational relaxation (**Figure 1.1**). This releases heat

into the environment, which changes the intermolecular interaction in the crystal (in which the dopant is embedded in) and melts the solid. Photothermal solid→solid transitions have been demonstrated previously in polymer and semiconductor systems.[47] However, as mentioned previously, liquids are often less dense than their solid counterparts and the solid→liquid volume expansions may be used to produce useful mechanical work.

An example of this is the use of alkane solids like waxes, a common and commercially available PCM. Waxes have the benefit of larger volume expansions in comparison to molecular crystals. These waxes are chemically simplistic and follow the chemical formula C_nH_{2n+2}. They begin in a hexagonal packing (where n = odd number) or orthorhombic packing (where n = even number). When these waxes are heated, they undergo a solid→solid transition, as shown in **Figure 1.8**.[48] Further heating to the melting point, the wax will then undergo a solid→liquid phase transition and expands 10~15% of its initial volume.[49]

The origin of this large volume expansion can be rationalized that these long alkane chains have many degrees of freedom[50] and the volume that the alkyl chains occupy in the liquid phase are much larger that of the solid. This isotropic expansion from solid to liquid can be harnessed to produce mechanical work by compressing the liquid, similar to that of a hydraulic piston.[51–55] The resolidification behavior of waxes are also well documented,[56] demonstrating the robustness of the material as well as the cyclability of these PCMs as active elements in an actuator. However, since these alkane PCMs liquefy, a secondary container is necessary to utilize its actuating capabilities, else the liquid would flow into its surroundings, and the active material is not recoverable. The actuation is also limited by

its containment system, unlike molecular crystals which can be used directly as the active element.

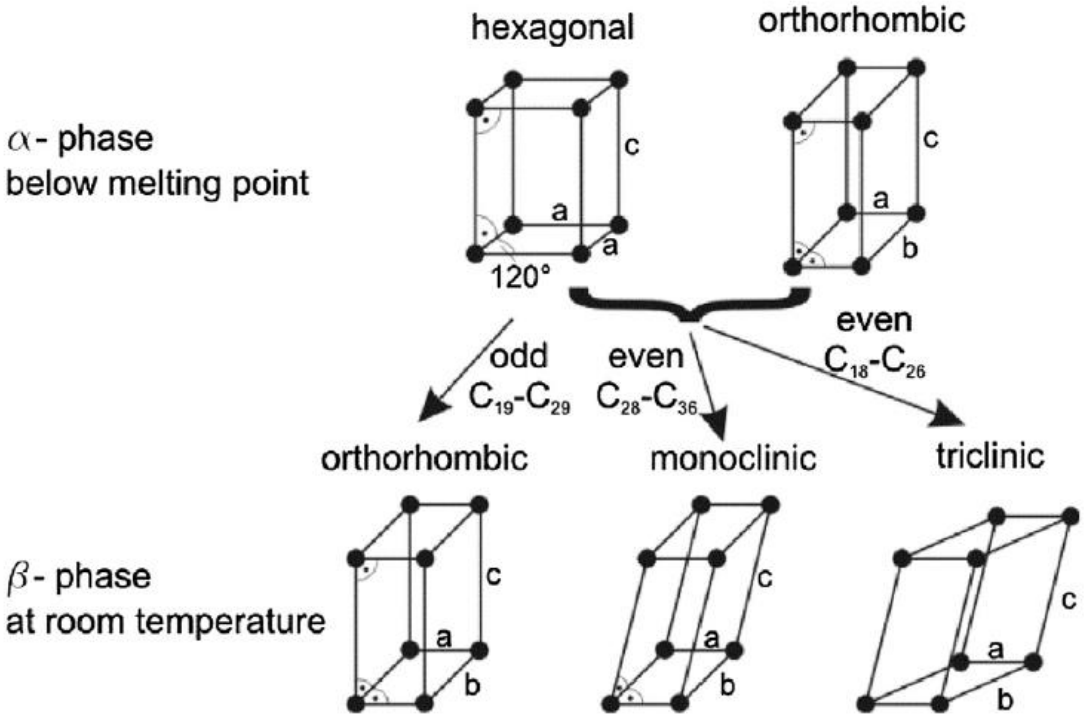

Figure 1.8 Solid→solid changes in crystal structure of even and odd numbered alkane solids. For solids that follow C_nH_{2n+2}, structures where n = 18-26 and is an even number transforms to triclinic. For n = 28-36 and is an even number, the structure transforms to monoclinic. For odd numbered n, the structure transforms to orthorhombic.[48] (Reproduced with the permission of Elsevier).

These waxes are encased in a container to create wax motors and the pressure generated from its solid→liquid expansion produces work.[51] In some cases, these wax motors can be adapted so that the PCM inside can be optically melted, thus producing photomechanical work.[53] The design and method of action for these actuators are discussed in more detail in **section 1.8**.

Figure 1.9 Multiwalled carbon nanotubes (MWCNTs) dispersed in paraffin wax. After 5 melt and resolidification cycles, the MWCNTs show a distinct separation and settle at the bottom of the container while the paraffin remains on top.[57] (Adapted and reproduced with the permission of Springer Nature).

To generate the temperature increase needed for melting, the waxes can be doped with nanoparticles[57,58] or small molecule dyes,[53] which allow the wax composites to absorb visible to near infrared (NIR) light. The resulting composite can then undergo the solid→liquid phase change via the photothermal effect. However, there are disadvantages in using nanoparticles as the photothermal agent since there have been reports of phase separation of the nanoparticles out from the host material, as seen in **Figure 1.9**. Small molecules, on the other hand, are much smaller than nanoparticles and are believed to reside in the interstitial lamellar regions of the alkane matrix of waxes.[59] Thus, when the small molecule-wax composites are thermally cycled, there is no phase separation and no loss of chemical stability of the composites themselves, even in highly concentrated samples (millimolar regime). **Figure 1.10** illustrates the effects of doping with small molecules and nanoparticles in alkane solids and how the smaller sized molecules are advantageous.

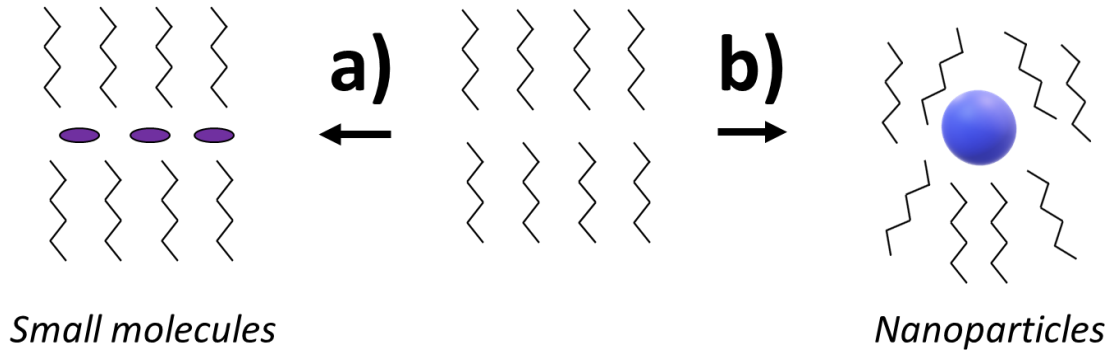

Figure 1.10 Doping of **a)** small molecules and **b)** nanoparticles in alkane matrices. In the case of small molecules, the molecules are small enough to lie in the interstitial regions of the solid while nanoparticles are much larger, thus disrupts the packing of the alkane chains, and over time will cause phase separation between the nanoparticles and the alkane chains.

1.7 Small molecule dopants as photothermal agents

As described above, small molecules are the ideal candidates for photothermal agents as they are resistant to phase separation from their alkane hosts. However, the challenge arises in selecting compatible molecules that are soluble in these alkane solids and liquids. From solubility rules, solute-solvent interactions must be acknowledged i.e., the intermolecular forces between the solute and solvent must be similar.[60] Waxes and other linear alkane hosts are nonpolar, where the dominant intermolecular forces are van der Waals forces. Molecules that are compatible in these alkane hosts must not be dominated by other intermolecular forces like hydrogen bonds, ionic bonds, etc., so the molecules chosen must be nonpolar as well.

In addition to the solute-solvent interaction, the size of the molecule and photophysical behavior must be considered. Low molecular weight small molecules (<200 g/mol) are preferred as they can be dissolved in high concentrations (>millimolar),[53] though from our work, larger molecules like perylene and Lumogen Orange have been shown to

be soluble in small quantities (<2×10^{-4} M). Since the heat output needs to be maximized to exceed the melting point of the alkane host, a small $S_0 \rightarrow S_1$ transition is also desirable as this often promotes fast internal conversion.[61] A smaller $S_0 \rightarrow S_1$ gap also allows for the use of laser diodes in 405 – 900 nm as the excitation source, which are commercially available and relatively inexpensive. Other photophysical and photochemical pathways like fluorescence or photoisomerization are not frequently sought out because the input photons would not produce heat efficiently. With all these properties considered, molecules like azobenzene, azulene, guaiazulene, and (2,2,6,6-tetramethylpiperidin-1-yl)oxidanyl (TEMPO) have been chosen to demonstrate remarkable photothermal behavior.[53] Though this is not an exhaustive list of molecules that are compatible with photothermal applications, this provides a basis of what is considered ideal.

1.8 Wax motors: a practical way to generate photomechanical work

Wax motors are linear actuators that take thermal energy, often passively from its surroundings, and converts it to mechanical energy. These closed containment systems with flexible diaphragms are built to contain the solid→liquid expansion of waxes. Such devices have a variety of applications in commercial and private sectors, ranging from controlling the dish soap containment in dishwashers to controlling crucial hydraulic applications in modern airplanes and space craft.[62] As mentioned previously, these actuators take advantage of the large volume expansions of waxes to generate mechanical work; two designs are shown in **Figure 1.11**.

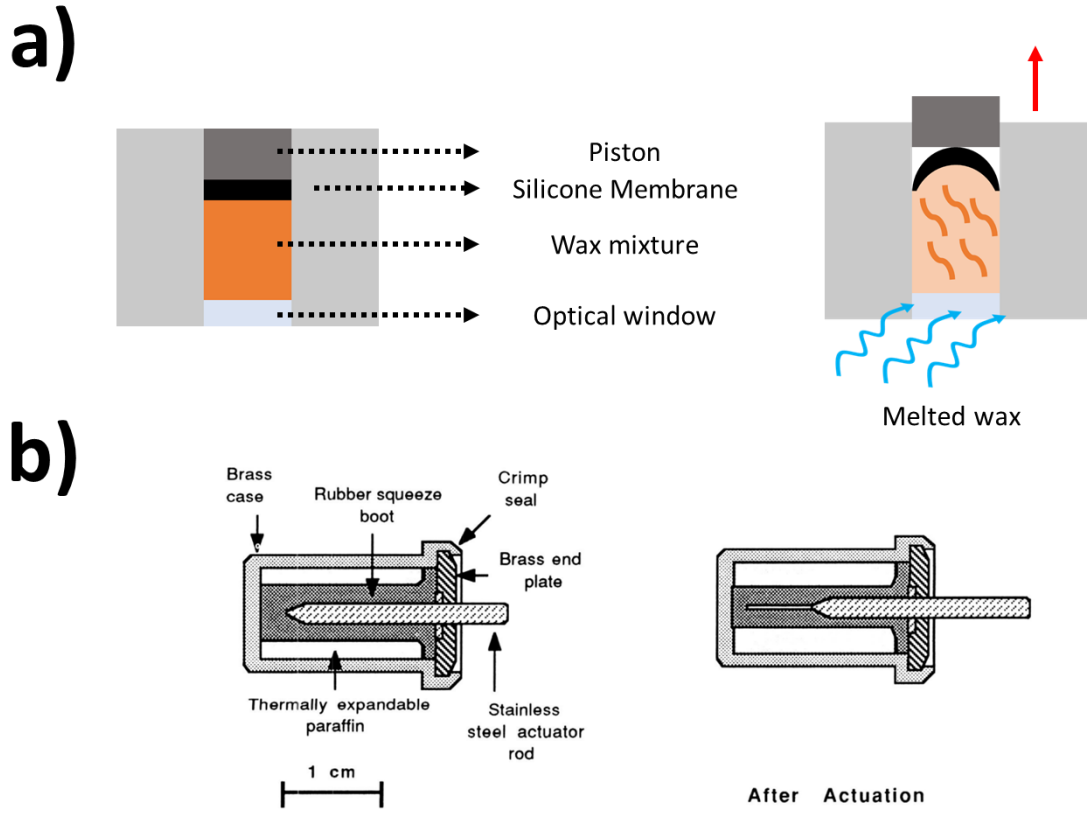

Figure 1.11 Sample designs of different types of wax motors. **a)** Illustrates an actuator with an optical window attached to the bottom. When the wax is irradiated with a laser, it melts, and the piston extends upward. **b)** A wax motor which relies on passive thermal energy to promote its phase transition and actuation. The actuator is strategically placed so that heat can transfer from its surroundings into the housing to melt the wax. In both cases, when the melt occurs, the diaphragm is compressed or the membrane expands and the piston is pushed outwards, creating a mechanical stroke. (Reproduced with the permission of the US government).[62]

These wax motors possess a large work density (approximately 9 MJ/m^3)[63] and are relatively simplistic to integrate into industrial applications. Actuators that are functionally comparable, like piezoelectrics, thermoneumatics, and muscle-like actuators, report work densities in the range of 0.02 – 1 MJ/m^3,[64] which is much smaller in comparison to wax's solid→liquid work density. Those devices are also limited by their size, whereas wax

motors are scalable from micrometers to centimeter size scales. Factoring in that wax motors are robust and can be thermally cycled many times, they distinguish themselves as attractive candidates for further investigation as light-powered devices.

Adapting the designs from preexisting wax motors, an optically powered wax motor was created by attaching a borosilicate window to a slightly modified version of **Figure 1.11b**.[53] This adaptation places a visual port on the bottom of the actuator and allows illumination from the bottom-up to melt the wax placed inside. **Figure 1.12** shows the light-powered wax motor filled with an eicosane-guaiazulene mixture as the photothermal agent. Some technical challenges that arose in fabricating these custom wax motors include issues with filling and sealing these actuators properly; since the wax inside liquefies, Viton O-rings had to be positioned so that the liquid was contained during the actuation stage. Evacuating any air bubbles inside the reservoir chamber was also a crucial task: since the residual air inside the actuator may act as void spaces for the wax to expand into and hinder any expansion against the membrane, precaution had to be taken to remove any excess air. Lastly, it was necessary to find a membrane that was not only chemically resistant to the liquid wax and small molecules, but also flexible and resistant to tearing upon expansion of the wax.

A major result of this thesis is the creation of a light-powered actuator based on the wax motor concept. The actuation can be triggered on demand by turning a laser on to melt the wax and promote actuation. The experimentally measured work density of these light driven wax motors ranges from 0.048 – 0.14 MJ/m^3, which is better than piezoelectrics and other soft actuators,[65–67] but is still 100 times smaller than the proposed maximum work

density by Srinivasan and Spearing.[63] Additionally, the light-to-work efficiency of the work output can also be calculated by dividing the total work output divided by the laser energy input, giving an efficiency of $9.1\times10^{-4}\%$.[53] The efficiency, temporal response, comparisons to electrical heating, and work output of similar actuators are currently being evaluated so that continuous improvements could be made in this regime of light-powered machines.

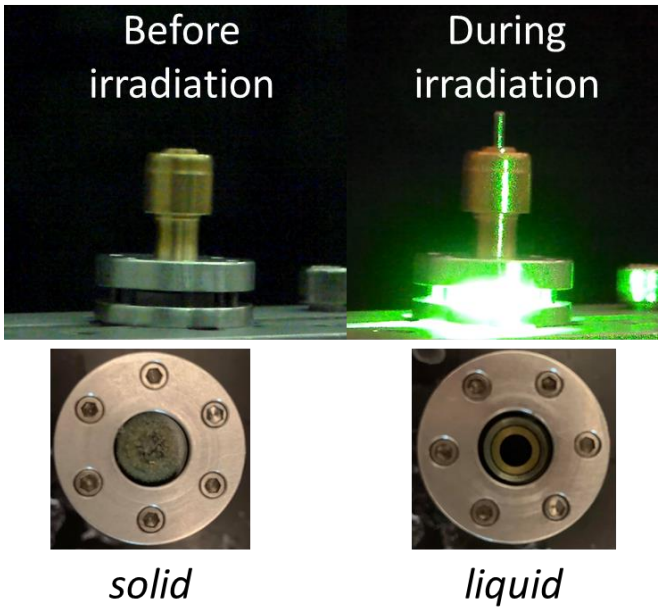

Figure 1.12 Top images are still photos of the adapted actuators in its "off" (left) and "on" (right) state. Bottom images show the wax before the melt (left) and after the melt (right).[53] (Reproduced with the permission of John Wiley and Sons).

1.9 Summary

Photomechanical actuation has been introduced as a next generation smart material that uses photons to replace electrons. Two methods of inducing photomechanical effects were discussed: 1) a photochemical reaction and 2) the photothermal effect; both have their

advantages, depending on the application of the device. The challenges that must be addressed for these devices to be useful outside of a controlled research environment include maximizing the actuator's light-to-work efficiency, controlling the temporal response of actuation, and having continuous control of the extent of actuation. This thesis provides the framework of creating novel photoresponsive composites which utilizes both photochemical and photothermal effects to propagate photomechanical work.

The research accomplishments are described in Chapters 3-5. In Chapter 3, the photochemistry of molecules like DASA is studied and its concentration dependent switching is discussed in both solid and liquid environments. DASA's potential as a photochemical solid→solid phase change material is dependent on its ability to switch in the solid state, so this behavior must be understood if DASA is to be incorporated in the photomechanical molecular toolbox. In Chapter 4, guaiazulene, azobenzene, and TEMPO are discussed as small molecule photothermal candidates which convert photons into thermal energy. These molecules are doped inside of eicosane, a wax, and these composites are incorporated inside custom built light-powered actuators. The volume expansions of these composites are then harnessed in wax motors which are designed to house and contain the solid→liquid transformation of these wax composites. Lastly, the work outputs, efficiencies, and direct comparisons to conventional convection heating are discussed in Chapter 5 to highlight the efficacy of using photons to power traditional electric actuators.

1.10 References

(1) Drossel, W. G.; Kunze, H.; Bucht, A.; Weisheit, L.; Pagel, K. Smart3 – Smart Materials for Smart Applications. *Procedia CIRP* **2015**, *36*, 211–216. https://doi.org/10.1016/J.PROCIR.2015.01.055.

(2) Kim, T.; Zhu, L.; Al-Kaysi, R. O.; Bardeen, C. J. Organic Photomechanical Materials. *ChemPhysChem* **2014**, *15* (3), 400–414. https://doi.org/10.1002/cphc.201300906.

(3) Hou, Y.; Vidu, R.; Stroeve, P. Solar Energy Storage Methods. *Ind Eng Chem Res* **2011**, *50* (15), 8954–8964. https://doi.org/10.1021/IE2003413.

(4) Tong, F.; Qu, D.-H. Engineering Shapes and Sizes of Molecular Crystals to Achieve Versatile Photomechanical Behaviors. *Langmuir* **2022**, *38* (16), 4793–4801. https://doi.org/10.1021/acs.langmuir.2c00414.

(5) Aßhoff, S. J.; Lancia, F.; Iamsaard, S.; Matt, B.; Kudernac, T.; Fletcher, S. P.; Katsonis, N. High-Power Actuation from Molecular Photoswitches in Enantiomerically Paired Soft Springs. *Angewandte Chemie - International Edition* **2017**, *56* (12), 3261–3265. https://doi.org/10.1002/anie.201611325.

(6) Liu, G.; Liu, W.; Dong, C. M. UV- and NIR-Responsive Polymeric Nanomedicines for on-Demand Drug Delivery. *Polym Chem* **2013**, *4* (12), 3431–3443. https://doi.org/10.1039/c3py21121e.

(7) Chan, J. C. H.; Lam, W. H.; Yam, V. W. W. A Highly Efficient Silole-Containing Dithienylethene with Excellent Thermal Stability and Fatigue Resistance: A Promising Candidate for Optical Memory Storage Materials. *J Am Chem Soc* **2014**, *136* (49), 16994–16997. https://doi.org/10.1021/ja5101855.

(8) Tong, F.; Xu, W.; Guo, T.; Lui, B. F.; Hayward, R. C.; Palffy-Muhoray, P.; Al-Kaysi, R. O.; Bardeen, C. J. Photomechanical Molecular Crystals and Nanowire Assemblies Based on the [2+2] Photodimerization of a Phenylbutadiene Derivative. *J Mater Chem C Mater* **2020**, *8* (15), 5036–5044. https://doi.org/10.1039/c9tc06946a.

(9) Franck, J.; Livingston, R. Remarks on the Fluorescence, Phosphorescence and Photochemistry of Dyestuffs. *J Chem Phys* **1941**, *9* (2), 184–190. https://doi.org/10.1063/1.1750873.

(10) Lakowicz, J. R. Introduction to Fluorescence. In *Principles of Fluorescence Spectroscopy*; Lakowicz, J. R., Ed.; Springer US: Boston, MA, 1999; pp 1–23. https://doi.org/10.1007/978-1-4757-3061-6_1.

(11) Kasha, M. Characterization of Electronic Transitions in Complex Molecules. *Discuss Faraday Soc* **1950**, *9*, 14–19. https://doi.org/https://doi.org/10.1039/DF9500900014.

(12) Michl, J.; Thulstrup, E. W. Why Is Azulene Blue and Anthracene White? A Simple Mo Picture. *Tetrahedron* **1976**, *32* (2), 205–209. https://doi.org/https://doi.org/10.1016/0040-4020(76)87002-0.

(13) del Valle, J. C.; Catalán, J. Kasha's Rule: A Reappraisal. *Physical Chemistry Chemical Physics* **2019**, *21* (19), 10061–10069. https://doi.org/10.1039/c9cp00739c.

(14) Fiori, J.; Gotti, R.; Albini, A.; Cavrini, V. Study on the Photostability of Guaiazulene by High-Performance Liquid Chromatography/Mass Spectrometry and Gas Chromatography/Mass Spectrometry. *Rapid Communications in Mass Spectrometry* **2008**, *22* (17), 2698–2706. https://doi.org/10.1002/rcm.3661.

(15) Fujino, T.; Arzhantsev, S. Yu.; Tahara, T. Femtosecond Time-Resolved Fluorescence Study of Photoisomerization of Trans-Azobenzene. *J Phys Chem A* **2001**, *105* (35), 8123–8129. https://doi.org/10.1021/jp0110713.

(16) Al-Kaysi, R. O.; Sang Ahn, T.; Müller, A. M.; Bardeen, C. J. The Photophysical Properties of Chromophores at High (100 MM and above) Concentrations in Polymers and as Neat Solids. *Physical Chemistry Chemical Physics* **2006**, *8* (29), 3453–3459. https://doi.org/10.1039/B605925B.

(17) Lui, B. F.; Tierce, N. T.; Tong, F.; Sroda, M. M.; Lu, H.; Read De Alaniz, J.; Bardeen, C. J. Unusual Concentration Dependence of the Photoisomerization Reaction in Donor-Acceptor Stenhouse Adducts. *Photochemical and Photobiological Sciences* **2019**, *18* (6), 1587–1595. https://doi.org/10.1039/c9pp00130a.

(18) Kasha, M.; Rawls, H. R.; El-Bayoumi, M. A. The Exciton Model In Molecular Spectroscopy. *Pure and Applied Chemistry* **1965**, *11* (3–4), 371–392. https://doi.org/10.1351/pac196511030371.

(19) Mai, S.; Gonzµlez, L. Molecular Photochemistry:Recent Developments in Theory. https://doi.org/10.1002/anie.201916381.

(20) Han, Y.; Hamada, M.; Chang, I. Y.; Hyeon-Deuk, K.; Kobori, Y.; Kobayashi, Y. Fast T-Type Photochromism of Colloidal Cu-Doped ZnS Nanocrystals. *J Am Chem Soc* **2021**, *143* (5), 2239–2249. https://doi.org/10.1021/jacs.0c10236.

(21) Frigoli, M.; Marrot, J.; Gentili, P. L.; Jacquemin, D.; Vagnini, M.; Pannacci, D.; Ortica, F. P-Type Photochromism of New Helical Naphthopyrans: Synthesis and

Photochemical, Photophysical and Theoretical Study. *ChemPhysChem* **2015**, *16* (11), 2447–2458. https://doi.org/10.1002/cphc.201500251.

(22) Fedele, C.; Ruoko, T.-P.; Kuntze, K.; Virkki, M.; Priimagi, A. New Tricks and Emerging Applications from Contemporary Azobenzene Research. *Photochemical & Photobiological Sciences 1*, 3. https://doi.org/10.1007/s43630-022-00262-8.

(23) Helmy, S.; Leibfarth, F. A.; Oh, S.; Poelma, J. E.; Hawker, C. J.; de Alaniz, J. R. Photoswitching Using Visible Light: A New Class of Organic Photochromic Molecules. *J Am Chem Soc* **2014**, *136* (23), 8169–8172. https://doi.org/10.1021/ja503016b.

(24) Helmy, S.; Oh, S.; Leibfarth, F. A.; Hawker, C. J.; Read De Alaniz, J. Design and Synthesis of Donor-Acceptor Stenhouse Adducts: A Visible Light Photoswitch Derived from Furfural. *Journal of Organic Chemistry* **2014**, *79* (23), 11316–11329. https://doi.org/10.1021/jo502206g.

(25) Sanchez, D. M.; Raucci, U.; Martínez, T. J. In Silico Discovery of Multistep Chemistry Initiated by a Conical Intersection: The Challenging Case of Donor-Acceptor Stenhouse Adducts. *J Am Chem Soc* **2021**, *143* (48), 20015–20021. https://doi.org/10.1021/jacs.1c06648.

(26) di Donato, M.; Lerch, M. M.; Lapini, A.; Laurent, A. D.; Iagatti, A.; Bussotti, L.; Ihrig, S. P.; Medved, M.; Jacquemin, D.; Szymański, W.; Buma, W. J.; Foggi, P.; Feringa, B. L. Shedding Light on the Photoisomerization Pathway of Donor-Acceptor Stenhouse Adducts. *J Am Chem Soc* **2017**, *139* (44), 15596–15599. https://doi.org/10.1021/jacs.7b09081.

(27) Lerch, M. M.; Wezenberg, S. J.; Szymanski, W.; Feringa, B. L. Unraveling the Photoswitching Mechanism in Donor-Acceptor Stenhouse Adducts. *J Am Chem Soc* **2016**, *138* (20), 6344–6347. https://doi.org/10.1021/jacs.6b01722.

(28) Stricker, F.; Sanchez, D. M.; Raucci, U.; Dolinski, N. D.; Zayas, M. S.; Meisner, J.; Hawker, C. J.; Martínez, T. J.; Read de Alaniz, J. A Multi-Stage Single Photochrome System for Controlled Photoswitching Responses. *Nat Chem* **2022**, *14* (8), 942–948. https://doi.org/10.1038/s41557-022-00947-8.

(29) Sroda, M. M.; Stricker, F.; Peterson, J. A.; Bernal, A.; Read de Alaniz, J. Donor–Acceptor Stenhouse Adducts: Exploring the Effects of Ionic Character. *Chemistry - A European Journal* **2021**, *27* (12), 4183–4190. https://doi.org/10.1002/chem.202005110.

(30) Sroda, M. M.; Lee, J.; Kwon, Y.; Stricker, F.; Park, M.; Valentine, M. T.; Read de Alaniz, J. Role of Material Composition in Photothermal Actuation of DASA-Based

Polymers. *ACS Appl Polym Mater* **2022**, *4* (1), 141–149. https://doi.org/10.1021/acsapm.1c01108.

(31) Dong, X.; Tong, F.; Hanson, K. M.; Al-Kaysi, R. O.; Kitagawa, D.; Kobatake, S.; Bardeen, C. J. Hybrid Organic-Inorganic Photon-Powered Actuators Based on Aligned Diarylethene Nanocrystals. *Chemistry of Materials* **2019**, *31* (3), 1016–1022. https://doi.org/10.1021/acs.chemmater.8b04568.

(32) Tong, F.; Xu, W.; Al-Haidar, M.; Kitagawa, D.; Al-Kaysi, R. O.; Bardeen, C. J. Photomechanically Induced Magnetic Field Response by Controlling Molecular Orientation in 9-Methylanthracene Microcrystals. *Angewandte Chemie International Edition* **2018**, *57* (24), 7080–7084. https://doi.org/https://doi.org/10.1002/anie.201802423.

(33) Li, W.; Kitagawa, D.; Kobatake, S.; Bekyarova, E.; Bardeen, C. J. Patterning Submicron Photomechanical Features into Single Diarylethene Crystals Using Electron Beam Lithography. *Nanoscale Horiz* **2022**. https://doi.org/10.1039/D2NH00205A.

(34) Yao, Y.; Zhang, L.; Leydecker, T.; Samorì, P. Direct Photolithography on Molecular Crystals for High Performance Organic Optoelectronic Devices. *J Am Chem Soc* **2018**, *140* (22), 6984–6990. https://doi.org/https://doi.org/10.1021/jacs.8b03526.

(35) Kuenstler, A. S.; Kim, H.; Hayward, R. C. Liquid Crystal Elastomer Waveguide Actuators. *Advanced Materials* **2019**, *31* (24), 1901216. https://doi.org/10.1002/adma.201901216.

(36) Matějka, L.; Ilavský, M.; Dušek, K.; Wichterle, O. Photomechanical Effects in Crosslinked Photochromic Polymers. *Polymer (Guildf)* **1981**, *22* (11), 1511–1515. https://doi.org/10.1016/0032-3861(81)90321-9.

(37) Tong, F.; Kitagawa, D.; Bushnak, I.; Al-Kaysi, R. O.; Bardeen, C. J. Light-Powered Autonomous Flagella-Like Motion of Molecular Crystal Microwires. *Angewandte Chemie - International Edition* **2021**, *60* (5), 2414–2423. https://doi.org/10.1002/ANIE.202012417.

(38) Xu, T. Y.; Tong, F.; Xu, H.; Wang, M. Q.; Tian, H.; Qu, D. H. Engineering Photomechanical Molecular Crystals to Achieve Extraordinary Expansion Based on Solid-State [2 + 2] Photocycloaddition. *J Am Chem Soc* **2022**, *144* (14), 6278–6290. https://doi.org/10.1021/jacs.1c12485.

(39) Berges, A. J.; Li, W.; Xu, W.; Tong, F.; Al-Kaysi, R. O.; Hayward, R. C.; Bardeen, C. J. Photomechanical Structures Based on Porous Alumina Templates Filled with 9-Methylanthracene Nanowires. *Crystals (Basel)* **2022**, *12* (6), 808. https://doi.org/10.3390/cryst12060808.

(40) Jung, C.; Kim, G.; Jeong, M.; Jang, J.; Dong, Z.; Badloe, T.; Yang, J. K. W.; Rho, J. Metasurface-Driven Optically Variable Devices. *Chemical Reviews*. American Chemical Society November 10, 2021, pp 13013–13050. https://doi.org/10.1021/acs.chemrev.1c00294.

(41) Kim, D. Y.; Lee, S. A.; Kim, H.; Min Kim, S.; Kim, N.; Jeong, K. U. An Azobenzene-Based Photochromic Liquid Crystalline Amphiphile for a Remote-Controllable Light Shutter. *Chemical Communications* **2015**, *51* (55), 11080–11083. https://doi.org/10.1039/c5cc02834e.

(42) Hu, J.; Li, X.; Ni, Y.; Ma, S.; Yu, H. A Programmable and Biomimetic Photo-Actuator: A Composite of a Photo-Liquefiable Azobenzene Derivative and Commercial Plastic Film. *J Mater Chem C Mater* **2018**, *6* (40), 10815–10821. https://doi.org/10.1039/C8TC03693D.

(43) Zha, R. H.; Vantomme, G.; Berrocal, J. A.; Gosens, R.; de Waal, B.; Meskers, S.; Meijer, E. W. Photoswitchable Nanomaterials Based on Hierarchically Organized Siloxane Oligomers. *Adv Funct Mater* **2018**, *28* (1). https://doi.org/10.1002/adfm.201703952.

(44) Norikane, Y.; Uchida, E.; Tanaka, S.; Fujiwara, K.; Nagai, H.; Akiyama, H. Photoinduced Phase Transitions in Rod-Shaped Azobenzene with Different Alkyl Chain Length. *Journal of Photopolymer Science and Technology* **2016**, *29* (1), 149–157. https://doi.org/10.2494/PHOTOPOLYMER.29.149.

(45) Norikane, Y.; Uchida, E.; Tanaka, S.; Fujiwara, K.; Koyama, E.; Azumi, R.; Akiyama, H.; Kihara, H.; Yoshida, M. Photoinduced Crystal-to-Liquid Phase Transitions of Azobenzene Derivatives and Their Application in Photolithography Processes through a Solid-Liquid Patterning. *Org Lett* **2014**, *16* (19), 5012–5015. https://doi.org/10.1021/ol502223u.

(46) Han, G. G. D.; Li, H.; Grossman, J. C. Optically-Controlled Long-Term Storage and Release of Thermal Energy in Phase-Change Materials. *Nat Commun* **2017**, *8* (1). https://doi.org/10.1038/s41467-017-01608-y.

(47) Ma, H.; Xiao, X.; Zhang, X. Recent Advances for Phase-Transition Materials for Actuators. *J. Appl. Phys* **2020**, *128*, 101101. https://doi.org/10.1063/5.0020596.

(48) Wilhelm, E.; Richter, C.; Rapp, B. E. Phase Change Materials in Microactuators: Basics, Applications and Perspectives. *Sens Actuators A Phys* **2018**, *271*, 303–347. https://doi.org/10.1016/j.sna.2018.01.043.

(49) Templin, P. R. Coefficient of Volume Expansion for Petroleum Waxes and Pure N-Paraffins. *Ind Eng Chem* **1956**, *48* (1), 154–161. https://doi.org/10.1021/ie50553a043.

(50) Earnshaw, J. C.; Hughes, C. J. A Novel Surface Induced Phase Transition in Normal Alkane Fluids. *Trends in Colloid and Interface Science VII* **1993**, 108–111. https://doi.org/10.1007/BFB0118485.

(51) Ogden, S.; Klintberg, L.; Thornell, G.; Hjort, K.; Bodén, R. Review on Miniaturized Paraffin Phase Change Actuators, Valves, and Pumps. *Microfluid Nanofluidics* **2014**, *17* (1), 53–71. https://doi.org/10.1007/s10404-013-1289-3.

(52) Park, J. M.; Cho, Y. K.; Lee, B. S.; Lee, J. G.; Ko, C. Multifunctional Microvalves Control by Optical Illumination on Nanoheaters and Its Application in Centrifugal Microfluidic Devices. *Lab Chip* **2007**, *7* (5), 557–564. https://doi.org/10.1039/b616112j.

(53) Lui, B. F.; Bardeen, C. J. Using Small Molecule Absorbers to Create a Photothermal Wax Motor. *Small* **2021**, *2105356*, 1–7. https://doi.org/10.1002/smll.202105356.

(54) Carlen, E. T.; Mastrangelo, C. H. Electrothermally Activated Paraffin Microactuators. *Journal of Microelectromechanical Systems* **2002**, *11* (3), 165–174. https://doi.org/10.1109/JMEMS.2002.1007394.

(55) Hou, S.; Wang, M.; Guo, S.; Su, M. Photothermally Driven Refreshable Microactuators Based on Graphene Oxide Doped Paraffin. *ACS Appl Mater Interfaces* **2017**, *9* (31), 26476–26482. https://doi.org/10.1021/acsami.7b08728.

(56) di Giambattista, C.; Sanctuary, R.; Perigo, E.; Baller, J. Relaxations in the Metastable Rotator Phase of N-Eicosane. *Journal of Chemical Physics* **2015**, *143* (5). https://doi.org/10.1063/1.4928059.

(57) Saydam, V.; Duan, X. Dispersing Different Nanoparticles in Paraffin Wax as Enhanced Phase Change Materials: A Study on the Stability Issue. *J Therm Anal Calorim* **2019**, *135* (2), 1135–1144. https://doi.org/10.1007/s10973-018-7484-4.

(58) Hou, S.; Wang, M.; Guo, S.; Su, M. Photothermally Driven Refreshable Microactuators Based on Graphene Oxide Doped Paraffin. *ACS Appl Mater Interfaces* **2017**, *9* (31), 26476–26482. https://doi.org/10.1021/acsami.7b08728.

(59) E. Zimerman, O.; G. Weiss, R. Pyrene Photochemistry in Solid N-Alkane Matrices: Comparisons with Liquid-Phase Reactions. *J Phys Chem A* **1999**, *103* (48), 9794–9804. https://doi.org/10.1021/jp992339h.

(60) Tro, N. *Chemistry: A Molecular Approach*, 2nd ed.; Folchetti, N., Ed.; Pearson Prentice Hall: Upper Saddle River, 2011; Vol. 1.

(61) Bearpark, M. J.; Bernardi, F.; Clifford, S.; Olivucci, M.; Robb, M. A.; Smith, B. R.; Vreven, T. The Azulene S 1 State Decays via a Conical Intersection: A CASSCF

Study with MMVB Dynamics. *J Am Chem Soc* **1996**. https://doi.org/10.1021/ja9514555.

(62) Scott Tibbitts. High Output Paraffin Actuators: Utilization in Aerospace Mechanisms. In *NASA. Langley Research Center, The 22nd Aerospace Mechanisms Symposium*; Boulder, 1988.

(63) Srinivasan, P.; Spearing, S. M. Material Selection for Optimal Design of Thermally Actuated Pneumatic and Phase Change Microactuators. *Journal of Microelectromechanical Systems* **2009**, *18* (2), 239–249. https://doi.org/10.1109/JMEMS.2009.2013385.

(64) Krulevitch, P.; Lee, A. P.; Ramsey, P. B.; Trevino, J. C.; Hamilton, J.; Northrup, M. A. Thin Film Shape Memory Alloy Microactuators. *Journal of Microelectromechanical Systems* **1996**, *5* (4), 270–282. https://doi.org/10.1109/84.546407.

(65) Liang, J.; Xu, Y.; Huang, Y.; Zhang, L.; Wang, Y.; Ma, Y.; Li, F.; Guo, T.; Chen, Y. Infrared-Triggered Actuators from Graphene-Based Nanocomposites. *Journal of Physical Chemistry C* **2009**, *113* (22), 9921–9927. https://doi.org/10.1021/jp901284d.

(66) Chen, L.-J.; Li, Q. Soft Photoactuators in Microfluidics. In *Photoactive Functional Soft Materials*; 2019; pp 167–196. https://doi.org/10.1002/9783527816774.ch5.

(67) Hu, J.; Ma, S.; Yu, H.; Li, Q. Photomechanical Soft Nanocomposites: Synergies Between Soft Matrix and Energy Conversion Additives. In *Photoactive Functional Soft Materials*; 2019; pp 285–317. https://doi.org/10.1002/9783527816774.ch8.

2. Experimental details

2.1 Foreword

This section is prefaced by stating that the preparation of materials and specific instrumentation used for each experiment are contained in their own individual chapters. Instead, this chapter will detail the method development of the techniques and instruments used for the experiments described throughout this thesis.

2.2 UV-Vis absorption spectroscopy

The primary tool of analysis of photochromes used in our lab is UV-Vis absorption spectroscopy. The Agilent Cary 60, 500, and 5000 are the spectrometers available at UC Riverside's Analytical Chemistry Instrumentation Facility and their operation manuals can be found online. However, in situations where a specialized cuvette or flow cell is necessary, a temperature sensitive phase change material is being studied, or if simultaneous irradiation with a diode laser is required, then a custom UV-Vis spectrometer must be built for ease of access to the sample chamber. **Figure 2.1** illustrates an example of a custom UV-Vis spectrometer built in our lab. This spectrometer is functionally the same as the Agilent Cary variants.

The light source is a combination of a tungsten light bulb (380-800 nm) and a deuterium lamp (180-370 nm) coupled through a fiber optic, although in principle any light source would work in this setup (as long as the wavelengths of interest are present). The detector that is used in our lab is an Ocean Optics USB4000, which is made by OceanInsight and the operating manual can be found online. The device is paired with a

software called OceanView, which is used to operate the instrument. The download and operating manual could also be found online.

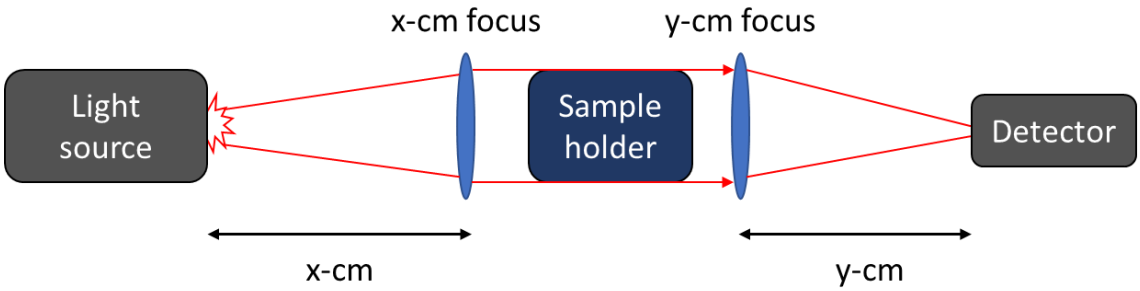

Figure 2.1 Schematic of a custom spectrometer. A light source passes through some x-cm focus placed the same distance away (x-cm). This collimates the light, and another focus (y-cm) is placed on the opposite side, followed by a detector. For example, if the first focus is x = 10-cm, then the distance between the light source and the focus is 10-cm. The detector is placed y-cm away from the second focus and collects the signal for the experiment. As an example, if the second focus is y = 5-cm, then the distance between the second focus and the detector is 5-cm. In between the foci, a sample holder is placed so that the material of interest could be probed. It is worth noting that the distance between the two foci do not matter since the light is collimated.

2.3 Fabrication of ultrathin cuvettes: 0.5-micron cell

The optical density of photochromes is an important metric in spectroscopy as it is an indicator of how much light is being absorbed by the sample and how much light is being transmitted through the sample. Beer's law can be used to calculate the absorption of a sample with the following equation:[1]

$$A = L \times c \times \varepsilon$$

where A (unitless) is the absorption of the sample, L (cm) is the path length of the cuvette (or thickness of the solid film if a solid is being measured), C (M, mol dm^{-3}) is the concentration of the sample, and ε (M^{-1} cm^{-1}) is the molar extinction coefficient of the

molecule. Absorbance can also be used to calculate transmittance, or the fraction of incident light which passes through the sample (i.e., not absorbed) with the following equation:[1]

$$A = 2 - \log(\%T)$$

Where *A* (unitless) is the absorption and *%T* (unitless) is the percent transmittance. Transmittance *T* is defined as I/I_0 where *I* = light detected by the detector (i.e., output) and I_0 is the initial or incident light (input).

In an experiment where it is necessary to vary the concentration of a photochrome, the optical density (absorption) must be held constant in order for each sample to experience the same number of photons. To achieve this, the path length of the cuvette is the one parameter that could be varied. The following is the experimental details on how to fabricate an ultrathin cuvette using photolithography.

The following is prepared in the Nanofabrication facility at UC Riverside. **Figure 2.2** details the photolithographic process. A microscope glass slide was cleaned with acetone, methanol, isopropanol, and dried with N_2 gas. The microscope slide was then placed on a spin coater and S1813 positive photoresist was deposited. The slide was spun for 30 seconds at 3000 RPM and baked for 10 minutes at 100 °C. Since S1813 is a positive resist and the photomask is a negative mask, an image reversal technique was used.[2] First, the photomask was placed on top of the substrate with the Suss MA-6 Mask Aligner and exposed to UV light for 10 seconds. The slide was removed and baked on a hot plate for 10 minutes at 110 °C. The slide was then exposed to UV light again without a mask for 10 seconds and then placed in the developing solution (SU-8) for 60 seconds. 0.5-micron of

gold was then deposited by electron beam evaporation and acetone was used in the reverse liftoff process to remove the unwanted areas. The result of this procedure is the production of a 0.5-micron cuvette and the schematic is shown in **Figure 2.3**. The same procedure could be followed to make a cuvette that is thicker or thinner than 0.5 μm.

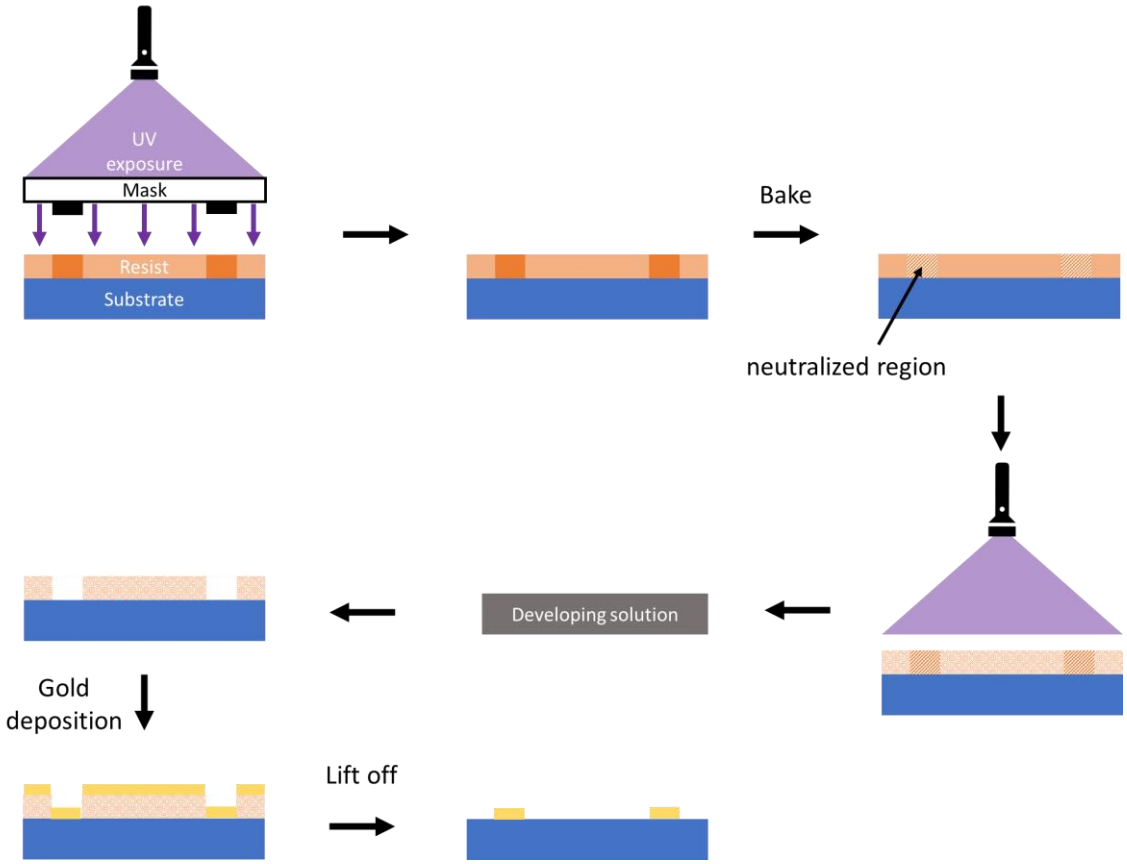

Figure 2.2 Schematic of the inverse image photolithography process. A negative mask was used to design the pattern of the cuvette.

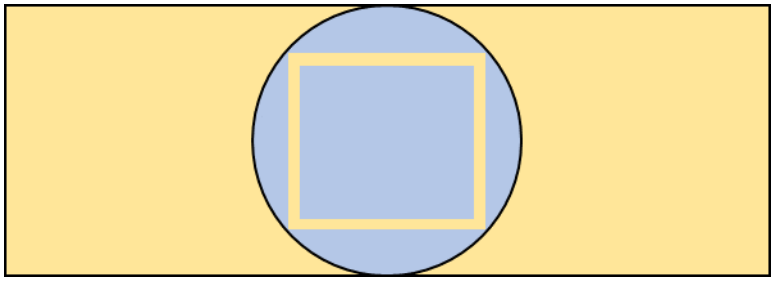

Figure 2.3 Diagram of a custom-made cuvette used for steady state absorption. The gold regions represent a layer of gold that was deposited via electron beam evaporation. The gold is 0.5 μm thick. The blue regions are the exposed regions of glass. The inside square is the reservoir for the liquid and the quarter-moons on the outside edges of the square serve as overflow regions. A second glass slide of the same size is placed on top, and the aperture is held together with binder clips.

2.4 Differential scanning calorimetry

Differential scanning calorimetry (DSC) is a technique used to probe the thermal properties of molecules and polymers, like the melting point and glass transition temperature.[3] The instrument available at UC Riverside is the Netzsch DSC 214 Polyma and its operating manual can be found online. The theory behind how DSC operates is beyond the scope of this thesis, but the sample preparation will be described. Aluminum sample pans that are specifically calibrated for the Netzsch DSC are used as the sample vessels. Sample preparation is to simply place some amount of the material in the sample pan and to place the sample and the reference pans in the respective slots in the instrument. The data collected is then analyzed on Netzsch's proprietary software and the download can be found online.

2.5 Nuclear magnetic resonance spectroscopy

Nuclear magnetic resonance (NMR) spectroscopy is a powerful technique used in our lab to distinguish between isomers that are formed during a photochemical reaction.[4]

More specifically, proton, or ^{1}H-NMR is used. The reactions could be carried out in either the deuterated solvent or as a solid and dissolved afterwards in the deuterated solvent to track the molecular changes. **Figure 2.4** shows an example of ^{1}H-NMR being used as a tool to distinguish between trans and cis isomers of an azobenzene derivative studied in our lab.

UC Riverside has access to Bruker Avance 400, 500, 600 and 700 NMRs and their operation manuals could be found online. Both Bruker's proprietary software and MestreNova could be used to analyze the spectra that the Bruker Avance generates. It is worth mentioning that liquid NMR is considered a destructive technique because sample recovery is difficult. In the event that analysis of a photomechanical application is necessary (and dissolving the material in deuterated solvent is impractical), solid-state NMR (ssNMR) could be used, but this technique will not be discussed in this thesis.

2.6 Preparation of wax-small molecule composites

Waxes are easiest to work with in the liquid state as they can be manipulated and mixed with other reagents. Everything that will be used to handle the wax should be equal to or hotter than the melting point of the wax. Therefore, the wax, glass pipets, and intended vessel for the wax should be placed into an oven to get up to temperature. Afterwards, the wax should be handled like any other organic solvent, i.e., it can be used to dissolve other nonpolar organic reagents. In our lab, the main wax used in the experiments described in this thesis is eicosane ($C_{20}H_{42}$), which has a melting point of 36-38 °C. It is convenient to measure the waxes out by weight and to use the density to convert the weight to volume. The density of solid eicosane is 0.7889 g cm^{-3}.[5] The concentration of the mixture could

then be calculated by moles of small molecule divided by the volume of eicosane used, giving the traditional unit of Molarity (mol dm^{-3}). More detailed descriptions of fabrication of these wax-small molecule mixtures are described in detail in the Chapters 4 and 5.

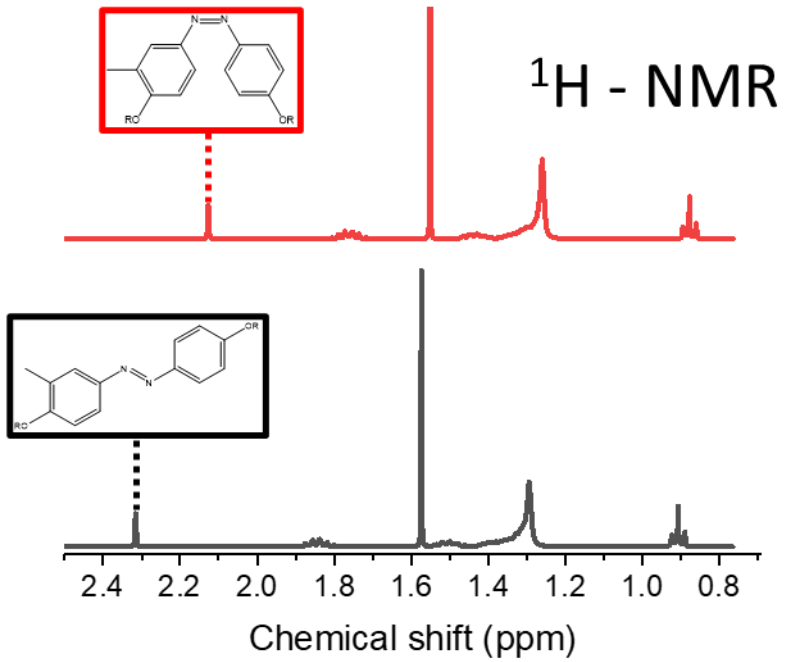

Figure 2.4 Proton NMR of an azobenzene derivative. The black spectrum corresponds to the *trans* (unreacted) form of the azobenzene derivative and could be distinguished by the position of the singlet peak at 2.3 ppm. This singlet corresponds to the protons on the methyl group on the phenyl ring. After prolong exposure to 365 nm light, the photoisomerization occurs and the *cis* isomer is formed as evidenced of the disappearance of the peak at 2.3 ppm and an appearance of a peak at 2.1 ppm (protons of the methyl group on the *cis* isomer).

2.7 Doped polymer thin films: the drop cast method

Doped polymer thin films are frequently used in our lab because it allows us to probe the optical properties of the molecule in the solid state. Molecules are codissolved with a polymer (e.g., polymethyl methacrylate, polystyrene, polyvinyl alcohol, etc.) in a compatible solvent. Afterwards, the solution is drop casted onto a glass microscope slide

and the solvent is evaporated at room temperature. The resulting films are optically clear and can be used for a variety of purposes, whether for spectroscopy or for photomechanical applications. The evaporation rate of the solvent will also dictate the opacity of the film. Typically, the slower the evaporation, the clearer the film.

If molecular polymer films are not wanted and nanoparticles are desired, the nanoprecipitation method can be used to make nanoaggregates.[6] Briefly, the molecules are dissolved in acetone or THF and injected into a beaker or petri dish containing deionized water while vigorously stirring with a magnetic stir bar. A vessel with a wider mouth is desired here because the evaporation of the organic solvent is crucial, so it is not advised to use a bottle, vial, or Erlenmeyer flask. The nanoparticle suspension can then be used to codissolve a polymer, however the solvent used in this method is water, so the polymer must also be soluble in water. It should be noted that the polymer can be omitted and the molecules themselves can be drop casted to make molecular thin films as well. To have definitive control of the film's thicknesses, a spin coater can be used but will not be discussed here.

2.8 Wax motor assembly

2.8.1 Generation 1 wax motors

Two separate wax motors were created to house the composites from **section 2.6**. The first version (referred to as generation 1) is an adapted commercialized wax motor made by Honda. A Honda 16620-Z0Y-M41 Thermostat (wax motor) was purchased online and modified at the UC Riverside machine shop. Briefly, the bottom of the Honda wax

motor was lathed off and the wax was emptied out of the cavity. The wax motor was then press fitted into an aluminum puck and a detachable window (Esco optics, 12.80-mm diameter borosilicate window) was placed on the bottom for optical access. A Viton O-ring was placed in between the actuator body and the window to prevent the window from breaking while assembling the actuator. **Figure 2.5** illustrates the design and dimensions of the generation 1 motor as well as the still images of the real actuator.

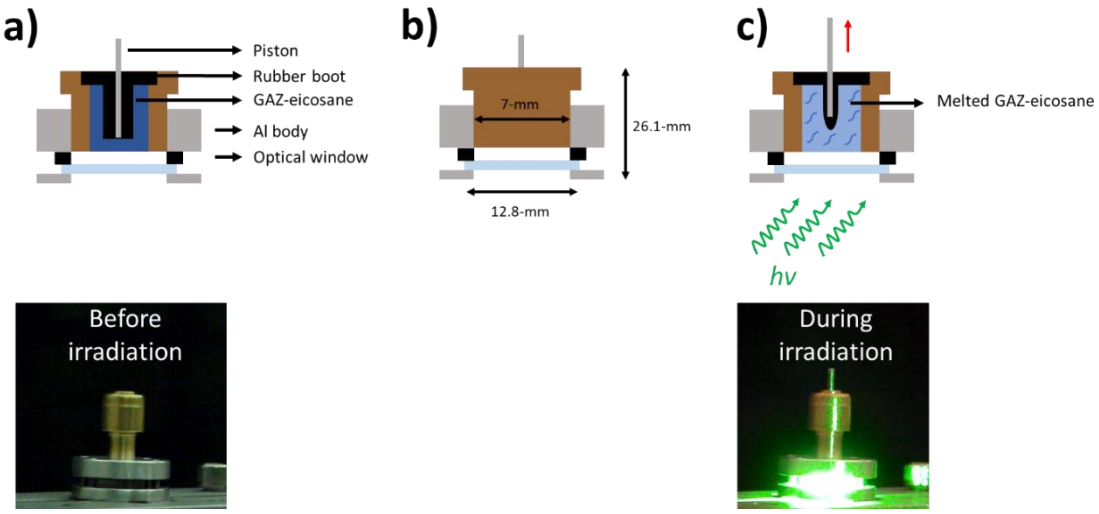

Figure 2.5 Design of the generation 1 wax motor. **a)** Illustrates a cross section of how the actuator looks like. **b)** Shows the dimensions of the height and width of the actuator. **c)** When the wax melts, it compresses a black rubber boot which squeezes a metal piston upwards.

2.8.2 Generation 2 wax motors

Generation 2 wax motors were built because the black rubber boot built into the Honda wax motor absorbed the visible light used to melt the wax. Over time, there was noticeable degradation of the rubber boot, which led to diminishing performances of the actuator. This prompted the creation of a new wax motor that was much simpler in design and did not rely on a rubber boot to drive the extension and contraction of the metal piston.

The design philosophy is identical to generation 1 in that the wax resides in a reservoir and expands against some inert membrane to drive the actuation. The difference is that the silicone membrane (purchased from The Rubber Company, 0.5-mm thickness) used here is robust; it does not absorb the wavelengths used to melt the waxes and can withstand the temperature cycles that the actuator undergoes. **Figure 2.6** illustrates the design of the generation 2 actuator. All of the pieces shown are custom made at the machine shop at UC Riverside except the window, O-rings, and silicone membrane.

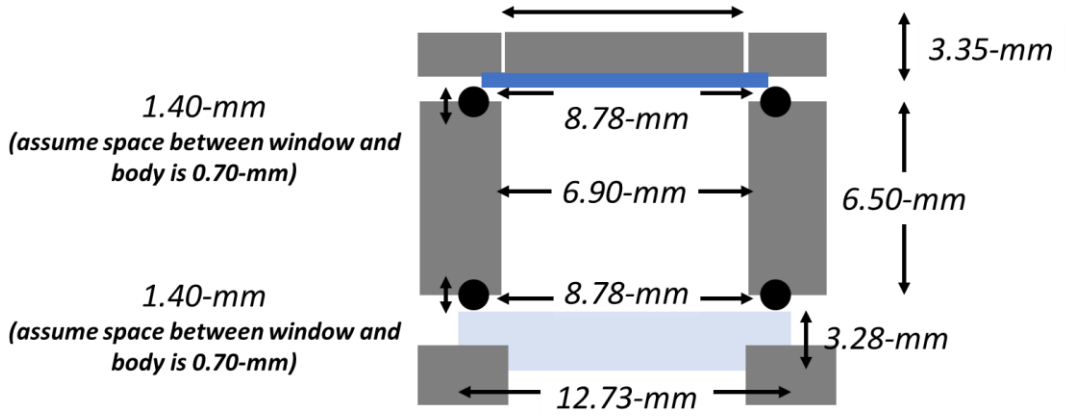

Figure 2.6 Generation 2 actuator's design and dimensions. The only moveable part of this actuator is the 0.5-mm thick silicone membrane (blue sheet) which is flexible enough to expand against the expanding wax without tearing.

The noted differences between generations 1 and 2 are that the rubber boot is now replaced with a silicone membrane and that a second Viton O-ring exists in the top half of the actuator as well, acting as a seal between the actuator body and the membrane so that the wax does not leak when the actuator is “on”. **Figure 2.7** show the still images of how generation 2 looks like.

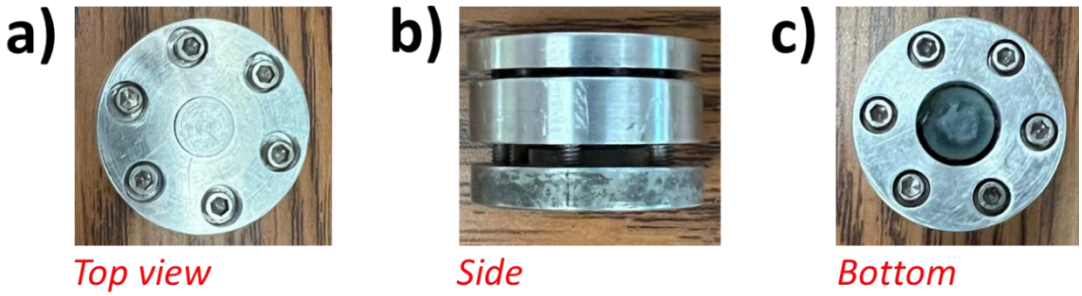

Figure 2.7 Still images of the generation 2 actuator. **a)** Is the top view where the piston can be seen. **b)** The side view of the actuator. **c)** Bottom view with the window showing the wax composite that is inside of the actuator.

2.8.3 Filling the actuators with wax

As stated previously, waxes are considerably easier to handle when they are in the liquid phase. Generation 1 is assembled without attaching the window while generation 2 is assembled without attaching the top aluminum piece. From here, the motors can be filled up with the molten wax. It should be noted that waxes contract when they cool down, so it is recommended to overfill the motors so when the wax contracts, it is as full to the lip of the container as possible. Any remaining pockets should be patched with some more molten wax. Should there be any excess wax if the actuators are overfilled, the excess can be scraped off with either a razor blade or a piece of plastic.

2.9 Measuring the extension, rate, and work output of the custom wax motors

The wax motors have a convenient range of motion: up and down. This allows us to place weights on top of the actuator and use Force = mass × acceleration (of gravity) to calculate the amount of force generated by the actuator. Work = Force × extension (of piston) can be used to calculate the work generated by the actuator However, the extension of the piston cannot be directly measured during the actuation phase without disturbing the

weights or the actuator itself. Instead, the entire extension and contraction process is filmed with a camera, and image analysis is used to determine the rate of extension along with the amount extended. The temperature of the actuator is measured by utilizing a thermocouple probe taped to the side to the actuator with electrical tape. The data collected could be plotted with respect to time to monitor the dynamics of the actuator. A sample of this plot is shown in **Figure 2.8**.

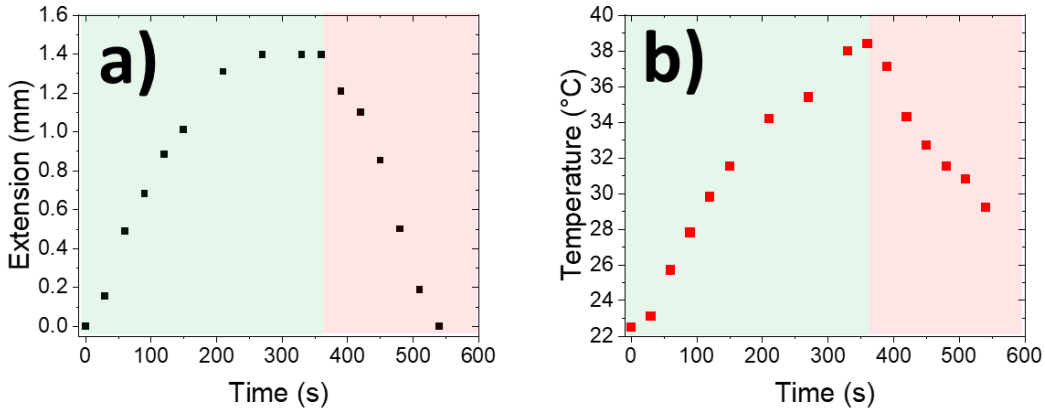

Figure 2.8 A plot of a generation 2 actuator's **a)** extension and **b)** temperature dynamics. The area highlighted in green represents when the laser is turned on while the area in red is when the laser is turned off.

The work output of the actuator can be calculated from a plot of extension versus force exerted onto the actuator. The resulting plot should yield a straight line, and the integral of this line gives the work output of the actuator. More specifically, the following equation is used:

$$Work = \int_0^{Maximum\ extension} mx + b\ dx$$

Where m = slope of the line and b = y-intercept of the line. The stop force (amount of force where the actuator *cannot* move) is the y-intercept of the line. The weight of the stop force could be calculated by dividing the y-intercept by the acceleration of gravity. A sample of this plot is shown in **Figure 2.9**.

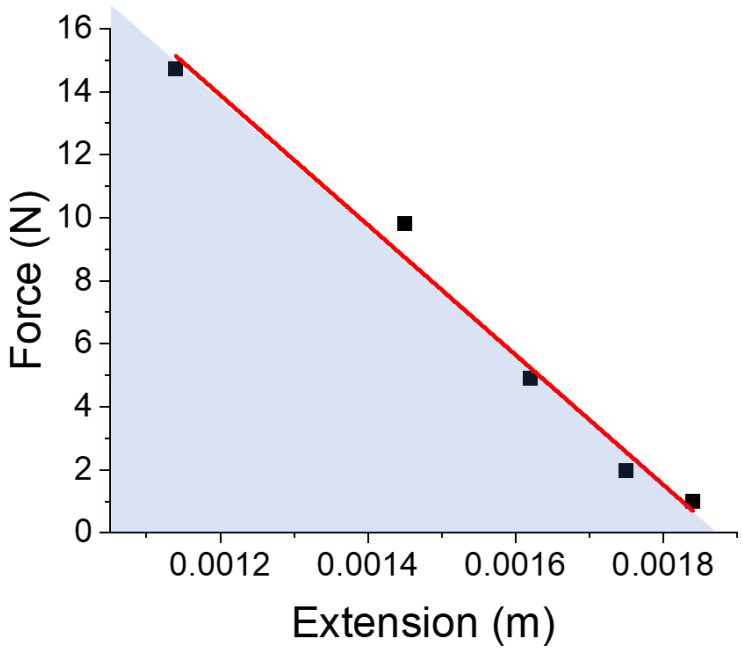

Figure 2.9 A plot of a generation 2 actuator's work output. The area highlighted in blue is the area under the curve, which can be calculated by taking the integral of the equation of the line.

The work density has units of J cm^{-3} (equivalent to MJ m^{-3}) can be calculated by obtaining the work output from a curve like **Figure 2.9** and dividing by the volume of wax inside the actuator. Refer to **section 2.6** on calculating the volume of wax in an actuator.

2.10 References

(1) McQuarrie, D. A.; Simon, J. D. Physical Chemistry A Molecular Approach; McGuire, A., Ed.; University Science Books, 1997; p 625.

(2) Ailing, E.; Stauffer, C. Image Reversal Of Positive Photoresist A New Tool For Advancing Integrated Circuit Fabrication. In *Proc.SPIE*; 1985; Vol. 0539, pp 194–218. https://doi.org/10.1117/12.947835.

(3) Menczel, J. D.; Judovits, L.; Prime, R. B.; Bair, H. E.; Reading, M.; Swier, S. Differential Scanning Calorimetry (DSC). In *Thermal Analysis of Polymers*; 2009; pp 7–239. https://doi.org/10.1002/9780470423837.ch2.

(4) Beauchamp, P. Advanced Organic Spectroscopy Tools For Beginning Organic Spectroscopists; CreateSpace Independent Publishing Platform, 2016; p 147.

(5) F. Seyer, Wm.; F. Patterson, R.; L. Keays, J. The Density and Transition Points of the N-Paraffin Hydrocarbons. *J Am Chem Soc* **2002**, *66* (2), 179–182. https://doi.org/10.1021/ja01230a004.

(6) Sadguru Prasad, L. T.; Madhusudhan, B.; Kodihalli, P. B.; Ghosh, P. C. Development and in Vitro Evaluation of Oxytetracycline-Loaded PMMA Nanoparticles for Oral Delivery against Anaplasmosis. *IET Nanobiotechnol* **2017**, *11* (1), 119–126. https://doi.org/10.1049/iet-nbt.2016.0061.

3. Unusual Concentration Dependence of the Photoisomerization Reaction in Donor-Acceptor Stenhouse Adducts

3.1 Preface

We begin with the discussion of a novel photoswitch, Donor-acceptor Stenhouse adducts (DASAs). In this chapter, the chemistry of DASA is studied with the intent of using the molecule as a solid→solid photomechanical material. The photoisomerization kinetics of a third generation DASA are examined over a range of concentrations. DASA switches efficiently at micromolar concentrations in both liquid solution and in polymers, but as the photochrome concentration is increased there is a dramatic inhibition of the photoisomerization. A kinetic study of both the reactant and photoproduct decays at varying concentrations and in different hosts indicates that the forward photoisomerization and the thermal backward reaction can change by factors of 20 or more depending on DASA concentration. Femtosecond transient absorption experiments show that the initial *cis*→*trans* step of the isomerization is not affected by concentration. It is hypothesized that long-range Coulombic interactions interfere with the ground state electrocyclization stage of the isomerization, which is unique to the DASA family of photochromes. The physical origin of the inhibition of photoswitching at high photochrome concentrations must be understood if the DASA class of molecules is to be used for applications that require high photochrome concentrations, including photomechanical actuation.

3.2 Introduction

The ability of molecules to isomerize after light exposure (photochromism) has enabled applications ranging from data storage to fluorescence microscopy to optical computing. There exist many classes of organic molecules that undergo photoisomerization reactions in dilute liquid solutions, providing a wide array of options for the design of light-responsive materials.[1, 2] Many of these photochromic molecules retain their ability to photoisomerize in solid hosts like polymers. But when photochrome concentrations are increased to the point where intermolecular interactions become non-negligible, the photochemistry can be modulated by the close proximity of the photochromes. Electronic interactions between neighboring molecules can lead to the formation of delocalized excited states (excitons) with different reactivities. Steric interactions can inhibit the nuclear motions necessary to complete the isomerization reaction. In rare cases, molecular interactions can also facilitate the photochemistry, for example through a chain reaction mechanism.[3-5]

The effects of high photochrome density on reaction kinetics must be taken into account for some applications. For example, the development of organic photomechanical materials requires high photochrome concentrations because the work density should be directly proportional to the photochrome density.[6, 7] While multiple photochromic molecule classes have exhibited photomechanical behavior in polymer hosts[8-11] and neat crystals[12-22], there is still a need for new and improved photomechanical elements, especially ones that can be activated by visible instead of ultraviolet light.[23] A recently developed class of photochromic molecules based on donor-acceptor Stenhouse adducts

(DASAs) absorb in the visible and near-infrared spectral regions.[24-30] Even more promising, these molecules are negative photochromes, meaning that the photoproduct absorption shifts to the blue of the reactant absorption and thus does not absorb the exciting light.[31] This property can lead to high conversion efficiencies due to the avoidance of a photostationary state. The light-driven forward reaction pathway for the CF_3 pyrazolone based DASA derivative (E)-4-((2Z,4E)-2-hydroxy-5-(2-methylindolin-1-yl)penta-2,4-dien-1-ylidene)-2-phenyl-5-(trifluoromethyl)-2,4-dihydro-3H-pyrazol-3-one (referred to as **DASA** in this chapter) is shown in **Scheme 3.1**.[32, 33] The reverse reaction is thermally activated and occurs on timescales of seconds to minutes in liquid solution. We became interested in the DASAs as possible active elements for photomechanical materials. Their favorable absorption properties and negative photochromism make them ideal for this application, but highly concentrated samples, or even single crystals, are required in order to generate useful amounts of work.

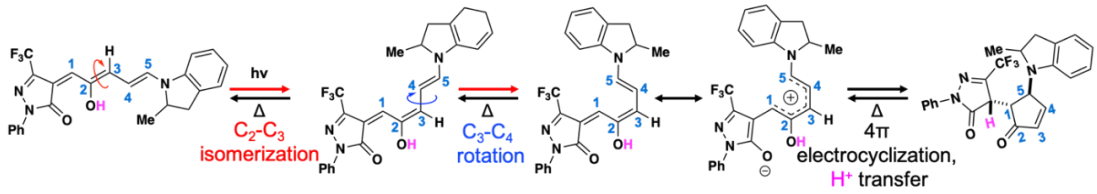

Scheme 3.1 The photoisomerization of DASA occurs in two steps: 1) an actinic step where a Z→E isomerization along the C_2-C_3 bond occurs, followed by 2) the ground state C_3-C_4 rotation and 4π electrocyclization.

In this chapter, we examine the photochemical properties of **DASA** over a range of concentrations. We focus on the third generation **DASA** molecule shown in **Scheme 3.1** because this derivative has a relatively long-wavelength absorption and good open-form isomer stability.[34] We find that **DASA** switches efficiently at low concentrations in both

liquid solution and in polymer hosts. As the photochrome concentration is increased, however, the ability of **DASA** to photoswitch decreases drastically. At concentrations on the order of 10^{-3} M, the photoswitching is effectively turned off for moderate light intensities on the order of 1 mW/cm^2. A similar trend is observed in polymer hosts. A two-state kinetic analysis, combined with photophysical measurements, is used to evaluate how changes in forward and reverse reaction rates conspire to inhibit the net production of the ring-closed isomer. Our results indicate that the slowdown likely occurs during the proton transfer/ring-closing step, as opposed to the actinic *cis-trans* photoisomerization step. The electrocyclization reaction is unique to the **DASA** family of photochromes and may be vulnerable to environmental effects induced by polar molecules, including neighboring DASAs. The physical origin of the inhibition of photoswitching at high photochrome concentrations must be understood if the **DASA** class of molecules is to be used in photomechanical applications. Such an understanding would provide the basis for designing new **DASA** molecules that can switch efficiently at high concentrations.

3.3 Experimental

3.3.1 Sample preparation:

The synthesis of **DASA** has been reported previously.[34] Chloroform and toluene were purchased from Fischer Chemical. A series of different concentrations ranging from 10^{-6}-10^{-2} M (chloroform) and 10^{-6}-10^{-3} M (toluene) were prepared (10^{-2} M was unachievable in toluene due to limited solubility). To make the polymer samples, methylene chloride (Fisher Chemical) was used to prepare a 2.50×10^{-5} M stock solution of

DASA. Aliquots were taken from this stock to dissolve appropriate amounts of polystyrene and polymethyl(methacrylate), both purchased from Sigma-Aldrich, to create a series of concentrations ranging from 10^{-4}-10^{-1} M $\left(\frac{mol_{DASA}}{L_{polymer}}\right)$. The films were made by drop casting the **DASA**-polymer solutions on microscope slides purchased from Fisher Scientific. These films were placed in an oven at 80°C to ensure evaporation of residual solvent.

The spiropyran derivative (TCI Chemicals), 1,3,3-trimethylindolino-6'-nitrobenzopyrylospiran, was used as a control in this study. 91 mmol of the spiropyran derivative was used to create a 9.1 mM stock solution with chloroform as the solvent. From here, 1.4×10^{-6}-1.4×10^{-4} M concentrations were prepared by method of serial dilution.

3.3.2 Absorption & transient absorption studies:

An Ocean Optics USB4000 was employed to acquire the time-dependent absorption spectra of the samples under irradiation. The OceanView software was used to operate the spectrometer with a wavelength window of 400-800 nm and a full spectrum with acceptable signal-to-noise could be acquired within 1 s. The neat film and polymer samples were mounted in front of the probe light source and a 638 nm diode laser was used to isomerize the films. For liquid samples, we wanted to ensure that the optical densities were ~0.3 or less for reasons discussed in **section 3.4**. To achieve this, a demountable flow cell with variable path lengths was employed. For 3×10^{-6} M, a 1-cm cuvette was used. For higher concentrations in the range of 10^{-3}-10^{-6} M, a commercial demountable cell with a variable path length O-rings was utilized to ensure that the optical densities remained at ~0.30. **Table 3.1** illustrates which path lengths were used with their respective concentrations:

Table 3.1 Path lengths used in UV-Vis experiments with their respective concentrations to maintain an optical density of <0.3 are shown.

Concentration (M)	Path length (mm)
1×10^{-2}	0.0005
1×10^{-3}	0.015
1×10^{-4}	0.2
3×10^{-5}	0.5
8×10^{-6}	2.5
3×10^{-6}	10

The 638 nm laser beam was passed through a diffuser to uniformly illuminate the liquid samples with an intensity of 1.0 mW/cm^2, while a higher intensity of 11.4 mW/cm^2 was used for the polymer samples due to their slower reaction.

Transient absorption measurements were performed using a 1 kHz Coherent Libra femtosecond Ti:Sapphire laser system. The 642 nm pump beam was generated by sending the 800 nm fundamental output into a Palitra optical parametric amplifier. The probe beam was generated by focusing a portion of the fundamental into a 3 mm sapphire plate. Both beams were focused onto either a 0.015 and 0.5 mm path-length quartz flow cell that contained the 1 mM and 30 μM DASA/chloroform solutions, respectively. The probe beam after the sample was coupled into an Ultrafast Systems UV-VIS CMOS spectrometer. A solvent response was recorded under the same conditions for all samples in order to remove nonresonant contributions to the transient absorption signal. The transient absorption signals were analyzed using Ultrafast Systems Surface Xplorer software.

3.3.3 Differential scanning calorimetry:

Glass transition temperatures of the films were collected using a Netzsch 214 Polyma differential scanning calorimeter using a temperature range of 50°C – 150°C with

a 20°C heating rate, 1-minute holding, and a 20°C cooling rate. The films were heated and cooled for two cycles and the T_g of the second trial was recorded.

3.3.4 Powder X-ray diffraction (PXRD):

A few drops of DASA/toluene solution were deposited onto a clean glass slide (2.5 cm × 2.5 cm) to form a neat film. The glass slide was then put inside an oven at about 90 ^{o}C to evaporate the toluene. The PXRD data were collected on a Bruker D8 Advance X-ray powder diffractometer (CuK radiation, λ = 1. 5418 Å, 45 kV/40 mA power) at room temperature. The sample was measured in Bragg-Brentano geometry. The sample holder stage was fixed horizontally, and the detector (divergence slit = 0.76 mm without monochromator) rotates over the sample with a step size = 0.0263 degrees.

3.4 Results and Discussion

DASA is a polar molecule that is soluble in common organic solvents up to concentrations of ~10 mM. Over the concentration range 10^{-6}-10^{-2} M in both chloroform ($CHCl_3$) and toluene, the absorption spectrum remained remarkably constant, as shown in **Figure 3.1**. Even at the highest concentrations in these liquids, there is no sign of peak broadening or shifting that would indicate aggregation or electronic coupling. Note that the very high absorption coefficient of **DASA** (~10^5 $M^{-1}cm^{-1}$ at the absorption peak) necessitated the use of variable pathlength demountable cells. At the highest concentrations, the path length had to be reduced to 0.5 micron in order to accurately measure the spectrum and also minimize the variation in light intensity across the cell. This allowed us to assume a constant light intensity within the cell and simplified the kinetic analysis of the photoisomerization rates described below. In all cases the initial sample

absorbance at 638 nm was kept at 0.3 or less to ensure that molecules throughout the sample saw a maximum change in light intensity of 50% from front to back of the cell.

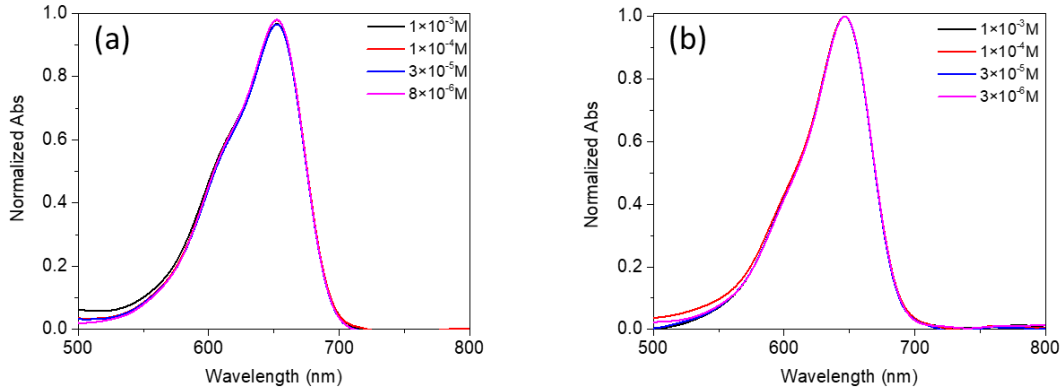

Figure 3.1 Absorption spectra of DASA at various concentrations. The spectra shape remains unchanged in both **(a)** toluene and **(b)** chloroform as the concentration is varied.

When the **DASA** solutions were exposed to 638 nm light, with an intensity of 1.0 mW/cm^2, the absorption steadily decreased until the forward photochemical reaction rate was balanced by the thermal reverse rate and a photostationary state (PSS) was achieved. An example of this data for $CHCl_3$ is shown in **Figure 3.2a**. In **Figure 3.2b**, we plot the time-dependent decrease in the **DASA** absorbance for concentrations ranging from 10^{-6} M to 10^{-2} M, all under identical irradiation conditions. Both the initial rate of absorbance decay and the asymptotic PSS value change with increasing concentration. A similar concentration dependence was observed in toluene (**Figure 3.3**).

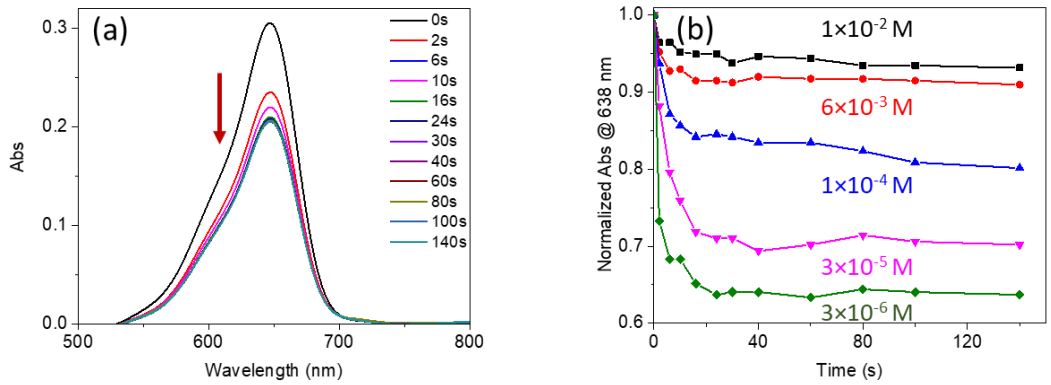

Figure 3.2 a) DASA absorption spectra at various times for an irradiated 3×10^{-6} M chloroform sample. A 638 nm laser (0.89 mW/cm^2) irradiated the sample until a photostationary state was obtained. **b)** The decay of absorption monitored at 638 nm versus time for different **DASA** concentrations in chloroform.

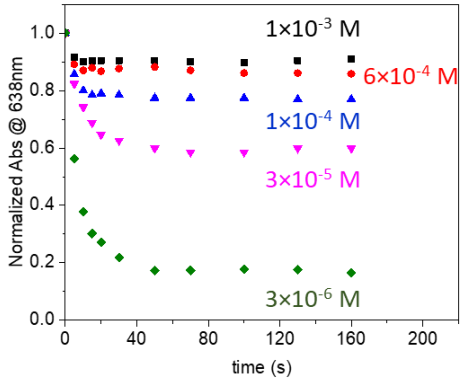

Figure 3.3 The absorption decay of DASA in toluene under 638 nm irradiation at 1.0 mW/cm^2. The PSS absorbance is lower due to a slower k_{back}.

Given that the molecules are free to diffuse and interact in the liquids, we decided to see whether the reaction was also affected by concentration in solid polymer matrices where diffusion is inhibited. The evolution of the **DASA** absorption with concentration is shown for both polymethyl(methacrylate) (PMMA) in **Figure 3.4a** and for polystyrene

(PS) in **Figure 3.4b**. The absorption spectrum of a neat **DASA** film, deposited by solvent evaporation, is also shown in **Figure 3.4b**.

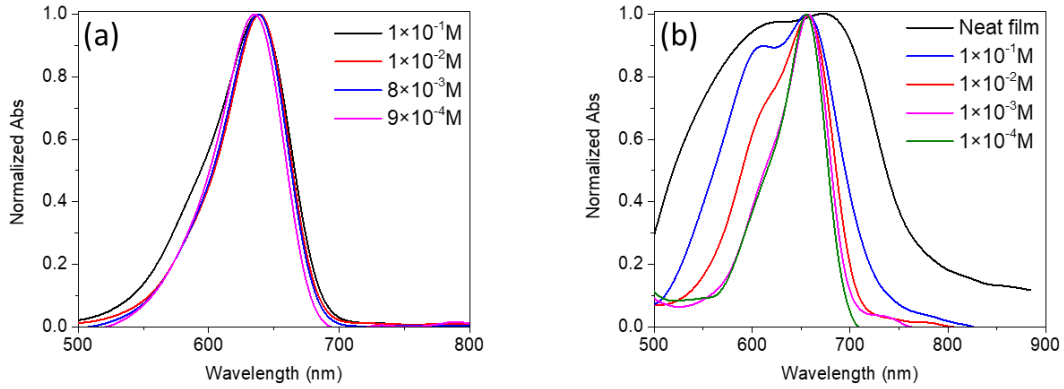

Figure 3.4 a) Normalized absorption spectra of **DASA**/PMMA polymer films with varying **DASA** concentrations. The main peak broadens slightly only at the highest concentration, 0.1 M. **b)** Normalized absorption spectra of **DASA**/PS polymer films with varying **DASA** concentrations. In this polymer, the lineshape broadening starting at 10^{-2} M. Also shown is the absorption of a neat film.

Table 3.2 Full width half max (FWHM) & peak absorbance of DASA/polymer films

PMMA			PS		
Concentration (M)	FWHM (cm^{-1})	λ_{peak} (nm)	Concentration (M)	FWHM (cm^{-1})	λ_{peak} (nm)
1×10^{-1}	138,831	637.7	Neat film	46,089	674.1
1×10^{-2}	165,371	668.7	1×10^{-1}	74,482	656.7
8×10^{-3}	167,842	638.1	1×10^{-2}	104,134	656.6
9×10^{-4}	170,416	635.6	1×10^{-3}	146,049	657.3
			1×10^{-4}	158,403	655.1

Only in PS at the highest concentrations (>10^{-2} M) are clear signatures of aggregation seen: a broadening of the spectrum and an enhancement of the 0-1 vibronic feature, both of which are probably the result of weakly interacting H-type molecular aggregates.[35] In the neat film, the absorption broadened considerably and both blue- and red-shifted features became

prominent. The varying peak positions and widths of the spectra in **Figure 3.4** are tabulated in **Table 3.2** Full width half max (FWHM) & peak absorbance of DASA/polymer films. Powder x-ray diffraction and polarized light microscopy measurements indicated that the solution-cast neat film was a mixture of crystalline and amorphous regions (**Figure 3.5**). Its absorption lineshape can be understood qualitatively in terms of a statistical mixture of H-type and J-type aggregates.

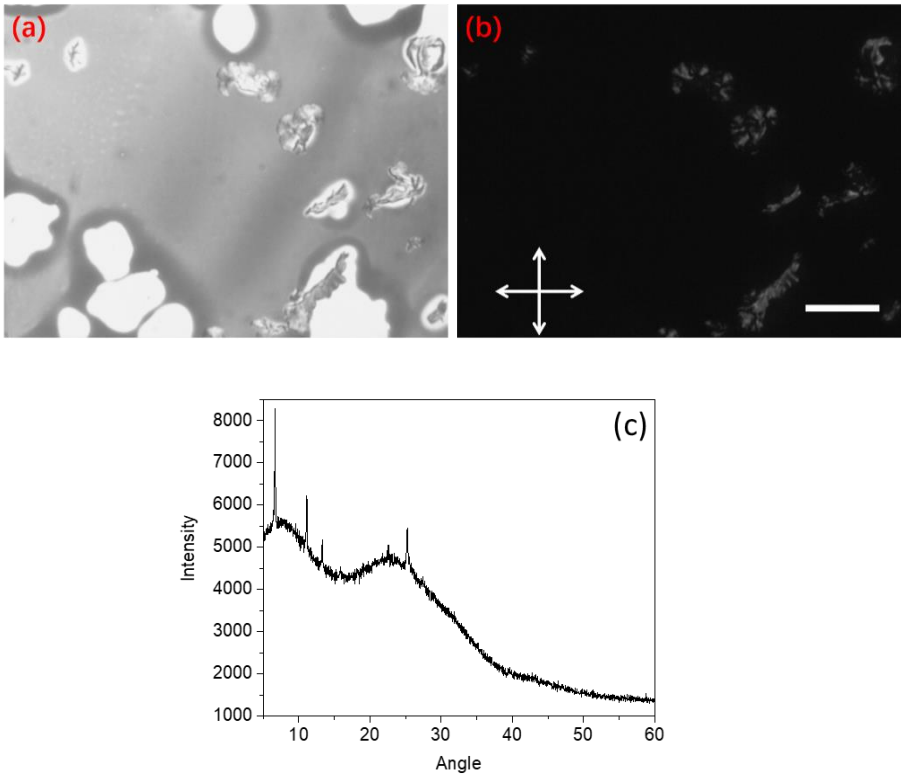

Figure 3.5 a) Optical microscope image of DASA neat film at bright field. **b)** Cross-polarized microscope image of DASA neat film of the same region as **a)**. Only a few regions exhibit birefringence. Scale bar: 50 μm. **c)** X-ray diffraction pattern of DASA neat film.

While there are some differences in the concentration dependence of the absorption spectrum, the polymer blends all showed the same kinetic trends as the liquids: a slowdown

in photoswitching as the photochrome concentration is increased. Data for **DASA**/PMMA films are plotted in **Figure 3.6**, along with the results for the neat film. As with the liquid samples, the ability of **DASA** to photoisomerize decreases dramatically as the **DASA** concentration increases. Similar results are observed for **DASA** in PS (**Figure 3.7**).

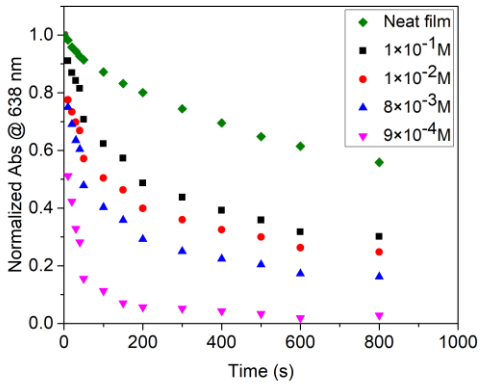

Figure 3.6 Decay of the **DASA** absorption in PMMA films monitored at 638 nm under irradiation with an intensity of 11.4 mW/cm^2. The higher intensity was needed to achieve conversion on timescales similar to those in the solutions.

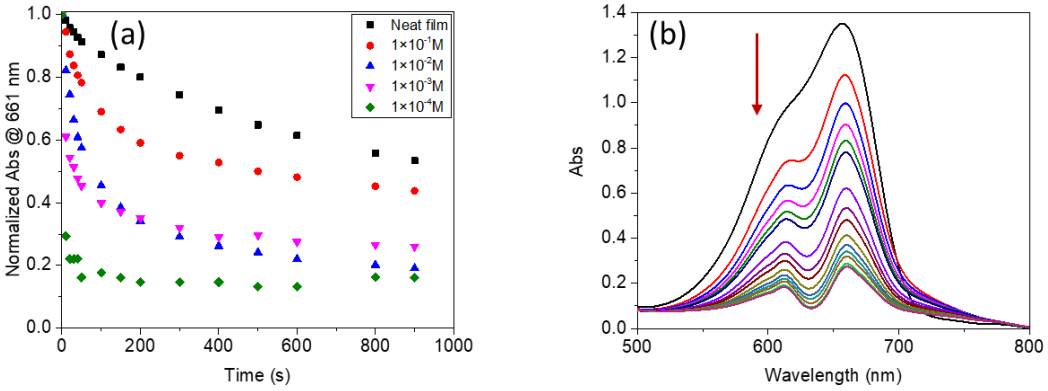

Figure 3.7 a) The decay of absorption of DASA/PS films monitored at 661 nm (peak absorbance). **b)** A sample of the decay of absorption of a DASA/PS film (1×10^{-2} M). The dip in the absorption at 638 nm is caused by the irradiation source.

We were curious to see whether another commonly used photochromic molecule would exhibit a similar concentration dependence. We tested the spiropyran derivative 1,3,3-trimethylindolino-6'-nitrobenzopyrylospiran, which undergoes a ring-opening isomerization to the more polar merocyanine form[36], somewhat analogous to the **DASA** isomerization. Over the concentration range 10^{-6}-10^{-3} M, we found no systematic dependence of either the forward or back reaction rates to within the error (**Table 3.3**). Even in neat films, this spiropyran derivative underwent an obvious color change after a few minutes of exposure to 365 nm light, whereas the **DASA** film showed almost no change for the same photon dose at 638 nm. While this is not a survey of all photochromic molecule classes, it does support that the concentration effect is not a general phenomenon.

Table 3.3 The quantum yields and k_{back} of 1,3,3-trimethylindolino-6'-nitrobenzopyrylospiran.

Concentration (M)	k_{back} (s^{-1}) ($\times10^{-3}$)	$k_{forward}$ (s^{-1}) ($\times10^{-3}$)	Φ (%)
9.1×10^{-3}	15±3	30±3	12 ±2
1.4×10^{-4}	14 ±5	16±4	7±2
1.4×10^{-5}	21±4	35±3	15±2
1.4×10^{-6}	20±5	21±3	9±2

In order to quantify the effects of concentration on the **DASA** reaction rates, we can model the isomerization in terms of the simple two-state model given in **Figure 3.8**.[37] We start with the rate equations:

$$\frac{dN_{open}}{dt} = -\sigma I \phi_{OC} N_{open} + k_{back} N_{closed} \quad (1a)$$

$$\frac{dN_{closed}}{dt} = +\sigma I \phi_{OC} N_{open} - k_{back} N_{closed} \quad (1b)$$

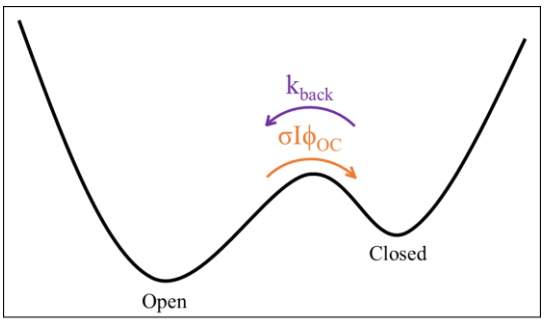

Figure 3.8 Simple two-state model of the isomerization of **DASA**. The net forward isomerization rate depends on light intensity I, absorption cross section σ, and the net quantum yield for the open→closed reaction, ϕ_{OC}. After the light is turned off, **DASA** thermally reverts back to the open form at the rate of k_{back}.

where N_{open} and N_{closed} are the concentrations of the open and closed-ring isomers, respectively. $N_{open}+N_{closed} = N_0$ where N_0 is the total chromophore concentration. σ is the absorption cross section of the open form at the irradiation wavelength, ϕ_{OC} is the quantum yield for going from the open to closed form, and k_{back} is the thermal back reaction rate. We assume that before light exposure, all the **DASA** photochromes reside in the open state, $N_{open}(0)=N_0$. While there can be appreciable closed population for some **DASA** derivatives[29], at least 95% of the third-generation molecule studied here has been shown to reside in the open form at equilibrium.[34] The time-dependence of N_{open}, which is experimentally monitored via its visible absorbance (*Abs*), is given by:

$$Abs \propto N_{open}(t) = \frac{k_{back} N_0}{k} + N_0 \left(1 - \frac{k_{back}}{k}\right) e^{-kt} \qquad (2)$$

where $k = \sigma I \phi_{OC} + k_{back}$ is the initial decay rate of the open-form absorbance. Direct extraction of the initial decay rate k from the curves in **Figure 3.2** and **Figure 3.6** is

hampered by the limited acquisition rate of the absorption spectrometer. To measure k_{back} at different concentrations, we monitored the absorption recovery time after the 638 nm irradiation was suddenly removed. In **Figure 3.9a** we plot the absorbance recovery for different **DASA** concentrations in toluene, along with fits to the exponential recovery function

$$Abs(t) = Abs(\infty) - Abs(0)e^{-k_{back}t} \tag{3}$$

where $Abs(\infty)$-$Abs(0)$ is the absorbance right after the 638 nm light is removed and $Abs(\infty)$ is the fully recovered **DASA** absorbance. The curves can all be adequately fit using Equation (3), and we find k_{back} increases by a factor of 7 over this concentration range. In PMMA, we find that the recovery is much slower than in solution (**Figure 3.9b**), but again there is a strong concentration dependence. To determine ϕ_{OC} for the forward reaction, we take advantage of the fact that the ratio of the PSS absorbance to the initial absorbance is given by

$$\frac{N_{open}(\infty)}{N_{open}(0)} = \frac{k_{back}}{k} = \frac{k_{back}}{\sigma I \phi_{OC} + k_{back}} \tag{4}$$

and can be measured with high precision. This ratio, along with the measured values for k_{back}, allowed us to extract values for the forward quantum yield ϕ_{OC}, given a σ(638 nm)=3×10^{-16} cm^2 and a measured intensity of 3.2×10^{15} photons/s/cm^2 (3.6×10^{16} photons/s/cm^2 in polymer films).

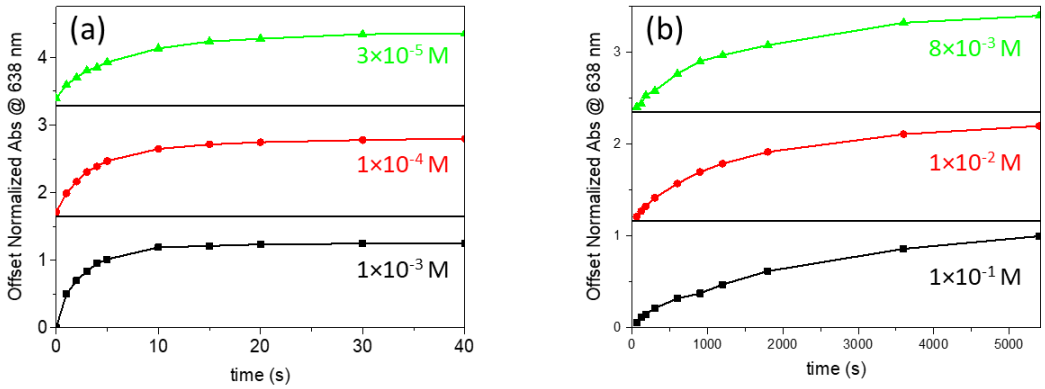

Figure 3.9 a) Absorption recovery curves for different **DASA** concentrations in toluene, monitored at 638 nm, reflecting the decrease in k_{back}. **b)** Absorption recovery curves for different **DASA** concentrations in PMMA, monitored at 638 nm. Unlike the behavior in toluene, k_{back} increases as the **DASA** concentration increases. Exponential fits using Equation (3) to these data allow us to extract the k_{back} values given in **Table 3.4**.

Given the complicated multistep nature of the **DASA** isomerization, the simple two-state model's lack of intermediate states and assumption of negligible open→closed isomerization in the absence of light may limit its absolute accuracy. Nevertheless, it does provide a convenient way to quantify DASA's overall photophysical behavior. The concentration dependence of both k_{back} and ϕ_{OC} are plotted in **Figure 3.10a** (toluene) and in **Figure 3.10b** (PMMA) and the values are summarized in **Table 3.4**. In toluene, the forward reaction is inhibited as the quantum yield drops from ϕ_{OC} =21% for [**DASA**]=10^{-6} M to ϕ_{OC} =3% for [**DASA**]=10^{-3} M, while k_{back} increases from 0.04 s^{-1} to 0.30 s^{-1}. Both effects inhibit net photoproduct formation. In PMMA, k_{back} is about 100× slower and decreases with increasing **DASA** concentration, the opposite of what is observed in the liquids. Normally, this would favor isomerization, but ϕ_{OC} decreases even more rapidly and again the net effect is to suppress the photochromism at high concentrations.

Interestingly, when the rates are plotted versus concentration in a log-log plot (**Figure 3.11**), they exhibit a power law dependence with exponents ranging from 0.3 to 0.7. The origin of this nonlinear behavior with concentration is not clear, and the uncertainties in the log-log plot slopes are sufficiently large we defer further analysis to a future study.

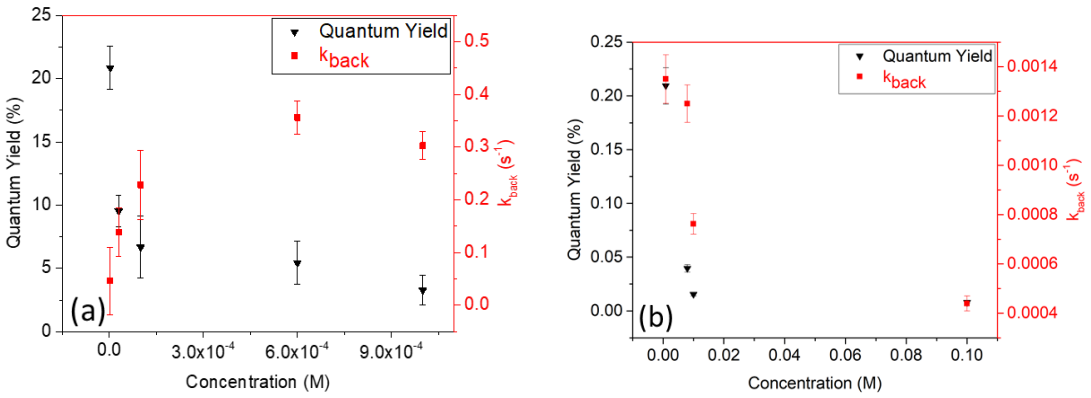

Figure 3.10 a) The quantum yield (black triangles) and k_{back} rates (red squares) are displayed for **DASA** in toluene for different **DASA** concentrations. In toluene, the QY decreases while k_{back} increases as the **DASA** concentration increases. **b)** The quantum yield (black triangles) and k_{back} rates (red squares) are displayed for **DASA** in PMMA for different **DASA** concentrations. In PMMA, both the QY and k_{back} values decrease as concentration is increased.

Table 3.4 Tabulated quantum yields and recovery rates of DASA in toluene, chloroform, and PMMA.

Toluene			**Chloroform**		**PMMA**		
Concentration (M)	k_{back} (s^{-1})	Φ_{OC} (%)	k_{back} (s^{-1})	Φ_{OC} (%)	Concentration (M)	k_{back} (s^{-1}) ($\times10^{-4}$)	Φ_{OC} (%) ($\times10^{-3}$)
1×10^{-3}	0.303±0.008	3.3±1.2	0.059±0.001	0.616±0.150	1×10^{-1}	4.4±0.3	7.9±0.9
6×10^{-4}	0.356±0.011	5.4±1.7	--	--	1×10^{-2}	7.6±0.4	15.6±1.4
1×10^{-4}	0.228±0.015	6.7±2.4	0.034±0.001	0.799±0.165	8×10^{-3}	12.5±0.8	39.6±3.5
3×10^{-5}	0.139±0.006	9.5±1.3	0.029±0.001	1.38±0.29	9×10^{-4}	13.5±1.0	209±17
3×10^{-6}	0.046±0.003	21±1.7	--	--			

The net quantum yield ϕ_{OC} is actually the product of yields for each reaction step shown in **Scheme 3.1**. The question then becomes which stage is responsible for the

concentration effect. The first step, *cis*→*trans* isomerization, can be monitored using femtosecond transient absorption spectroscopy. We measured the picosecond dynamics after excitation of the **DASA** at 640 nm for two different concentrations in chloroform, 10^{-5} M and 10^{-3} M. From **Table 3.4**, ϕ_{OC} changes by a factor of 2 over this concentration range. A series of time-resolved spectra for different pump-probe delays are shown in **Figure 3.13a**. The transient spectra are typical of the **DASA** class of compounds, with a strong excited state absorption feature at 650 nm that decays as isomerization and internal conversion remove population from the excited state.[38, 39] The excited state decay dynamics, measured at the probe wavelength of 648 nm, are overlaid in **Figure 3.13b** and are identical. The decay times are the same to within the experimental error, τ_{ex} = 25±2 ps.

After the excited state decay, the derivative lineshape left at longer delays is proportional to the amount of *trans* isomer formed, since its absorption is slightly redshifted relative to that of the *cis* isomer. Since the absorption is not affected by concentration, the size of this feature, relative to the initial bleach, should be proportional to the *cis*→*trans* photoisomerization yield. Here we assume that secondary photon absorption events by the trans isomer, which have been shown to facilitate later isomerization events in gas phase experiments [33], are absent in our experiment. This is justified by the fact that the pump pulse is only present during the first 200 fs of the isomerization process and cannot re-excite the *trans* isomer which is formed after several ps. The size of the long-time derivative feature, relative to the initial bleach, is identical

for both concentrations (**Figure 3.12**). There is no evidence that the initial *cis*→*trans* reaction step is affected by concentration.

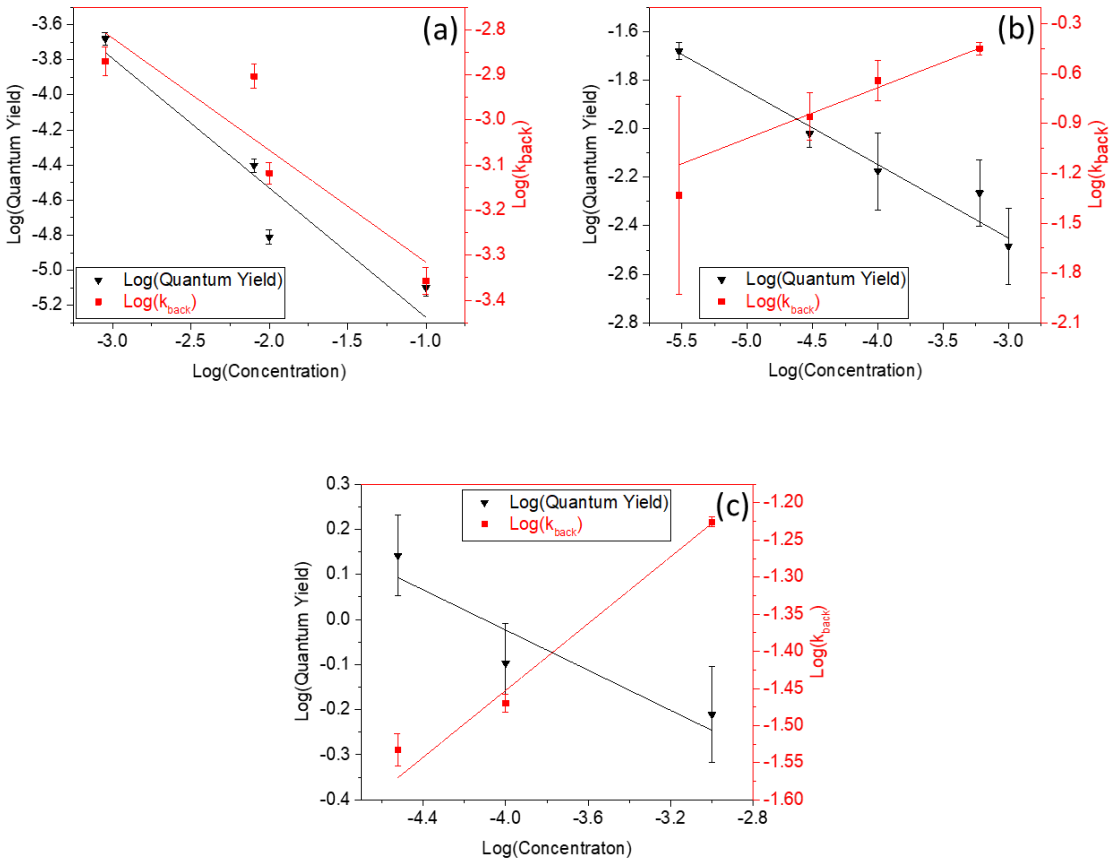

Figure 3.11 Log(QY) and log(k_{back})-log[DASA] plots for DASA in PMMA **a)**, toluene **b)**, and chloroform **c)** are shown. A linear fit could is also shown for all cases. The slopes of k_{back} and the quantum yield in PMMA samples are -0.25±0.09 and -0.74±0.17, respectively. The slopes for the toluene samples are +0.31±0.03 and -0.30±0.02. The slopes of the chloroform samples are +0.23±0.02 and -0.22±0.09.

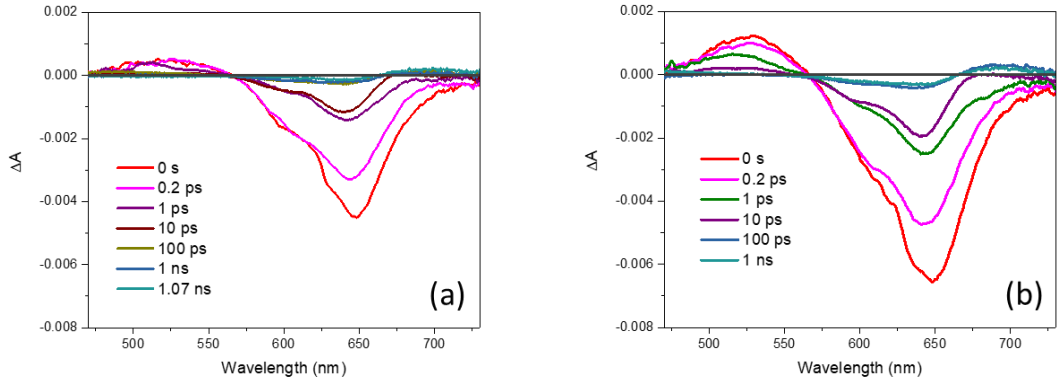

Figure 3.12 Raw transient absorption spectra of both **a)** 30 μM and **b)** 1 mM DASA in $CHCl_3$. The long-time derivative feature between both concentrations are comparable relative to their initial bleaches.

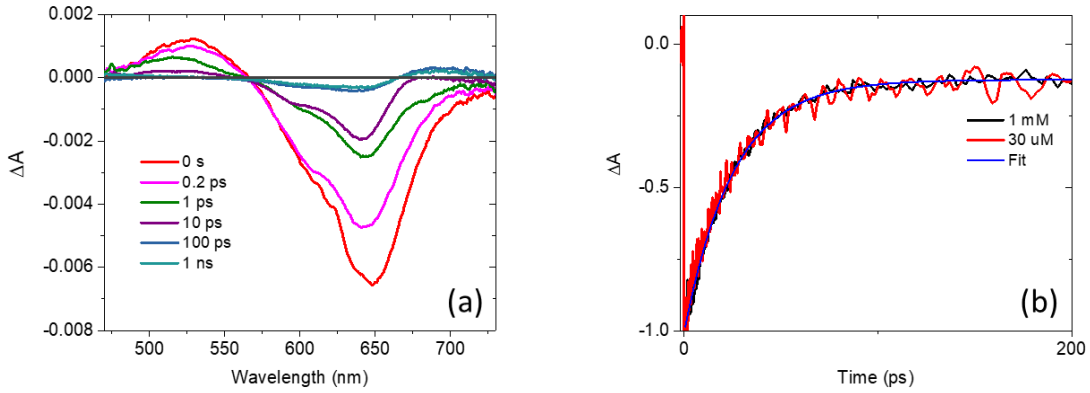

Figure 3.13 a) Transient absorbance spectra of **DASA** in chlororoform **(**10^{-3} M) for different probe delays. At early times, the positive signal at 528 nm reflects excited state absorbance and the negative signal at 648 nm reflects a ground state bleach and excited state stimulated emission of the Z isomer. After 100 ps the excited state features decay to zero, and there is a new positive signal at 695 nm representing the absorbance of the E isomer, with a negative bleach signal at around 640 nm. **B)** Normalized decay of the stimulated emission feature at 648 nm shows that the Z→E isomerization lifetime for the 1 mM and 30 uM concentrations are identical.

The mechanism for the changes in k_{back} and ϕ_{OC} at high **DASA** concentrations is not clear. We have already ruled out any effects on the *cis*→*trans* step, but it is possible

that later steps along the pathway are inhibited. One possible explanation is that steric interference prevents the subsequent conformational change and ring-closing, both of which require substantial atomic rearrangements. But the fact that the inhibition occurs in both liquid and solid-state environments is not consistent with this explanation. Steric inhibition by neighboring **DASA** molecules in a liquid environment is hard to envision. In the solid-state, it is not clear why neighboring **DASA** molecules would be more sterically obstructing than neighboring polymer chains. Such an inhibition has been observed for azobenzene/PMMA blends, but only when the azobenzene begins to crystallize inside the polymer.[40] Furthermore, if the molecules are close enough to sterically interact with each other, we would expect to see some sign of this association in the absorption spectrum. **DASA**'s large S_0-S_1 transition dipole moment should lead to excitonic coupling and the appearance of excitonic electronic states. However, changes in the absorption spectrum are only observed at the highest concentrations in PS, while the spectrum in liquids and PMMA do not show changes at any concentration. The absorption data in **Figure 3.1** and **Figure 3.4** show that **DASA** does not form close aggregates at concentrations where there is significant inhibition of the photoisomerization.

We should note that exciton state formation itself can also provide a mechanism for changes in photoreactivity. This mechanism does not require physical contact between the molecule and would be active in both liquid and solid environments. Excitonic coupling has been implicated in lowered photoisomerization quantum yields for aggregated azobenzene[41-44] and merocyanine photochromes.[45] This mechanism does not appear to be operative for **DASA**, however. First, as described above, the photoisomerization inhibition

is present in samples where there is no sign of excitonic coupling. Second, at 10^{-3} M, where ϕ_{OC} has decreased by a factor of 10, the average distance between molecules is on the order of 10 nm, much greater than the typical distance over which excitonic interactions occur. Third, excitonic coupling would most likely affect the excited state reactivity, since this is the state that splits and shifts under the influence of the dipole-dipole interaction. As shown above, there is no evidence that the rate of the excited state *cis*→*trans* reaction is perturbed at higher concentrations.

In polymers, it is possible that adding **DASA** changes the host mechanical properties in a way that makes the local environment more resistant to the isomerization. We checked whether **DASA** changes the mechanical properties of the polymer matrix by measuring the glass transition temperature (T_g) of PS as a function of **DASA** concentration. A stiffening of the polymer matrix would be expected to raise the T_g. A T_g value of 105ºC was found for neat PS, in good agreement with literature values and the manufacturer's specification.[46] Adding **DASA** up to concentrations of 10^{-3} M resulted in a slight (~1°C) decrease in T_g (**Figure 3.14**), as usually observed when small molecule additives are mixed with a polymer.[47] Again, there was no evidence of a physical effect of **DASA** that would make the host less amenable to the conformational changes needed for photoisomerization.

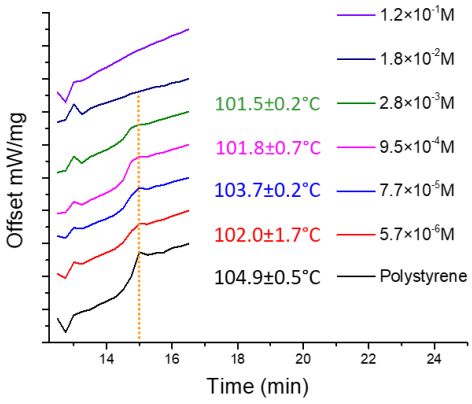

Figure 3.14 T_g of pure PS and various concentrations of DASA-PS were collected via DSC. The T_g appears to decrease slightly as concentration is increased. At the two highest concentrations, the T_g diminishes and is not observed.

Previous reports of concentration dependent photoisomerization are rare and are sometimes reported without comment on the mechanism.[48] Excited state quenching by collisions or noncovalent complex formation have been reported[49, 50] but can be ruled out in this case based on the transient absorption results. Density functional theory calculations estimate a ground state dipole moment on the order of 15 Debye for closely related molecules[51], so it is likely that **DASA** can support long-range electrostatic interactions that can perturb the proton transfer and electrocyclization steps necessary to complete the isomerization. For example, electrostatic effects due to high ionic strength have been shown to slow down intramolecular proton transfer rates in liquids.[52] We are currently pursuing this line of reasoning by measuring photoisomerization rates for dilute **DASA** solutions in a variety of solvents, including ionic liquids. More specific intermolecular interactions may also play a role. For example, there are several reports of ground state isomerization reactions that are inhibited by ion-pairing interactions.[53, 54] Beves and

coworkers have recently shown that the colorless closed form of **DASA** can exist as both enolate and diketone forms, and the enolate form is favored at high concentrations.[29] They suggest that hydrogen-bonded pairs of cyclic **DASA** molecules can be formed in solution, providing a possible concentration dependent intermediate that could affect the kinetics of forward and backward isomerizations. Finally, it is likely that multiple factors affect the overall photoisomerization yield and recovery. From the data in **Figure 3.10**, higher **DASA** concentrations reduce ϕ_{OC} in both liquids and solids. Meanwhile, k_{back} increases in liquids but decreases in the polymers. The different effects in different hosts suggest that the concentration effects depend on the diffusivity of the **DASA** molecules. Additional experiments and theory will probably be needed to sort out the mechanisms responsible for the concentration dependence of the rates.

3.5 Conclusion

The results in this chapter identify a new effect in the photophysics of **DASA** photochromes: the dramatic inhibition of the photoisomerization with increasing photochrome concentration. Preliminary experiments in our labs indicate that this inhibition is a general effect, observed for different **DASA** derivatives and across a wide variety of solid and liquid hosts. We can eliminate steric and excitonic interactions as possible mechanisms for this inhibition. Femtosecond transient absorption experiments show that the fast *cis*→*trans* step of the isomerization is not affected by concentration. We suspect that long-range Coulombic interactions interfere with the slower electrocyclization stage of the isomerization. Determining the physical origin of the photoisomerization inhibition at high concentrations is necessary in order to design new **DASA** derivatives that

avoid this problem. Many other photochromic molecules (spiropyrans, diarylethenes, azobenzenes) exhibit strong photochromic behavior even in neat crystals or amorphous films, where concentrations are on the order of 1-10 M. DASAs provide an opportunity to expand the molecular toolbox for photomechanical materials if they can maintain their favorable photochromic properties at similar concentrations.

3.6 References

(1) Durr, H.; Bouas-Laurent, H. *Photochromism : Molecules and Systems*; Elsevier, 1990.

(2) Irie, M.; Yokoyama, Y.; Seki, T. *New Frontiers in Photochromism*; Springer, 2013.

(3) Saltiel, J.; Townsend, D. E.; Sykes, A. The Quantum Chain Process in the Sensitized Cis-Trans Photoisomerization of 1 ,3-Dienes. *J. Am. Chem. Soc.* **1973**, *95*, 5968-5973.

(4) Kuzmanich, G.; Gard, M. N.; Garcia-Garibay, M. A. Photonic Amplification by a Singlet-State Quantum Chain Reaction in the Photodecarbonylation of Crystalline Diarylcyclopropenones. *J. Am. Chem. Soc.* **2009**, *131*, 11606–11614.

(5) Doan, S. C.; Kuzmanich, G.; Gard, M. N.; Garcia-Garibay, M. A.; Schwartz, B. J. Ultrafast Spectroscopic Observation of a Quantum Chain Reaction: The Photodecarbonylation of Nanocrystalline Diphenylcyclopropenone. *J. Phys. Chem. Lett.* **2012**, *3*, 81−86.

(6) Kim, T.; Zhu, L.; Al-Kaysi, R. O.; Bardeen, C. J. Organic Photomechanical Materials. *ChemPhysChem* **2014**, *15*, 400-414.

(7) White, T. J. Photomechanical Materials, Composites, and Systems. 1 ed.; Wiley: Hoboken, New Jersey, 2017.

(8) Barrett, C. J.; Mamiya, J.; Yager, K. G.; Ikeda, T. Photomechanical Effects in Azobenzene-Containing Soft Materials. *Soft Matter* **2007**, *3*, 1249-1261.

(9) Ikeda, T.; Mamiya, J.; Yu, Y. Photomechanics of liquid-crystalline elastomers and other polymers. *Angew. Chem. Int. Ed.* **2007**, *46*, 506-528.

(10) Iamsaard, S.; Abhoff, S. J.; Matt, B.; Kudernac, T.; Cornelissen, J. J. L. M.; Fletcher, S. P.; Katsonis, N. Conversion of Light into Macroscopic Helical Motion. *Nat. Chem.* **2014**, *6*, 229-235.

(11) Gelebart, A. H.; Mulder, D. J.; Varga, M.; Konya, A.; Vantomme, G.; Meijer, E. W.; Selinger, R. L. B.; Broer, D. J. Making Waves in a Photoactive Polymer Film. *Nature* **2017**, *546*, 632-636.

(12) Al-Kaysi, R. O.; Muller, A. M.; Bardeen, C. J. Photochemically driven shape changes of crystalline organic nanorods. *J. Am. Chem. Soc.* **2006**, *128*, 15938-15939.

(13) Zhu, L.; Tong, F.; Zaghloul, N.; Baz, O.; Bardeen, C. J.; Al-Kaysi, R. O. Characterization of a P-Type Photomechanical Molecular Crystal Based on the

E→Z Photoisomerization of 9-Divinylanthracene Malonitrile. *J. Mater. Chem. C* **2016**, *4*, 8245-8452.

(14) Medishetty, R.; Husain, A.; Bai, Z.; Runceviski, T.; Dinnebier, R. E.; Naumov, P.; Vittal, J. J. Single crystals popping under UV light: a photosalient effect triggered by a [2+2] cycloaddition reaction. *Angew. Chem. Int. Ed.* **2014**, *53*, 5907-5911.

(15) Naumov, P.; Chizhik, S.; Panda, M. K.; Nath, N. K.; Boldyreva, E. Mechanically Responsive Molecular Crystals. *Chem. Rev.* **2015**, *115*, 12440-12490.

(16) Bushuyev, O. S.; Tomberg, A.; Friscic, T.; Barrett, C. J. Shaping Cyrstals with Light: Crystal-to-Crystal Isomerization and Photomechanical Effect in Fluorinated Azobenzenes. *J. Am. Chem. Soc.* **2013**, *135*, 12556-12559.

(17) Koshima, H.; Takechi, K.; Uchimoto, H.; Shiro, M.; Hashizume, D. Photmechanical bending of salicylideneaniline crystals. *Chem. Commun.* **2011**, *47*, 11423-11425.

(18) Koshima, H.; Nakaya, H.; Uchimoto, H.; Ojima, N. Photomechanical motion of furylfulgide crystals. *Chem. Lett.* **2012**, *41*, 107-109.

(19) Kobatake, S.; Takami, S.; Muto, H.; Ishikawa, T.; Irie, M. Rapid and reversible shape changes of molecular crystals on photoirradiation. *Nature* **2007**, *446*, 778-781.

(20) Morimoto, M.; Irie, M. A diarylethene cocrystal that converts light into mechanical work. *J. Am. Chem. Soc.* **2010**, *132*, 14172-14178.

(21) Kitagawa, D.; Nishi, H.; Kobatake, S. Photoinduced twisting of a photochromic diarylethene crystal. *Angew. Chem. Int. Ed.* **2013**, *52*, 9320-9322.

(22) Kitagawa, D.; Kawasaki, K.; Tanaka, R.; Kobatake, S. Mechanical Behavior of Molecular Crystals Induced by Combination of Photochromic Reaction and Reversible Single-Crystal-to-Single-Crystal Phase Transition. *Chem. Mater.* **2017**, *29*, 7524-7529.

(23) Bleger, D.; Hecht, S. Visible-Light-Activated Molecular Switches. *Angew. Chem. Int. Ed.* **2015**, *54*, 11338-11349.

(24) Helmy, S.; Leibfarth, F. A.; Oh, S.; Poelma, J. E.; Hawker, C. J.; Alaniz, J. R. d. Photoswitching Using Visible Light: A New Class of Organic Photochromic Molecules. *J. Am. Chem. Soc.* **2014**, *136*, 8169−8172.

(25) Helmy, S.; Oh, S.; Leibfarth, F. A.; Hawker, C. J.; Alaniz, J. R. d. Design and Synthesis of Donor−Acceptor Stenhouse Adducts: A Visible Light Photoswitch Derived from Furfural. *J. Org. Chem.* **2014**, *79*, 11316−11329.

(26) Hemmer, J. R.; Poelma, S. O.; Treat, N.; Page, Z. A.; Dolinski, N. D.; Diaz, Y. J.; Tomlinson, W.; Clark, K. D.; Hooper, J. P.; Hawker, C.; et al. Tunable Visible and Near Infrared Photoswitches. *J. Am. Chem. Soc.* **2016**, *138*, 13960−13966.

(27) Lerch, M. M.; Szymanski, W.; Feringa, B. L. The (Photo)chemistry of Stenhouse Photoswitches: Guiding Principles and System Design. *Chem. Soc. Rev.* **2018**, *47*, 1910-1937.

(28) Mallo, N.; Brown, P. T.; Iranmanesh, H.; MacDonald, T. S. C.; Teusner, M. J.; Harper, J. B.; Ball, G. E.; Beves, J. E. Photochromic Switching Behaviour of Donor–Acceptor Stenhouse Adducts in Organic Solvents. *Chem. Commun.* **2016**, *52*, 13576-13579.

(29) Mallo, N.; Foley, E. D.; Iranmanesh, H.; Kennedy, A. D. W.; Luis, E. T.; Ho, J.; Harper, J. B.; Beves, J. E. Structure–Function Relationships of Donor–Acceptor Stenhouse Adduct Photochromic Switches. *Chem. Sci.* **2018**, *9*, 8242-8252.

(30) Lerch, M. M.; Medved, M.; Lapini, A.; Laurent, A. D.; Iagatti, A.; Bussotti, L.; Szymanski, W.; Buma, W. J.; Foggi, P.; Donato, M. D.; et al. Tailoring Photoisomerization Pathways in Donor−Acceptor Stenhouse Adducts: The Role of the Hydroxy Group. *J. Phys. Chem. A* **2018**, *122*, 955−964.

(31) Aiken, S.; Edgar, R. J. L.; Gabbutt, C. D.; Heron, B. M.; Hobson, P. A. Negatively Photochromic Organic Compounds: Exploring the Dark Side. *Dyes Pigm.* **2018**, *149*, 92-121.

(32) Lerch, M. M.; Wezenberg, S. J.; Szymanski, W.; Feringa, B. L. Unraveling the Photoswitching Mechanism in Donor−Acceptor Stenhouse Adducts. *J. Am. Chem. Soc.* **2016**, *138*, 6344−6347.

(33) Bull, J. N.; Carrascosa, E.; Mallo, N.; Scholz, M. S.; Silva, G. d.; Beves, J. E.; Bieske, E. J. Photoswitching an Isolated Donor−Acceptor Stenhouse Adduct. *J. Phys. Chem. Lett.* **2018**, *9*, 665−671.

(34) Hemmer, J. R.; Page, Z. A.; Clark, K. D.; Stricker, F.; Dolinski, N. D.; Hawker, C. J.; Alaniz, J. R. d. Controlling Dark Equilibria and Enhancing Donor−Acceptor Stenhouse Adduct Photoswitching Properties through Carbon Acid Design. *J. Am. Chem. Soc.* **2018**, *140*, 10425−10429.

(35) Spano, F. C. The Spectral Signatures of Frenkel Polarons in H- and J-Aggregates. *Acc. Chem. Res.* **2010**, *43*, 429-439.

(36) Klajn, R. Spiropyran-Based Dynamic Materials. *Chem. Soc. Rev.* **2014**, *43*, 148-184.

(37) Hanson, K. M.; Narayanan, S.; Nichols, V. M.; Bardeen, C. J. Photochemical Degradation of the UV filter Octyl Methoxycinnamate in Solution and in Aggregates. *Photochem. Photobio. Sci.* **2015**, *14*, 1607-1616.

(38) Donato, M. D.; Lerch, M. M.; Lapini, A.; Laurent, A. l. D.; Iagatti, A.; Bussotti, L.; Ihrig, S. P.; Medved, M.; Jacquemin, D.; Szymański, W.; et al. Shedding Light on the Photoisomerization Pathway of Donor−Acceptor Stenhouse Adducts. *J. Am. Chem. Soc.* **2017**, *139*, 15596−15599.

(39) Lerch, M. M.; Donato, M. D.; Laurent, A. D.; Medved, M.; Iagatti, A.; Bussotti, L.; Lapini, A.; Buma, W. J.; Foggi, P.; Szymanski, W.; et al. Solvent Effects on the Actinic Step of Donor–Acceptor Stenhouse Adduct Photoswitching. *Angew. Chem. Int. Ed.* **2018**, *130*, 8195 –8200.

(40) Pakula, C.; Hanisch, C.; Zaporojtchenko, V.; Strunskus, T.; Bornholdt, C.; Zargarani, D.; Herges, R.; Faupel, F. Optical Switching Behavior of Azobenzene/PMMA Blends with High Chromophore Concentration. *J. Mater. Sci.* **2011**, *46*, 2488–2494.

(41) Gahl, C.; Schmidt, R.; Brete, D.; McNellis, E. R.; Freyer, W.; Carley, R.; Reuter, K.; Weinelt, M. Structure and Excitonic Coupling in Self-Assembled Monolayers of Azobenzene-Functionalized Alkanethiols. *J. Am. Chem. Soc.* **2010**, *132*, 1831–1838.

(42) Titov, E.; Saalfrank, P. Exciton Splitting of Adsorbed and Free 4-Nitroazobenzene Dimers: A Quantum Chemical Study. *J. Phys. Chem. A* **2016**, *120*, 3055−3070.

(43) Utecht, M.; Klamroth, T.; Saalfrank, P. Optical Absorption and Excitonic Coupling in Azobenzenes Forming Self-Assembled Monolayers: a Study Based on Density Functional Fheory. *Phys. Chem. Chem. Phys.* **2011**, *13*, 21608–21614.

(44) Cocchi, C.; Moldt, T.; Gahl, C.; Weinelt, M.; Draxl, C. Optical Properties of Azobenzene-Functionalized Self-Assembled Monolayers: Intermolecular Coupling and Many-Body Interactions. *J. Chem. Phys.* **2016**, *145*, 234701/234701-234711.

(45) Eckhardt, H.; Bose, A.; Krongauzt, V. A. Formation of Molecular H- and J-stacks by the Spiropyran-Merocyanine Transformation in a Polymer Matrix. *Polymer* **1987**, *28*, 1959-1964.

(46) Rieger, J. The Glass Transiton Temperature of Polystyrene: Results of a Round Robin Test. *J. Therm. Anal.* **1996**, *46*, 965-972.

(47) Brinke, G. t.; Karasz, F. E.; Ellis, T. S. Depression of Glass Transition Temperatures of Polymer Networks by Diluents. *Macromolecules* **1983**, *16*, 244-249.

(48) Nonaka, Y.; Shimada, J.; Nonaka, H.; Koike, N.; Aoki, N.; Hiroyuki Kobayashi; Kase, H.; Yamaguchi, K.; Suzuki, F. Photoisomerization of a Potent and Selective Adenosine A2 Antagonist, (E)-l ,3-Dipropy 1-8- (3,4-dimethoxy sty ryl) -7-methylxanthine. *J. Med. Chem.* **1993**, *36*, 3731-3733.

(49) Zimmerman, A. A.; Orlando, C. M.; Gianni, M. H.; Weiss, K. Concentration Effects in Photochemical cis-trans Isomerization. A Study of Difurylethylene and Dithienylethylene. *J. Org. Chem.* **1969**, *34*, 73-77.

(50) El-Zohry, A. M.; Zietz, B. Concentration and Solvent Effects on the Excited State Dynamics of the Solar Cell Dye D149: The Special Role of Protons. *J. Phys. Chem. C* **2013**, *117*, 6544−6553.

(51) Laurent, A. D.; Medved, M.; Jacquemin, D. Using Time-Dependent Density Functional Theory to Probe the Nature of Donor–Acceptor Stenhouse Adduct Photochromes. *Chem. Phys. Chem.* **2016**, *17*, 1846 – 1851.

(52) Joung, J. F.; Kim, S.; Park, S. Ionic Effects on the Proton Transfer Mechanism in Aqueous Solutions. *Phys. Chem. Chem. Phys.* **2017**, *19*, 25509--25517.

(53) Craze, G.-A.; Watt, I. Ion-Pairing and Aggregation Effects on Reactivity in an Intramolecular Hydride Transfer. *Tet. Lett.* **1982**, *23*, 975-978.

(54) Yano, A.; Konno, Y.; Kinoshita, E.; Yano, R. Concentration Dependence of Thermal Isomerization Process of Methyl Orange in Ethanol. *J. Photochem. Photobiol. A* **2017**, *346*, 411–415.

4. Using Small Molecule Absorbers to Create a Photothermal Wax Motor

4.1 Preface

In this chapter, photothermally induced solid→liquid organic phase change materials are discussed with the motivation as photomechanical materials. The solid→liquid phase transition that drives expansion is commonly induced by resistive heating that requires an electrical connection. The use of light to generate a phase change provides a non-contact way to power wax motors. Here it is demonstrated that small molecules can act as absorbers to enable a photoinduced solid→liquid melting transition in eicosane, a low molecular weight phase change material. Three different small molecule absorbers are utilized: (2,2,6,6-tetramethylpiperidin-1-yl)oxyl, azobenzene, and guaiazulene (GAZ). The GAZ/eicosane mixture is characterized in detail because its absorption extends out to 750 nm, opening the possibility of using near-infrared diodes as the photon source. The GAZ/eicosane composite is incorporated into a commercial wax motor assembly and 532 nm laser light is used to lift up to 400 g. The temporal response, work and force output, and efficiency are measured, and no loss of lifting capability or degradation is observed after 10 cycles of irradiation. The incorporation of small aromatic molecules with low-energy absorption features into phase change materials can provide a general way to make light powered wax motors.

4.2 Introduction

Photons provide a low-loss way to transport energy without the need for physical connections like wires. The transformation of photon energy into mechanical work can be

accomplished by the use of a photomechanical material that expands or deforms after absorbing the photons.[1] Often, these materials rely on the photochemical isomerization of organic molecules in ordered matrices like crystals or liquid crystal polymers.[2-4] Alternatively, photothermal heating can be used to generate expansion and mechanical actuation without any chemical change.[5-16] Photothermal actuation has several advantages: 1) it avoids photochemistry and possible side reactions that lead to fatigue; 2) since only absorption is required, a large variety of absorbers spanning the optical and infrared spectrum can be used; 3) heat can diffuse throughout the material beyond the optical absorption depth that limits photon penetration. These advantages are balanced by several disadvantages: 1) heating and cooling dynamics tend to occur on much longer timescales than photochemistry, leading to a slower response; 2) the material response may be sensitive to the ambient temperature; 3) the material requires a continuous supply of photons to maintain temperature and hold its position, even while not performing any work.

There are several mechanisms by which photothermal heating can generate mechanical changes, e.g., expansion. In the simplest case, vibrational excitation associated with higher temperatures causes an increase in lattice spacing, as described by the thermal expansion coefficient. Photothermally induced solid→solid phase transitions have been successfully used in variety of polymer and semiconductor systems.[17] To generate larger volume changes, solid→liquid phase transitions may be used. There exists a large class of phase change materials (PCMs) that exhibit an expansion upon melting.[18] The largest class of these materials consists of long-chain alkanes (waxes) that undergo a large (10-15%) volume expansion upon melting.[19] This volume expansion has been harnessed to do

mechanical work by a variety of wax motor devices.[20] In all commercial devices, the melting is induced by electric current passed through a resistive heating element. To realize photothermal motion, one strategy is to infuse wax into structures composed of carbon nanotubes[21-23] or two-dimensional Mxene sheets.[24] Depending on shape, these composites can give rise to dramatic photothermal motions like bending, but the wax motor utilizes the melting expansion to move a piston in a standard actuator architecture. In this type of device, the wax must be melted in its own reservoir, and photothermal actuation relies on doping the wax with nanoparticles oxide that absorb visible light[25, 26], or heating the neat wax by infrared radiation.[27, 28] But in these cases, no detailed studies of cycling, work output, or photostability have been reported. Stability is a particular concern because many wax-nanoparticle composites have been shown to undergo phase separation after a few heating-cooling cycles.[29] Recrystallization of the alkane component appears to exclude the nanoparticles, causing them to aggregate and eventually separate from the wax.

Nanoparticles that are larger than the wax molecules can be expected to interfere with alkane chain packing. One way to avoid this interference is to use small molecules that can fit in the interstitial regions of the polycrystalline wax. For example, previous workers have shown that pyrene can reside between lamellar regions of alkane layers, allowing reasonably high (millimolar) concentrations to be achieved.[30] The challenge is to identify highly soluble small molecule absorbers that can absorb light in the range where inexpensive, high power light sources operate (roughly 400-1000 nm) and then efficiently turn the absorbed photons into heat. In this chapter, we identify three different small molecule absorbers: (2,2,6,6-Tetramethylpiperidin-1-yl)oxyl (TEMPO), azobenzene

(AZOB), and guaiazulene (GAZ) that can act as photothermal agents to induce a solid→liquid melting transition in eicosane, a low molecular weight PCM. We concentrate on characterizing the properties of the GAZ/eicosane mixture, since the GAZ absorption extends past 750 nm, opening up the possibility of using inexpensive near infrared diodes as the photon source. The GAZ/eicosane composite can be incorporated into a commercial wax motor assembly and 532 nm laser light used to power the piston actuator which lifts up to 400 g. There is no loss of lifting capability or GAZ degradation after multiple cycles of irradiation. The results in this chapter demonstrate that small molecule absorbers provide a way to create photoresponsive PCMs that are stable and can generate useful actuation. This work centers on eicosane as the PCM, but the approach should be applicable to the large class of PCMs based on alkane waxes, providing a general approach for the fabrication of light powered wax motors.

4.3 Results and Discussion

Long-chain alkanes tend to crystallize easily, causing large solutes like gold (Au) nanoparticles to phase separate after a few heating-cooling cycles (**Figure 4.1**). Even when we switched to molecular solutes, we found that their solubility was strongly dependent on size.

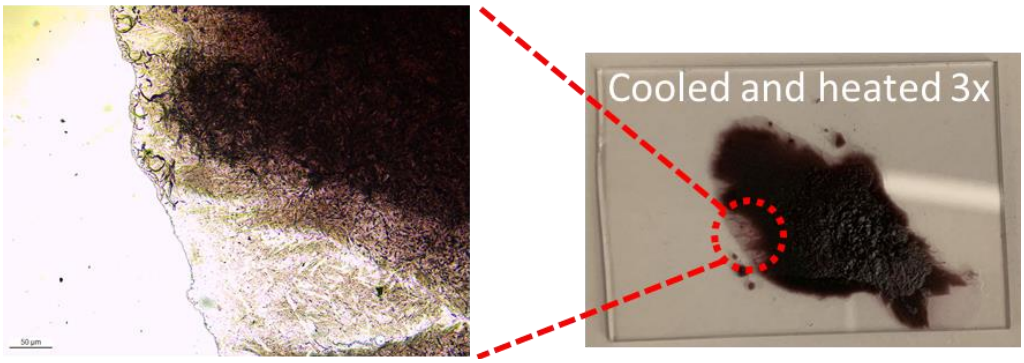

Figure 4.1 The AuNP/eicosane film after 3 melt-resolidifcation cycles is shown. The edges of the film became colorless, indicating that the AuNPs phase separated from eicosane.

For example, the maximum pyrene solubility in eicosane was found to be ~50 mM, while that of the slightly larger perylene was limited to only ~0.5 mM. Other larger dye molecules, like β-carotene and tetracene, had even lower solubilities. In order to identify viable candidates that could act as photothermal agents, we concentrated on small molecules that had 1) at most two aromatic rings; 2) absorption spectra that extended at least into the near ultraviolet (beyond 400 nm); and 3) low fluorescence quantum yields due to efficient internal conversion (IC). We examined three different small molecule absorbers: AZOB, TEMPO, and GAZ. All three had good solubility (> 10^{-2} M) in eicosane, and their absorption spectra and chemical structures are shown in **Figure 4.2**.

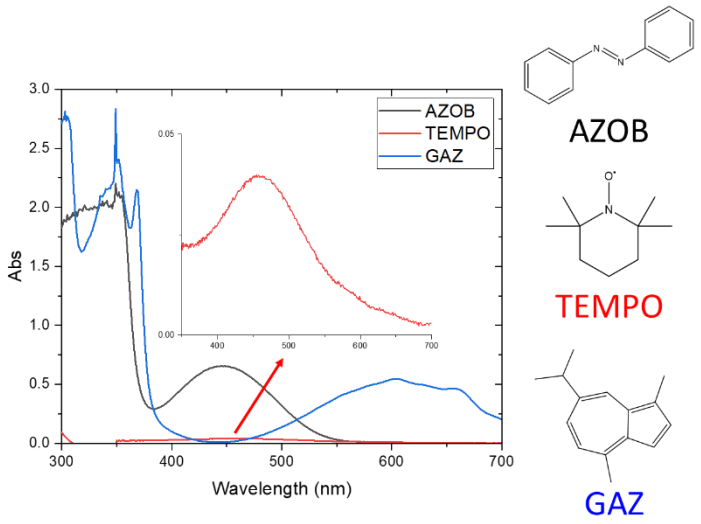

Figure 4.2 UV-Vis absorption spectra of the small molecule absorbers in eicosane (5 mM). The chemical structures of AZOB, TEMPO, and GAZ are shown to the right of the figure.

The absorption lineshapes in eicosane are very similar to those in cyclohexane (**Figure 4.3**) and show no sign of aggregation or specific molecular interactions that change the electronic structure.

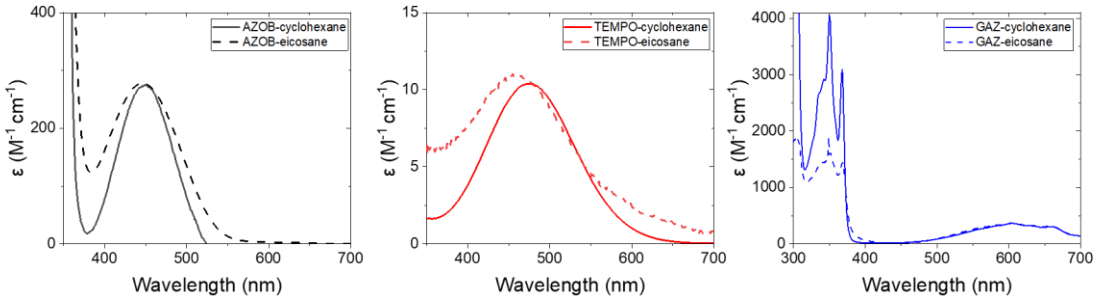

Figure 4.3 UV-Vis spectrum of the photochromes in cyclohexane (solid lines). The dotted lines are the absorption spectra of the photochromes in eicosane scaled to match the cyclohexane spectra.

The spectra in **Figure 4.2** provide a good measure of the relative absorbances but extracting absolute absorption coefficients from the solid wax data is complicated by the large

scattering background.[31] After absorption, rapid IC in AZOB is facilitated by an excited state conical intersection that also enables trans→cis isomerization[32-34], and this allows it to function as a photothermal agent.[35] TEMPO benefits from its radical structure that leads to a low energy absorbance.[36] Since we were unable to detect any fluorescence from this molecule, we assume that its excited state relaxation is also dominated by IC. Lastly, GAZ, like azulene, is a non-alternant aromatic hydrocarbon with a weak, low-energy absorption[37] and rapid IC.[38] Taken together, these molecules embody three different physical mechanisms to achieve absorption at longer wavelengths, which is desirable for a small molecule photothermal agent. Of these three, GAZ is the most promising candidate because of its low cost and absorption spectrum that extends almost to 800 nm. In the following we concentrate on characterizing the performance of this molecule, but all three are capable of supporting photoactuation of the wax motor, as shown in **Figure 4.4**.

The low absorption coefficient of GAZ's S_0-S_1 transition in the visible motivated the use of relatively high concentrations of 10 mM or more in the eicosane. The first question was whether the presence of the GAZ at these concentrations had any effect on the phase behavior of the wax. **Figure 4.5a** and **Figure 4.5b** compares the DSC curves for neat eicosane and a mixture with [GAZ]=14.3 mM.

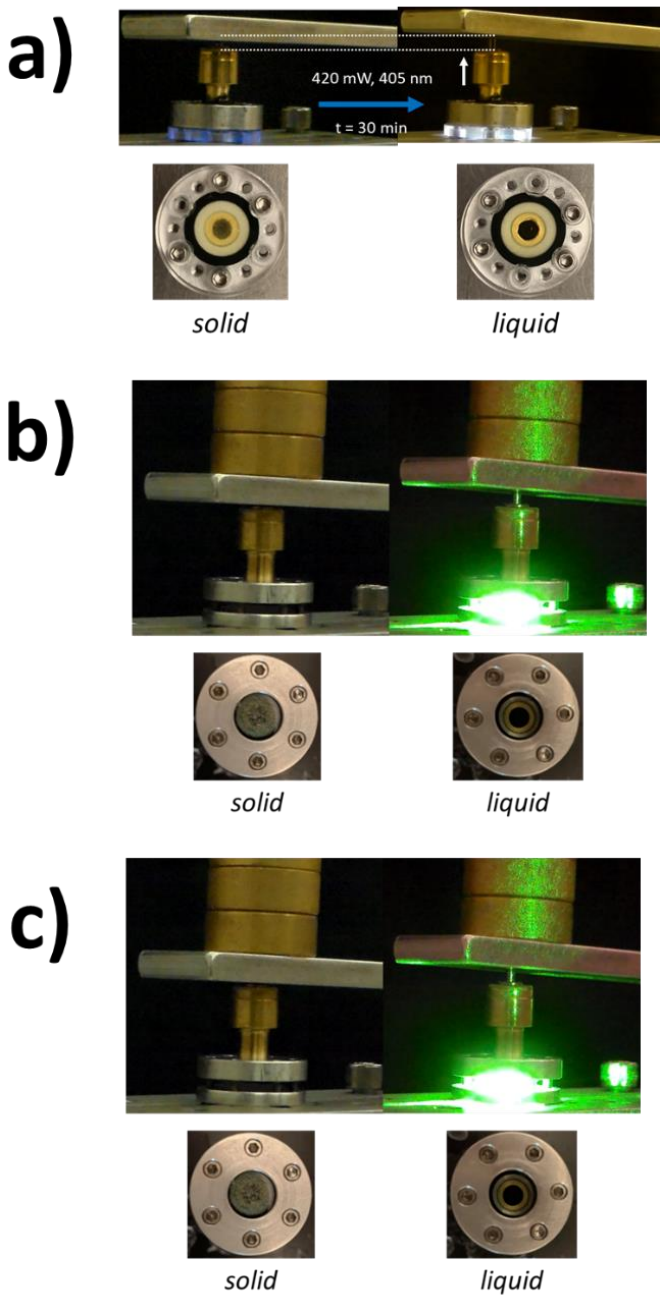

Figure 4.4 a) 3.8 mM AZOB filled actuator is shown lifting the Al lever. Irradiation wavelength used was 405 nm at 420 mW. b) 14.3 mM GAZ filled actuator is shown lifting the Al lever with an additional 400 g. Irradiation wavelength used was 532 nm at 2 W. c) 81.5 mM TEMPO filled actuator is shown in the "off" and "on" state, without any loading. Irradiation wavelength used was 532 nm at 2 W.

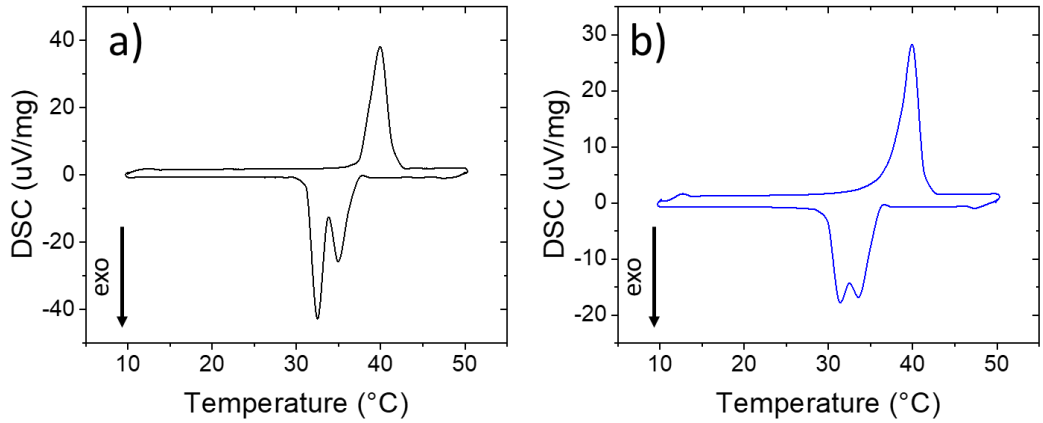

Figure 4.5 Differential scanning calorimetry curves of a) pure eicosane and b) a 14.3 mM GAZ/eicosane mixture.

A single endothermic peak is seen during the heating stage, and the onset melting temperature (T_m) for eicosane, and the GAZ doped sample was found to be 37.4±0.3 °C and 36.2±1.2 °C, respectively which indicates that the doping of small molecules at the millimolar regime does not change the melting temperature to within the error of the measurement. The two exothermic peaks seen during the cooling cycle correspond to transitions from the liquid→rotating phase and rotating phase→crystalline phase.[39] Interestingly, GAZ did affect the resolidification behavior, shifting both steps lower in temperature by 1.4 °C and 1.1 °C, respectively. This shift can be rationalized in terms of a colligative property in which the GAZ molecules inhibit alkane crystallization.[40] Overall, these high concentrations of GAZ have only a small effect on the phase change properties of eicosane.

Exposure of a solid GAZ/eicosane mixture on a glass slide to intense 532 nm laser light could induce melting within 1 minute. In order to assess whether this light-induced

melting could be harnessed to do useful actuation, we modified a commercial thermal wax motor so the interior could be illuminated by laser light. A schematic of the modified wax motor is shown in **Figure 4.6a**. Expansion of the wax after melting squeezes a rubber boot that in turn pushes up a metal rod (**Figure 4.6b**). This is a simple piston-type of wax motor commonly used to open valves in cooling systems.

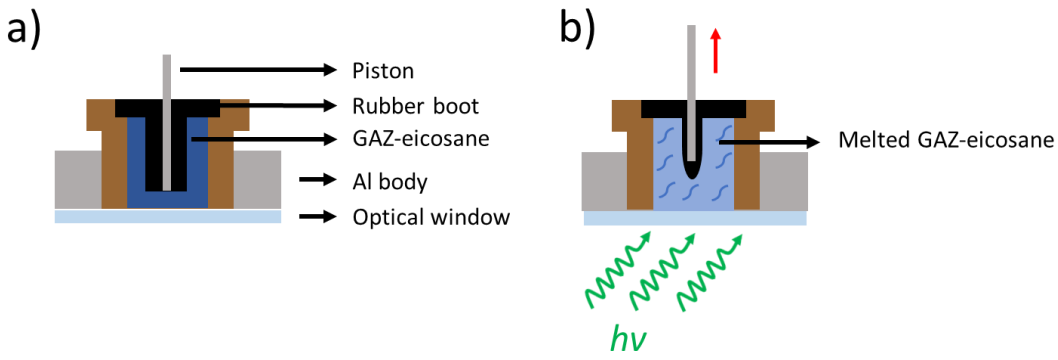

Figure 4.6 a) Cross sectional schematic of the modified wax motor assembly in the "off" state before light is applied. b) During the "on" state, the wax is melted with incident 532 nm laser light and the molten wax compresses the rubber boot, which vertically displaces the piston.

To demonstrate the performance of the GAZ/eicosane mixture, we mounted the actuator so it could push up against a weighted lever. The force and work output can be calculated from the vertical displacement of the lever, as detailed in (**Figure 4.7**). Images of the actuator before irradiation (retracted) and after irradiation (extended) are shown in **Figure 4.8**.

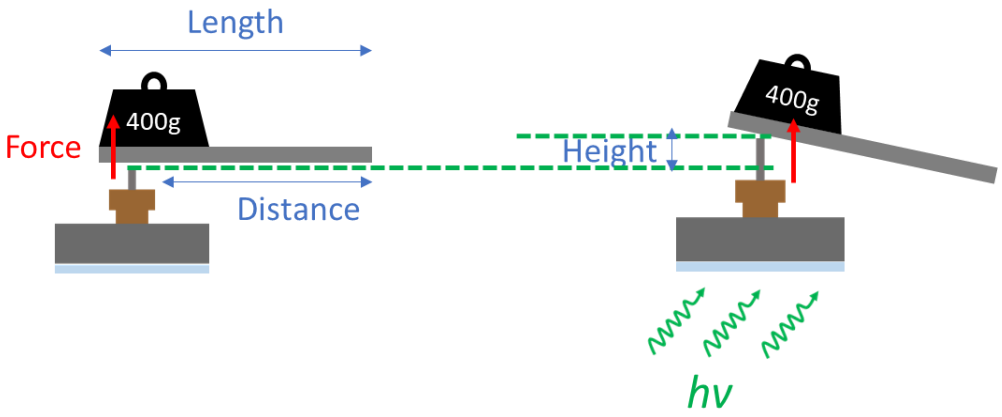

Figure 4.7 A simplified diagram of the piston pushing against the Al lever.

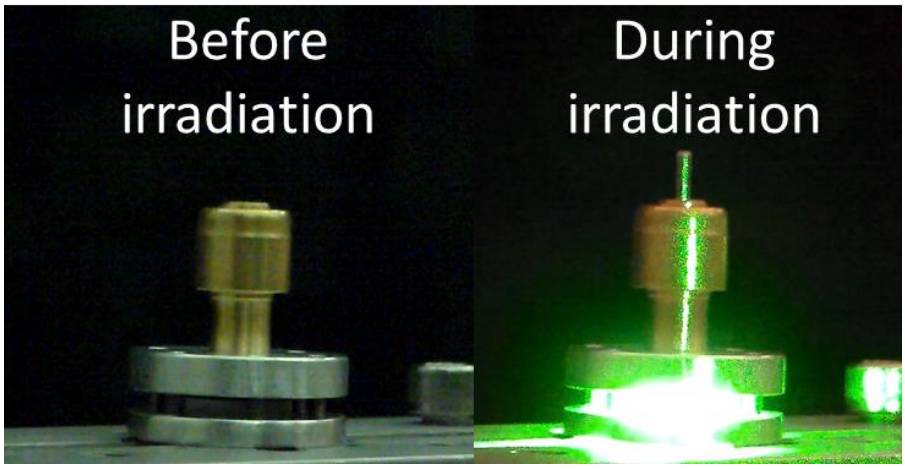

Figure 4.8 Still images of the GAZ/eicosane filled wax motor in the "off" (before light, piston retracted) and "on" (532 nm laser incident, piston extended) state.

The maximum actuator displacement varied by up to 30% from device to device due to variations in filling and the condition of the rubber boot, which degraded after many uses due to laser damage. Thus, data from different devices had slightly different maximum extension values, as seen in the data below. We found that a small illumination spot with high intensity led to the same behavior as a large illumination spot with lower

intensity as long as the powers were equal and both beam spots were contained entirely within the wax. The fact that the melting depends only on the total laser power suggests that thermal transport within the wax rapidly spreads the heat outside the illuminated spot. For this reason, laser conditions are reported in units of power (W) rather than intensity (W cm^{-2}).

The time-dependent extension and retraction for an actuator with a load (4.3 N) are shown in **Figure 4.9a**. After the laser is turned on, there is an induction period while the wax heats up, then an extension as it melts which is maintained as long as the laser is on. After the laser is turned off, the piston returns to its original position on a timescale of minutes. In **Figure 4.9b** we show the dynamics of the initial extension for two different laser powers without any loading. Once the laser was turned on, the displacement occurred in two steps. First, there was a rapid initial extension of 1-2 mm that occurred within seconds, followed by a slower extension that took place over a timescale of minutes. Increasing the laser power could compress these dynamics into a shorter time window, but the general form remained the same. Note that at the higher laser power, the initial extension (~1 mm) appears instantaneous on this graph. We interpret the extension behavior in terms of a two-step melting process. First, there is an initial melting and expansion of the wax adjacent to the transparent window that directly absorbs the laser light, leading to a small initial extension. After this initial melting, heat diffusion through

the wax and metal casing eventually causes the rest of the wax to melt, resulting in full extension of the piston.

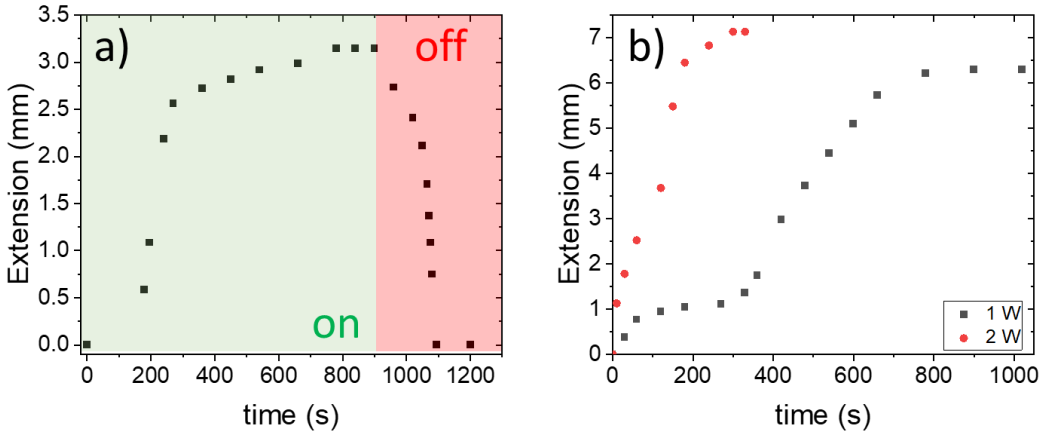

Figure 4.9 a) Time-dependent extension of a loaded (400 g) wax actuator after the laser (2 W) is turned on (green region) and after the laser is turned off (red region). The actuator takes about 15 minutes to reach maximum extension, then returns to its initial position within 5-minutes. b) Time-dependent extension (no load) for two different laser powers: 1 W (black) and 2 W (red). The maximum extension is reached more quickly for higher laser powers and less loading.

It is worth mentioning that an actuator filled only with eicosane and no GAZ would eventually extend after prolonged laser exposure due to residual absorption by the metal and rubber boot. This extension was observed on much longer timescales (**Figure 4.10**) and only at the highest laser power (2 W). At the lowest power where actuation was still observed with the GAZ doped eicosane (0.7 W), no extension at all was observed in the control.

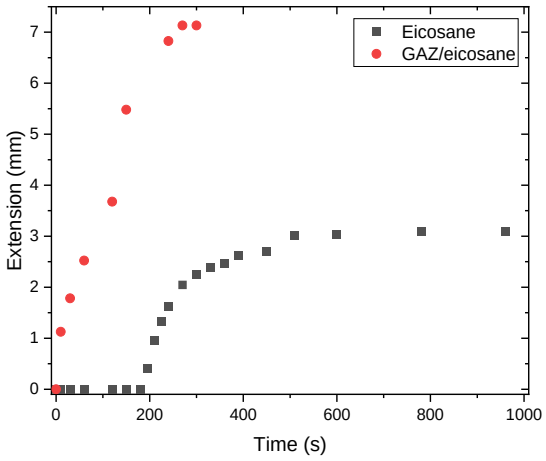

Figure 4.10 Time-dependent extension of the control actuator (filled with pure eicosane, no GAZ) without any load (black squares). 2 W was used and the actuator takes ~3 minutes to begin melting and 13 minutes to reach its full extension. For comparison, the red circles show the extension for the actuator with the GAZ/eicosane mixture, which occurs within 5 seconds after the light is turned on.

After the laser is turned off, the wax slowly cools and resolidifies, leading to a retraction of the piston over the course of 5 minutes. The rate of recovery to the original position did not depend on the laser power seen by the actuator, as expected for a purely thermal process. The slow recovery time is expected since resolidification is governed by both heat loss and by nucleation in the melt. Eicosane has the tendency to supercool, as evidenced by the DSC curves in **Figure 4.5**, so the actuator must cool below T_m before it returns to its original position. A complete description of the time-dependent extension and retraction of the piston would require detailed modeling of the thermal transport within the device[20, 41, 42], which is beyond the scope of this chapter.

A plot of the maximum piston extension versus laser power for a typical device is given in **Figure 4.11a**. The power dependence can be understood qualitatively in terms of a competition between laser input and thermal loss.

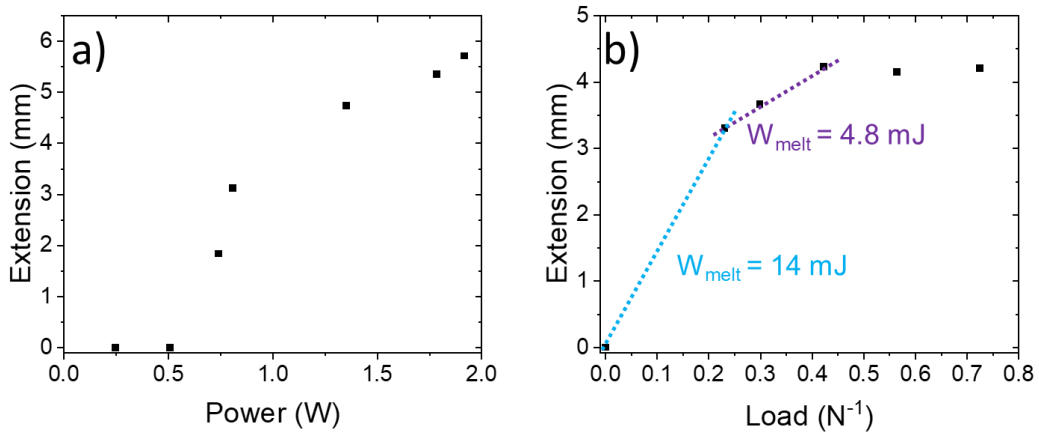

Figure 4.11 a) Plot of piston extension versus 532 nm laser power. At lower powers (≤ 0.5 W) the laser is unable to melt the wax, hence no extension is observed. b) For loads ≤ 200 g, the wax actuator always reached maximum extension, however a linear trend (purple) was observed with heavier loads. The trend in blue is extrapolated assuming that as $1/F_{load} \rightarrow 0$ then extension $d \rightarrow 0$, giving a slightly larger slope W_{melt}.

For a perfectly insulated actuator, even a low power laser would eventually deposit enough energy to melt all of the wax and achieve full extension. But heat loss to the surroundings, both air and the contact points of the metal casing to the support structure, competes with the laser heating, so lower laser powers cannot build up sufficient heat to attain T_m. This leads to a threshold (~0.5 W) below which no extension can be observed. Once this threshold is reached, there is partial melting, and the extension increases roughly linearly with laser power. At the highest powers, we achieve full melting, and the extension saturates at its maximum value. For an oven-heated actuator, where the motor and its

surroundings are held at the same temperature, the competing heat loss is not a factor and full extension is always attained. The use of an actuator with a larger wax volume should lead to larger extensions but would also experience more heat dissipation and thus require larger laser powers. For example, the threshold for extension would be greater than the 0.5 W needed for the actuator structure used in our experiments.

The maximum extension also depends on the opposing force. **Figure 4.11b** shows an extension versus load curve for an actuator exposed to 2 W laser irradiation that generates full extension without a load. As the load on the lever is increased, the piston can no longer reach its full extension. For example, a load of 0.400 kg resulted in an opposing force of 4.3 N. Application of a 2 W laser beam for 780 seconds resulted in a 3.3 mm displacement, or 0.0142 J of work. The overall efficiency of the actuation, defined as the work output divided by the laser energy input, is calculated to be 0.0142 J/1560 J = 9.1×10^{-6}. In this regime, if we assume that the eicosane melting generates a constant amount of work W_{melt}, then the extension d is related to W_{melt} by

$$W_{melt}=F_{load}\times d \qquad (1)$$

where F_{load} is the force due to the weighted lever. A plot of d versus $1/F_{load}$ should be linear with a slope of W_{melt}. We were unable to balance sufficient weight on the lever to completely prevent any extension, so we could not approach the $1/F_{load} = 0$ limit, where we would expect $d\rightarrow 0$. The data in **Figure 4.11b** can be analyzed in terms of two different regimes. In the low F_{load} regime (large $1/F_{load}$ values), we extract a slope W_{melt} = 4.8 mJ. If we force the line from the last point to go through the origin, we obtain a slightly higher slope of 14 mJ for the high F_{load} regime. The work density can be calculated in two different

ways. If we consider the total volume of the actuator (5.6 cm^3), then from the fits in **Figure 4.11b**, we can extract an energy density in the range 8.6×10^{-4}-2.5×10^{-3} J cm^{-3}. This range is well below reported values of soft actuators that do not require containment systems, such as structured elastomers[43] and polymer nanocomposites[21, 44, 45] that can reach up to 0.5 J cm^{-3}. Alternatively, if we only consider the volume of the active material (i.e., eicosane), then we can extract a work density in the range 0.048-0.14 J cm^{-3}. These values are still below the limit of thermal alkane PCM systems, which can reach up to 9 J cm^{-3}[46].

Finally, to assess the chemical stability of the GAZ/eicosane mixture, we subjected it to repeated melt-solidification cycles using both thermal (oven) and laser heat sources. In both cases, the GAZ absorption showed no loss of intensity after 35 cycles (**Figure 4.12a** and **Figure 4.12b**). The chemical stability of the GAZ/eicosane mixture leads to stable mechanical extension, as shown in **Figure 4.12c** for both laser and oven heating. The laser heated actuator extension was 2.0 mm with a standard deviation of ±0.2 mm, or about 10%. Note that the laser power was lowered so that only partial melting (and less than full extension) was achieved. This avoided full melting, which would lead to an artificially stable data since the extension would always saturate at its maximum value, as is the case for the oven-heated actuator. There was no sign of diminished response after 10 cycles for either the oven or laser heated actuator. This result shows that controlling the laser power provides a reproducible way to control the actuator extension.

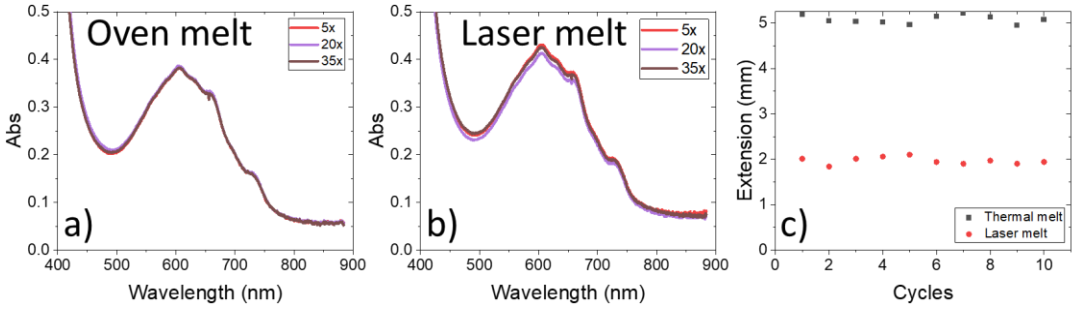

Figure 4.12 Absorption spectra of the liquid GAZ/eicosane mixture demonstrate the chemical stability from both a) thermal and b) optical melting. c) The GAZ/eicosane filled wax actuator was cycled up to 10 times to demonstrate that the actuator experiences no fatigue regardless of method of melting. The laser power was 1.0 W.

Since both resistive and laser heating can drive wax melting and power a linear actuator, it is worth considering the potential advantages of the laser heating approach in the context of wax motors. As mentioned in **section 4.2**, light has some advantages as a non-contact power source. But a second advantage is that light can bypass the actuator casing and directly heat the encapsulated wax through a transparent window. During laser irradiation, we noted that the initial actuator extension occurred while the casing was still cool to the touch. At longer times, after the body of the actuator had warmed up, the rest of the wax melted, and full extension was achieved. For resistive heating, on the other hand, the heating element is attached to the outside of the actuator casing, and the entire device must be heated above T_m before actuation can begin. The ability to selectively heat the PCM without directly heating the device casing or its surroundings may prove useful in some applications. If we consider our results in the context of other photothermal actuators, the current results are novel because they demonstrate that a stable photothermal PCM can be utilized in a well-established actuator architecture that generates a linear

expansion. Many photothermal actuators rely on shape changes, often bending due to asymmetric thermal expansion[10-14, 16, 22, 24, 35], that are difficult to incorporate into traditional actuator geometries. Actuators that rely on photothermal contraction of polymer composites can do work by pulling an object[6-9, 21], similar to muscle, but they cannot push outward due to their low elastic modulus.

Although the proof-of-principle experiments in this chapter demonstrate the concept, there is considerable room for improvement of the photothermal wax motor, including: 1) Improved thermal isolation of the wax from the actuator body, which would result in faster extension and less energy wasted in heating the surroundings. However, the contraction of the actuator after removal of light would slow down, since it requires heat loss. 2) Modifying the actuator structure to decrease its volume and improve coupling of the PCM to the mechanical output. In our devices, the compressibility of the rubber boot is probably one factor that limits the work output. There are several alternative geometries for wax motors in the literature.[47, 48] 3) Choosing a different PCM host material, possibly by drawing on the extensive work already done in the field of energy storage[49], to increase the work output from the melting.

Finally, the choice of photothermal agent requires special consideration. GAZ has a relatively weak absorption at 532 nm, so the use of a more highly absorbing chromophore would improve energy transfer from the light to the material, with less 532 nm light lost to scattering. For the same concentration, a more highly absorbing chromophore would also limit light penetration, but at the intensities used here, rapid thermal diffusion seems to be able to distribute heat from the localized absorbing region to the rest of the wax on a

reasonable timescale. GAZ has the advantage of high solubility in eicosane and has the possibility to tune its absorption by adding different substituents.[50, 51] But it is certainly worth looking for other chromophores that combine stronger absorption with high IC rates.

4.4 Conclusion

Using a blend of small molecule absorbers in an alkane PCM, we have shown that a practical light-powered wax motor can be realized. The temporal response, work and force output, and cyclability of this motor have been characterized and the path forward to optimize these figures-of-merit seems straightforward. The availability of small, highly soluble aromatic molecules with low-energy absorption features and rapid IC suggests that photothermal solid→liquid phase transitions could provide a general approach for making light-powered actuators.

4.5 Experimental

4.5.1 Sample preparation:

n-Eicosane, TEMPO, and azobenzene (AZOB) were purchased from Sigma-Aldrich. Guaiazulene (GAZ) was purchased from TCI Chemicals. All chemicals were used without further purification. GAZ-eicosane mixtures were prepared by melting the eicosane (3.8773 g, 4.92 mL) and mixing in solid GAZ particles (13.9 mg, 7×10^{-5} mol). The molten wax mixture was allowed to equilibrate for at least 1 hour before cooling. AZOB and TEMPO wax mixtures were prepared in the same fashion.

5-nm dodecanethiol functionalized gold nanoparticles (AuNPs) were purchased from Nanoprobes and used without further modification. Eicosane was melted in an oven and the AuNPs were placed in the molten wax (1.4% w/w) and mixed until visually

homogenous. Films of the AuNP/eicosane mixture were deposited on glass slides and a 532 nm laser diode was used to optically melt the films. The films were also subjected to heat-cool cycles in an oven to test for chemical stability. It was found that after 3 cycles, there was visible separation between eicosane and AuNPs at the edges of the film.

4.5.2 Spectroscopic methods:

A 1-mm path length quartz cell was used for the spectroscopic measurements. An Agilent Cary-5000 was used to measure the steady state UV-Vis absorption of solid GAZ-eicosane mixtures. For the cycling experiments, in order to avoid a variable scattering background from the solid, the GAZ absorption was measured in the molten state. In order to measure the melt quickly before resolidification, an Ocean Optics USB4000 was used. OceanView software was used to operate the spectrometer with the wavelength window of 400-800 nm. A heat gun and a 532 nm laser (2 W output) was used to thermally and optically melt the mixture, respectively.

4.5.3 Differential scanning calorimetry:

Melting points of the GAZ-eicosane mixture and pure n-eicosane were measured using a Netzsch 214 Polyma differential scanning calorimeter. A temperature range of 10 °C-50 °C was used with a 5 °C/min heating rate, 1-min holding, and 5 °C/min cooling rate. The samples were heated and cooled for three cycles and the onset melting temperatures were collected.

4.5.4 Device fabrication & work output measurement:

A commercially available wax motor (Honda 16620-Z0Y-M41 Thermostat) was modified to incorporate the GAZ-eicosane mixture and allow optical access. Briefly, the

actuator consists of a rubber boot and a metal piston. The actuator was pressed into an aluminum disk which allowed for an optical window to be attached. The actuator was then filled with the molten wax mixture and allowed to solidify. Excess wax was scraped away, and the optical window was clamped with an O-ring to prevent leakage. A lever apparatus was built to measure the displacement and work output of the actuator, as described in **Figure 4.13**. Digital calipers were used to measure the displacement of the piston to within 0.02 mm. A continuous wave 532 nm laser was used as the irradiation source for the photothermal melting.

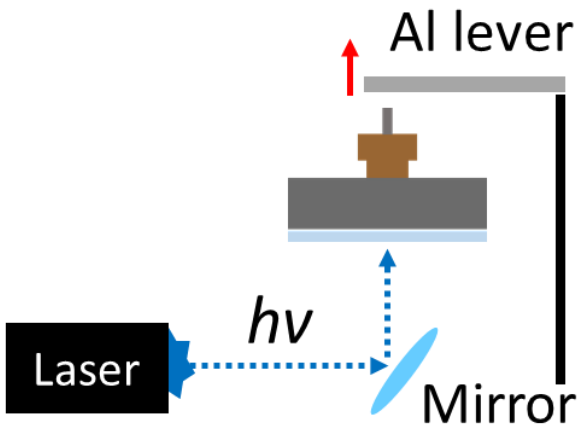

Figure 4.13 Schematic of the apparatus used to measure the work output of the wax actuator. Additional weights are placed on top of the Al lever to increase the loading.

4.6 References

(1) White, T. J. Photomechanical Materials, Composites, and Systems. 1 ed.; Wiley: Hoboken, New Jersey, 2017.

(2) Kim, T.; Zhu, L.; Al-Kaysi, R. O.; Bardeen, C. J. Organic photomechanical materials. *ChemPhysChem* **2014**, *15*, 400-414.

(3) Ikeda, T.; Mamiya, J.-i.; Yu, Y. Photomechanics of Liquid-Crystalline Elastomers and Other Polymers. *Angew. Chem. Intl. Ed.* **2007**, *46*, 506–528. DOI: 10.1002/anie.200602372.

(4) Naumov, P.; Chizhik, S.; Panda, M. K.; Nath, N. K.; Boldyreva, E. Mechanically Responsive Molecular Crystals. *Chem. Rev.* **2015**, *115*, 12440-12490.

(5) Sarkisov, S. S.; Curley, M. J.; Fields, A.; II, S. S. S.; Adamovsky, G. Photomechanical effect in films of polyvinylidene fluoride. *Appl. Phys. Lett.* **2004**, *85*, 2447-2449. DOI: 10.1063/1.1802390.

(6) Ahir, S. V.; Terentjev, E. M. Photomechanical actuation in polymer–nanotube composites. *Nat. Mater.* **2005**, *4*, 491-495. DOI: 10.1038/nmat1391.

(7) Lu, S.; Panchapakesan, B. Photomechanical responses of carbon nanotube/polymer actuators. *Nanotechnology* **2007**, *18*, 305502. DOI: 10.1088/0957-4484/18/30/305502.

(8) Loomis, J.; Fan, X.; Khosravi, F.; Xu, P.; Fletcher, M.; Cohn, R. W.; Panchapakesan1, B. Graphene/elastomer composite-based photo-thermal nanopositioners. *Sci. Rep.* **2013**, *3*, 1900. DOI: 10.1038/srep01900.

(9) Shen, X.; Viney, C.; Johnson, E. R.; Wang, C.; Lu, J. Q. Large negative thermal expansion of a polymer driven by a submolecular conformational change. *Nat. Chem.* **2013**, *5*, 1035-1041. DOI: 10.1038/nchem.1780.

(10) Hu, Y.; Wu, G.; Lan, T.; Zhao, J.; Liu, Y.; Chen, W. A Graphene-Based Bimorph Structure for Design of High Performance Photoactuators. *Adv. Mater.* **2015**, *27*, 7867–7873. DOI: 10.1002/adma.201502777.

(11) Liu, K.; Cheng, C.; Cheng, Z.; Wang, K.; Ramesh, R.; Wu, J. Giant-Amplitude, High-Work Density Microactuators with Phase Transition Activated Nanolayer Bimorphs. *Nano Lett.* **2012**, *12*, 6302−6308. DOI: 10.1021/nl303405g.

(12) He, Y.; Liang, H.; Chen, M.; Jiang, L.; Zhang, Z.; Heng, X.; Yang, L.; Hao, Y.; Gan, J.; Yang, Z. Optical Fiber Waveguiding Soft Photoactuators Exhibiting Giant

Reversible Shape Change. *Adv. Opt. Mater.* **2021**, 2101132. DOI: 10.1002/adom.202101132.

(13) Kuenstler, A. S.; Chen, Y.; Bui, P.; Kim, H.; DeSimone, A.; Jin, L.; Hayward, R. C. Blueprinting Photothermal Shape-Morphing of Liquid Crystal Elastomers. *Adv. Mater.* **2020**, *32*, 2000609. DOI: 10.1002/adma.202000609.

(14) Chen, J.; Feng, J.; Yang, F.; Aleisa, R.; Zhang, Q.; Yin, Y. Space-Confined Seeded Growth of Cu Nanorods with Strong Surface Plasmon Resonance for Photothermal Actuation. *Angew. Chem. Intl. Ed.* **2019**, *58*, 9275 – 9281. DOI: 10.1002/anie.201904828.

(15) Wang, T.; Torres, D.; Fernández, F. E.; Wang, C.; Sepúlveda, N. Maximizing the performance of photothermal actuators by combining smart materials with supplementary advantages. *Sci. Adv.* **2017**, *3*, e1602697. DOI: 10.1126/sciadv.1602697.

(16) Lee, J.; Sroda, M. M.; Kwon, Y.; El-Arid, S.; Seshadri, S.; Gockowski, L. F.; Hawkes, E. W.; Megan T. Valentine; Alaniz, J. R. d. Tunable Photothermal Actuation Enabled by Photoswitching of Donor−Acceptor Stenhouse Adducts. *ACS Appl. Mater. Interfaces* **2020**, *12*, 54075–54082. DOI: 10.1021/acsami.0c15116.

(17) Ma, H.; Xiao, X.; Zhang, X.; Liu, K. Recent advances for phase-transition materials for actuators. *J. Appl. Phys.* **2020**, *128*, 101101. DOI: 10.1063/5.0020596.

(18) Wilhelm, E.; Richtera, C.; Rapp, B. E. Phase change materials in microactuators: Basics, applications and perspectives. *Sensors Actuators A* **2018**, *271*, 303–347. DOI: 10.1016/j.sna.2018.01.043.

(19) Templen, P. R. Coefficient of Volume Expansion for Petroleum Waxes and Pure n-Paraffins. *Ind. Eng. Chem.* **1956**, *48*, 154-161. DOI: 10.1021/ie50553a043.

(20) Ogden, S.; Klintberg, L.; Thornell, G.; Hjort, K.; Boden, R. Review on miniaturized paraffin phase change actuators, valves, and pumps. *Microfluid Nanofluid* **2014**, *17*, 53–71. DOI: 10.1007/s10404-013-1289-3.

(21) Lima, M. D.; Li, N.; Andrade, M. J. d.; Fang, S.; Oh, J.; Spinks, G. M.; Kozlov, M. E.; Haines, C. S.; Suh, D.; Foroughi, J.; et al. Electrically, Chemically, and Photonically Powered Torsional and Tensile Actuation of Hybrid Carbon Nanotube Yarn Muscles. *Science* **2012**, *338*, 928-932. DOI: 10.1126/science.1226762.

(22) Deng, J.; Li, J.; Chen, P.; Fang, X.; Sun, X.; Jiang, Y.; Weng, W.; Bingjie Wang; Peng, H. Tunable Photothermal Actuators Based on a Pre-programmed Aligned Nanostructure. *J. Am. Chem. Soc.* **2016**, *138*, 225–230. DOI: 10.1021/jacs.5b10131.

(23) Han, B.; Zhang, Y.-L.; Chen, Q.-D.; Sun, H.-B. Carbon-Based Photothermal Actuators. *Adv. Funct. Mater.* **2018**, 1802235. DOI: 10.1002/adfm.201802235.

(24) Xiao, X.; Ma, H.; Zhang, X. Flexible Photodriven Actuator Based on Gradient−Paraffin-Wax-Filled $Ti_3C_2T_x$ MXene Film for Bionic Robots. *ACS Nano* **2021**, *15*, 12826−12835. DOI: 10.1021/acsnano.1c03950; .

(25) Park, J.-M.; Cho, Y.-K.; Lee, B.-S.; Lee, J.-G.; Ko, C. Multifunctional microvalves control by optical illumination on nanoheaters and its application in centrifugal microfluidic devices. *Lab Chip* **2007**, *7*, 557–564. DOI: 10.1039/b616112j.

(26) Hou, S.; Wang, M.; Guo, S.; Su, M. Photothermally Driven Refreshable Microactuators Based on Graphene Oxide Doped Paraffin. *ACS Appl. Mater. Interfaces* **2017**, *9*, 26476−26482. DOI: 10.1021/acsami.7b08728.

(27) Abi-Samra, K.; Hanson, R.; Madou, M.; Gorkin, R. A. Infrared controlled waxes for liquid handling and storage on a CD-microfluidic platform. *Lab Chip* **2011**, *11*, 723–726. DOI: 10.1039/c0lc00160k.

(28) Jung, J. H.; Han, C.; Lee, S. A.; Kima, J.; Yanga, C. Microfluidic-integrated laser-controlled microactuators with on-chip microscopy imaging functionality. *Lab Chip* **2014**, *14*, 3781–3789. DOI: 10.1039/c4lc00790e.

(29) Saydam, V.; Duan, X. Dispersing different nanoparticles in paraffin wax as enhanced phase change materials: A study on the stability issue. *J. Therm. Anal. Calorim.* **2019**, *135*, 1135-1144. DOI: 10.1007/s10973-018-7484-4.

(30) Zimerman, O. E.; Weiss, R. G. Pyrene Photochemistry in Solid n-Alkane Matrices: Comparisons with Liquid-Phase Reactions. *J. Phys. Chem. A* **1999**, *103*, 9794-9804. DOI: 10.1021/jp992339h.

(31) Thorne, J. B.; Bobbitt, D. R. Comparison of Beer's Law and Thermal Lens Techniques for Absorption Measurements Under Conditions of High Scattering Backgrounds. *Appl. Spect.* **1993**, *47*, 360-365. DOI: 10.1366/0003702934066785.

(32) Fujino, T.; Tahara, T. Picosecond Time-Resolved Raman Study of trans-Azobenzene. *J. Phys. Chem. A* **2000**, *104*, 4203–4210. DOI: 10.1021/jp992757m.

(33) Stuart, C. M.; Frontiera, R. R.; Mathies, R. A. Excited-State Structure and Dynamics of cis- and trans-Azobenzene from Resonance Raman Intensity Analysis. *J. Phys. Chem. A* **2007**, *111*, 12072–12080. DOI: 10.1021/jp0751460.

(34) Yu, J. K.; Bannwarth, C.; Liang, R.; Hohenstein, E. G.; Martínez, T. J. Nonadiabatic Dynamics Simulation of the Wavelength-Dependent Photochemistry of

Azobenzene Excited to the nπ* and ππ* Excited States. *J. Am. Chem. Soc.* **2020**, *142*, 20680–20690. DOI: 10.1021/jacs.0c09056.

(35) Cunha, M. P. d.; Thoor, E. A. J. v.; Debije, M. G.; Broer, D. J.; Schenning, A. P. H. J. Unravelling the photothermal and photomechanical contributions to actuation of azobenzene-doped liquid crystal polymers in air and water. *J. Mater. Chem. C* **2019**, *7*, 13502-13509. DOI: 10.1039/C9TC04440J.

(36) Lalevee, J.; Allonas, X.; Jacques, P. Electronic distribution and solvatochromism investigation of a model radical (2,2,6,6-tetramethylpiperidine N-oxyl: tempo) through TD-DFT calculations including PCM solvation. *J. Molec. Struct. THEOCHEM* **2006**, *767*, 143–147. DOI: 10.1016/j.theochem.2006.05.054.

(37) J.Michl; E.W.Thulstrup. Why is azulene blue and anthracene white? a simple mo picture. *Tetrahedron* **1976**, *32*, 205-209. DOI: 10.1016/0040-4020(76)87002-0.

(38) Wagner, B. D.; Szymanski, M.; Steer, R. P. Subpicosecond pump–probe measurements of the electronic relaxation rates of the S_1 states of azulene and related compounds in polar and nonpolar solvents. *J. Chem. Phys.* **1993**, *98*, 301-307. DOI: 10.1063/1.464675.

(39) Taggart, A. M.; Voogt, F.; Clydesdale, G.; Roberts, K. J. An Examination of the Nucleation Kinetics of n-Alkanes in the Homologous Series $C_{13}H_{28}$ to $C_{32}H_{66}$, and Their Relationship to Structural Type, Associated with Crystallization from Stagnant Melts. *Langmuir* **1996**, *12*, 5722-5728. DOI: 10.1021/la9600816.

(40) Ball, R.; Jones, J. C. Thermodynamics of the Deposition of Complex Waxes and Asphaltenes in Crude Oil. *Open Thermodyn. J.* **2009**, *3*, 34-37. DOI: 10.2174/1874396X00903010034.

(41) Lee, J. S.; Lucyszyn, S. Thermal analysis for bulk-micromachined electrothermal hydraulic microactuators using a phase change material. *Sensors Actuators A* **2007**, *135*, 731–739. DOI: 10.1016/j.sna.2006.07.033.

(42) Mann, A.; Bürgel, C. M.; Groche, P. A Modeling Strategy for Predicting the Properties of Paraffin Wax Actuators. *Actuators* **2018**, *7*, 81. DOI: 10.3390/act7040081.

(43) Ware, T. H.; McConney, M. E.; Wie, J. J.; Tondiglia, V. P.; White, T. J. Voxelated liquid crystal elastomers. *Science* **2015**, *347*, 982-984. DOI: 10.1126/science.1261019.

(44) Liang, J.; Xu, Y.; Huang, Y.; Zhang, L.; Wang, Y.; Ma, Y.; Li, F.; Guo, T.; Chen, Y. Infrared-Triggered Actuators from Graphene-Based Nanocomposites. *J. Phys. Chem. C* **2009**, *113*, 9921–9927. DOI: 10.1021/jp901284d.

(45) Feng, Y.; Qin, M.; Guo, H.; Yoshino, K.; Feng, W. Infrared-Actuated Recovery of Polyurethane Filled by Reduced Graphene Oxide/Carbon Nanotube Hybrids with High Energy Density. *ACS Appl. Mater. Interfaces* **2013**, *5*, 10882−10888. DOI: 10.1021/am403071k.

(46) Srinivasan, P.; Spearing, S. M. Material Selection for Optimal Design of Thermally Actuated Pneumatic and Phase Change Microactuators. *J. Microelectromech. Syst.* **2009**, *18*, 239-249. DOI: 10.1109/JMEMS.2009.2013385.

(47) Carlen, E. T.; Mastrangelo, C. H. Electrothermally Activated Paraffin Microactuators. *J. Microelectromech. Syst.* **2002**, *11*, 165-174. DOI: 10.1109/JMEMS.2002.1007394.

(48) Mann, A.; Germann, T.; Ruiter, M.; Groche, P. The challenge of upscaling paraffin wax actuators. *Mater. Design* **2020**, *190*, 108580. DOI: 10.1016/j.matdes.2020.108580.

(49) Yuan, K.; Shi, J.; Aftab, W.; Qin, M.; Usman, A.; Zhou, F.; Lv, Y.; Gao, S.; Zou, R. Engineering the Thermal Conductivity of Functional Phase-Change Materials for Heat Energy Conversion, Storage, and Utilization. *Adv. Funct. Mater.* **2020**, *30*, 1904228. DOI: 10.1002/adfm.201904228.

(50) Liu, R. S. H.; Muthyala, R. S.; Wang, X.-s.; Asato, A. E.; Wang, P.; Ye, C. Correlation of Substituent Effects and Energy Levels of the Two Lowest Excited States of the Azulenic Chromophore. *Org. Lett.* **2000**, *2*, 269-271. DOI: 10.1021/ol990324w.

(51) Zhang, X.-H.; Li, C.; Wang, W.-B.; Cheng, X.-X.; Wang, X.-S.; Zhang, B.-W. Photophysical, electrochemical, and photoelectrochemical properties of new azulene-based dye molecules. *J. Mater. Chem.* **2007**, *17*, 642-649. DOI: 10.1039/B613703B.

5. Performance of a Photothermal Actuator Based on Small Molecule Absorbers Dissolved in Eicosane

5.1 Preface

We continue the discussion of photothermally induced solid→liquid phase change materials. In this chapter, the same guaiazulene-eicosane composite from Chapter 4 is used in a custom actuator. The actuator differs from the version discussed in Chapter 4 in that the rubber boot is replaced with a transparent silicone membrane. It was found that the boot was absorbing the incident laser light and thus, after several cycles there were noticeable performance drops. The non-absorbing silicone membrane in this new actuator remedies this problem by acting as the flexible membrane that pushes up against a piston while maintaining structural integrity. A variety of heating methods are compared with photothermal heating, ranging from direct laser heating of the wax mixture to laser heating the metal body of the actuator directly, and finally to resistive heating. It was reported that using light to directly heat the wax is the most effective and efficient way to induce a photothermal phase transition when compared to the alternative methods. The work output, cyclability, and stability are also discussed here.

5.2 Introduction

Light provides a low-loss way to transmit energy without the need for physical contacts. Once it has arrived at its destination, however, light must be converted to electrical energy using photovoltaic materials, or to mechanical energy using photomechanical materials.[1–8] In the latter case, mechanical motion can arise through a variety of mechanisms, including photochemical reactions and photothermal expansion.[9–

[15] The effect of light-induced heating can be magnified if it induces a phase transition that results in a substantial volume change. Photoinduced liquid-to-gas transitions have been used for both actuation and locomotion.[16,17] Photoinduced solid-to-liquid transitions can also generate volume changes that can be harnessed to perform work.[9] For example, photothermal melting of alkane waxes can generate up to a 15% expansion that has been used for actuation in a variety of systems.[18] Photoinduced heating can be accelerated by the use of absorbing dopants, and we recently demonstrated that small molecules dopants are an effective way to enable laser heating of the wax while avoiding phase separation and aggregation.[19]

Previous work has demonstrated the laser induced operation of wax actuators, but there remain some key points that need to be addressed before they can be considered for practical applications. First, we must determine the maximum work output or work density of such a device, and how it compares to theoretical models. Second, we must determine how material parameters like the chemical identity of the absorber and its concentration affect the performance of the actuator. Finally, it is important to establish whether photothermal heating possesses any significant advantages relative to standard methods of resistive heating, besides the obvious advantage of not requiring physical contact between the energy source and the actuator. We hypothesize that the ability for light to deposit heat directly into the working medium (without having to pass through an intermediate material, like a metal casing) should decrease the response time for a given energy input.

In order to test these ideas, we needed to design the simplest possible wax actuator that could also be robust under laser illumination. Previously, we used a commercial wax

motor that was modified to enable light penetration. This version of a wax motor relied on a rubber boot to couple the wax expansion to a movable piston. This geometry did not provide a straightforward way to correlate the wax expansion with the piston displacement. Furthermore, the black rubber boot was susceptible to laser damage, which limited its lifetime. For the work in this chapter, we fabricated an actuator in which the expanding wax deforms a flexible silicone membrane. This design avoids the problem of laser damage and facilitates comparison with theoretical models.[20] We tested the performance of this actuator under a variety of experimental conditions, including resistive versus light-mediated heating, absorber identity and concentration, and filling. Using guaiazulene (GAZ) as an absorbing dopant and eicosane ($C_{20}H_{42}$) as the phase change material (wax), we found that light-mediated melting has clear advantages in terms of response time and thermal loading when compared to external heating by the laser or by a resistive heater. The use of a perylenediimide dye molecule, Lumogen Orange F 240 (LO), as an absorber can also induce melting and actuation, but its lower solubility and high fluorescence quantum yield make it less effective than GAZ. The results of this chapter help define parameters that can be tuned to improve the temporal performance and work output of light-powered actuators and make them competitive with other technologies.

5.3 Experimental

5.3.1 Sample Preparation

n-Eicosane was purchased from Sigma-Aldrich. Guaiazulene (GAZ) was purchased from TCI chemicals. Lumogen Orange F 240 (LO) was purchased from BASF. All chemicals were used without further purification. Small molecule-eicosane mixtures were

prepared by melting eicosane and mixing with GAZ or LO powders. A series of different concentrations including 2, 10, 20, 60, and 100 mM GAZ in eicosane were prepared. Due to the limited solubility of LO in eicosane, the mixtures were placed in a sonicating water bath at 40°C for one hour to ensure that the LO was fully dissolved, as judged by the absence of visible dye particles. The highest concentration of LO-eicosane prepared was 0.23 mM. The molten small molecule-wax mixtures were stirred and placed in an oven (60 °C) for an hour to equilibrate before cooling to room temperature.

5.3.2 Differential scanning calorimetry (DSC)

A Netzsch 214 Polyma differential scanning calorimeter was used to measure the melting points of pure n-eicosane, 60 mM GAZ-eicosane, and 0.23 mM LO-eicosane. A temperature range of 10-50 °C was used with a 5 °C/min heating, 1 min holding, and 5 °C/min cooling rate. The samples were melted and resolidified for three cycles and the onset melting temperatures were collected. Neither the GAZ nor the LO affected the phase change behavior of eicosane, as measured using DSC (**Figure 5.1**).[21]

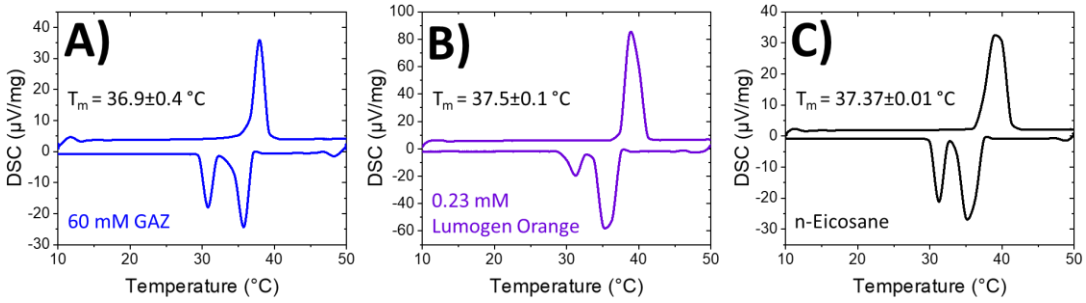

Figure 5.1 DSC curves of **A)** 60 mM GAZ, **B)** 0.23 mM LO, and **C)** pure n-eicosane.

5.3.3 Mechanical Characterization

The actuator consisted of an aluminum cylinder to contain the wax that was capped on both ends. The bottom of the cylinder was capped with a 12.80 mm diameter, 1.25 mm thick borosilicate window (Esco Optics) which transmitted the laser light, while a 0.5-mm thick silicone membrane (The Rubber Company) was the flexible membrane that accommodated the wax expansion at the top portion of the actuator. The glass window and silicone membrane were clamped to the cylinder with butyl rubber O-rings to prevent any leakage.

A 532 nm laser diode with an output power of 2 W was used to optically melt the wax. The apparatus used to measure the work performed by the actuator is shown in **Figure 5.2**. The laser entered the wax cylinder through the bottom window, and the piston displacement was vertical. The resulting motion of the piston was recorded using a video camera and analyzed to extract the time-dependent extension *X(t)*. The cycling was done by laser melting the wax with a 100 g weight that compressed the wax after the laser was turned off. All work output and cycling measurements were done using the 20 mM GAZ/eicosane mixture.

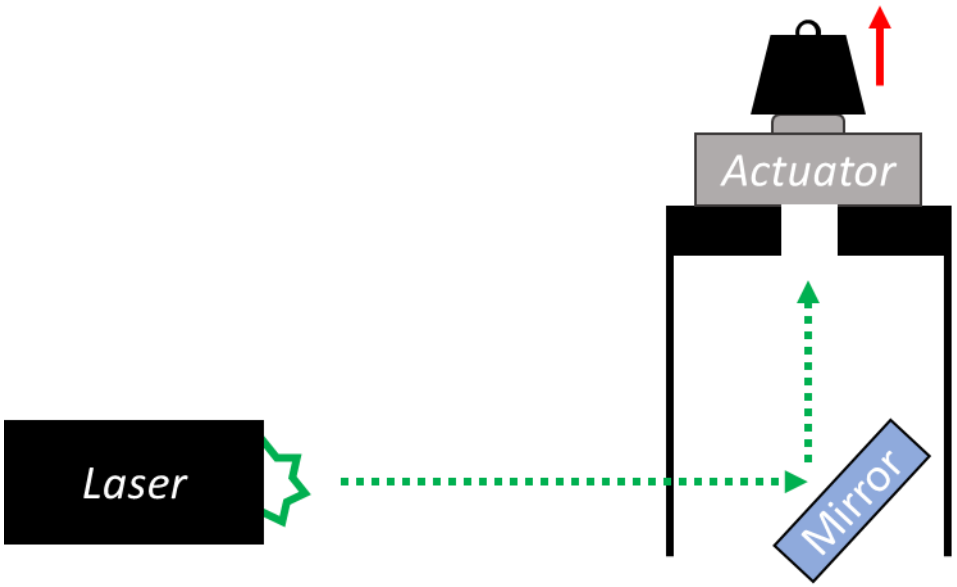

Figure 5.2 Schematic of the apparatus used to hold the actuator during irradiation experiments. The actuator rests on a slotted platform allowing the laser light to enter through the bottom. A mirror sends the laser beam upwards, into the optical window for the actuator. Weights are balanced on top of the piston.

5.3.4 Spectroscopy

An Agilent Cary-60 spectrometer was used to measure the steady state absorption of GAZ- and LO-mixtures in a 1 mm path length quartz cell. A heat gun was used to melt the solid eicosane mixtures in the sample holder of the spectrometer in order to obtain spectra without a high scattering background.

5.4 Results and Discussion

Figure 5.3 shows the molecular structures and absorption spectra of the two absorbers in liquid eicosane, guaiazulene (GAZ) and lumogen orange F 240 (LO). Both absorption

spectra in **Figure 5.3** resemble the monomeric absorption spectra measured in dilute hexanes solution, with no sign of aggregation even at high concentrations.

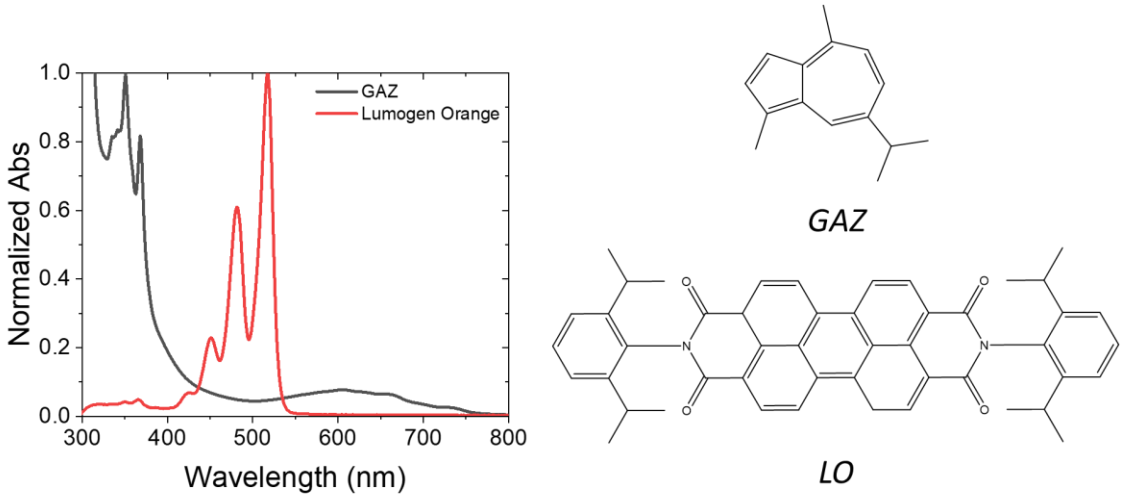

Figure 5.3 Normalized absorbance of guaiazulene (GAZ) and lumogen orange (LO) absorbers in molten eicosane. The chemical structures of GAZ and LO are shown on the right.

GAZ has the advantage that it is highly soluble in eicosane and has a high internal conversion yield, enabling it to convert absorbed photon energy into heat with close to 100% efficiency. The main weakness of GAZ is its low absorption coefficient of ε=170 $M^{-1}cm^{-1}$ at 532 nm. LO is a perylenediimide dye that has a much higher absorption coefficient with a peak ε=80,000 $M^{-1}cm^{-1}$ in organic solvents.[22] Using this absorption coefficient, we estimate that $\varepsilon\approx$8,000 $M^{-1}cm^{-1}$ at 532 nm after a blue shift of the absorption spectrum in nonpolar solvents is taken into account. However, LO also has a lower maximum solubility in eicosane, 0.23 mM as opposed to ≥100 mM for GAZ. Furthermore, with a fluorescence quantum yield of 0.99 in solution, we expect LO to be a less effective

photothermal agent. The fluorescence spectrum measured for a 0.23 mM LO-eicosane mixture resembled that of monomeric LO, with no sign of the excimer formation often seen in highly concentrated perylenediimide dye solutions (**Figure 5.4**).[23]

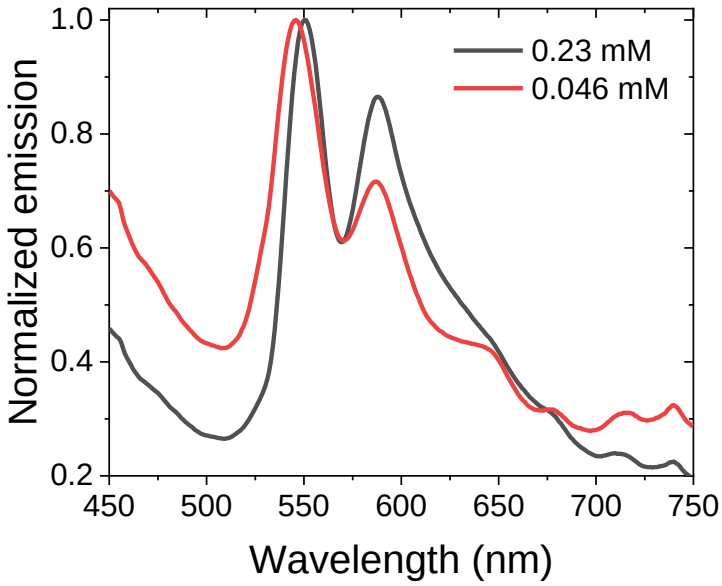

Figure 5.4 Normalized fluorescence spectra of LO-eicosane films. There is no sign of excimer formation despite increasing the concentration of LO 5x.

Eicosane mixtures were added to the actuator structure shown in **Figure 5.5**. One end was capped with a glass window, then the molten wax mixture was poured in. After the first wax filling solidified, extra wax was added to make sure the cylinder was completely filled. Then the silicone membrane was sealed on top of the filled cylinder. We found that moderate tightening in combination with butyl rubber O-rings was sufficient to prevent leaks. When the 250 mg eicosane plug was melted, its expansion could easily lift a 1.5 kg weight, which was the maximum that could be balanced on the vertically

oriented actuator. The actuator is shown in action in **Figure 5.5B-D**, where a 532 nm laser was used to melt a GAZ-eicosane mixture.

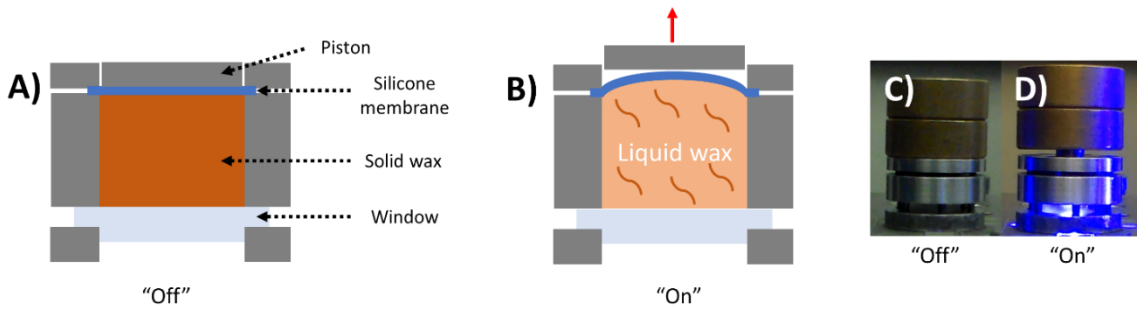

Figure 5.5 A) Schematic of the actuator in the "off" state. The cylinder and top and bottom plates are composed of aluminum, while the window on the bottom allows optical access to the wax. The top is sealed with a silicone membrane that pushes up an aluminum piston. **B)** In the "on" state, the wax is irradiated from the bottom and melts, expanding against the silicone membrane which pushes the piston upwards. Still images of the actuator with a 100 g weight in the **C)** "off" and **D)** "on" state.

With GAZ-eicosane mixture, the actuator could undergo 100 thermal expansion cycles with no loss in work output or leaking (**Figure 5.6**).

The actuator design in **Figure 5.5** has several advantages over the previous design. First, it was easier to fill due to the simple shape of the cylindrical cavity. Second, the silicone membrane was not damaged by the incoming laser light, unlike the black rubber boot of the earlier design. Finally, the simple geometry of the actuator and membrane force transducer makes it possible to compare the performance of our actuator to theoretical models described in the literature.[20,24]

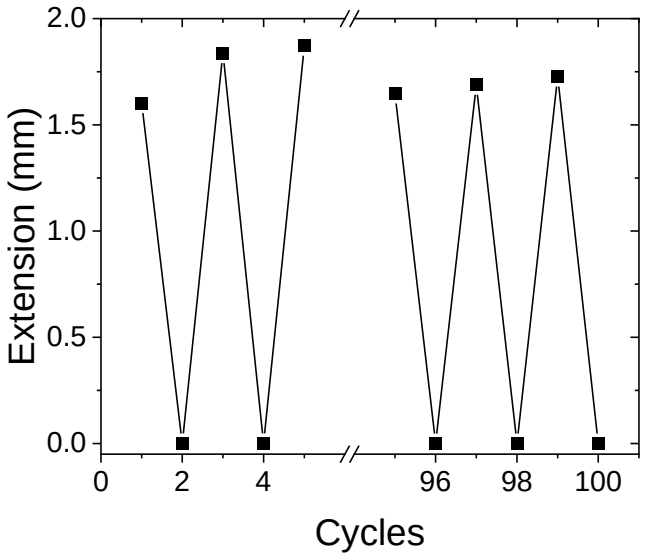

Figure 5.6 100 cycles of laser induced extension (laser on) followed by retraction (laser off) of the actuator.

The extension of the actuator depends on the force that is working against it, and integration of a force-extension curve is the standard way to evaluate work output. Given that eicosane undergoes a 15% expansion when it melts,[18] we expected to see a 15% height increase, corresponding to 1.0 mm on top of the 7 mm cylinder height. Instead, we consistently observed approximately 1.7 mm maximum displacement. As illustrated in **Figure 5.5a**, this additional vertical displacement reflects the fact that the silicone membrane cannot deform as a perfect cylinder, but rather as a parabola that compensates for its reduced lateral volume by increasing its height to accommodate the full wax expansion. The expanding wax must generate enough force to both distort the silicone membrane and lift the weight placed on top of it. We measured the force-displacement curve of the membrane in a separate experiment (**Figure 5.7**). The maximum membrane

force was on the order of 0.2 N, much less than the gravitational force due to the weight on top of the membrane.

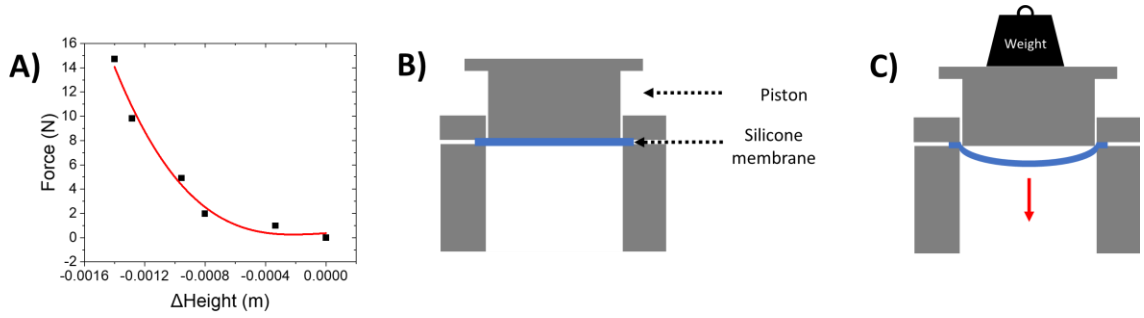

Figure 5.7 A) The contraction of the piston with increasing weight load was plotted versus $Force_{gravity}$. The data was fitted with a cubic function, $F(x)=A+Bx+Cx^3$ where Force F is a function of piston contraction x. **B)** The partially assembled actuator with a piston resting on the taut membrane. **C)** Membrane deforms downwards when weight is placed on the piston because the weight is pushing the membrane down.

The sum of these two forces gave the total force generated by the wax at a given vertical displacement X_{max}. The resulting force versus X_{max} data was linear, as shown in **Figure 5.8**, and this allowed us to determine a work output of 0.038 J and a stop force of 39 N (4 kg) for this device. To obtain the full work output, it was important to ensure the device was completely filled. If incomplete filling left free volume inside the cylinder, the wax expansion would fill these voids instead of pushing up the membrane, leading to smaller extensions. As shown in **Figure 5.8**, incomplete filling resulted in data that had the same slope but with smaller extensions due to some of the wax expansion filling up void spaces rather than deforming the membrane.

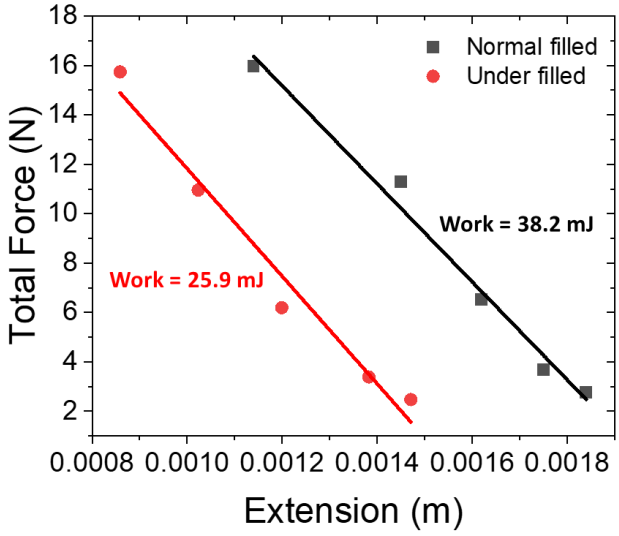

Figure 5.8 Force versus extension curves of an actuator that is completely filled with wax (black line) and an under-filled actuator (red line). The behavior of the actuators is similar (indicated by the slopes within error from one another), but the work output and stop forces differ due to the smaller extension in the under-filled actuator.

Given the work output and volume of wax inside the cylinder, we calculated an experimental work density of 0.12 MJ m^{-3}, comparable to our previous results of 0.14 MJ m^{-3} but considerably lower than the value of 3 MJ m^{-3} predicted by a theoretical analysis of the same actuator geometry (**Section 5.6.1**). The reasons for this discrepancy are not clear. We have already determined that the membrane resistance did not consume a significant fraction of the work output. Another possible explanation is that the theory does not take into account the possibility that the wax modulus or density can change with temperature and pressure. We have not been able to find a thermodynamic analysis of the ultimate reversible work limit for an expanding liquid wax, but such an analysis might provide insight on whether very high work densities can actually be attained

experimentally. It should be noted that the work densities reported here are comparable to or larger than values reported in the literature.[25–28]

The work output and maximum extension of the actuator are independent of how the wax is melted. They only depend on the properties of the eicosane and actuator. However, the dynamics of the actuation do depend on how heat is put into the system. Since the extension relies on a phase change, its dynamics will not follow simple first-order (exponential) kinetics in general. In order to quantify the actuator performance, we use a sigmoidal function to describe the time-dependent extension *X(t)*:

$$X(t) = \frac{1}{1 - \exp\left[-\frac{(t - \tau_{on})}{\tau_{rise}}\right]} \tag{1}$$

Here τ_{on} is the time when the extension has reached its halfway point and τ_{rise} determines how quickly this transition occurs, or the sharpness of the sigmoidal rise. We can define an effective extension time τ_{ext} for the actuator based on these parameters,

$$\tau_{ext} = \tau_{on} + \tau_{rise} \tag{2}$$

Figure 5.9 shows a typical X(t) curve during laser irradiation, along with a fit using Equation (1). After the laser is turned off, the piston retracts as the eicosane resolidifies. This motion can also be described by a sigmoidal function of the form

$$X(t) = \frac{1}{1 + \exp\left[-\frac{(t - \tau_{off})}{\tau_{fall}}\right]} \tag{3}$$

Equation (3) allows us to define an effective retraction time τ_{ret}:

$$\tau_{ret} = \tau_{off} + \tau_{fall} \tag{4}$$

Finally, the sum $\tau_{ext}+\tau_{ret}$ defines an effective cycling time for the actuator.

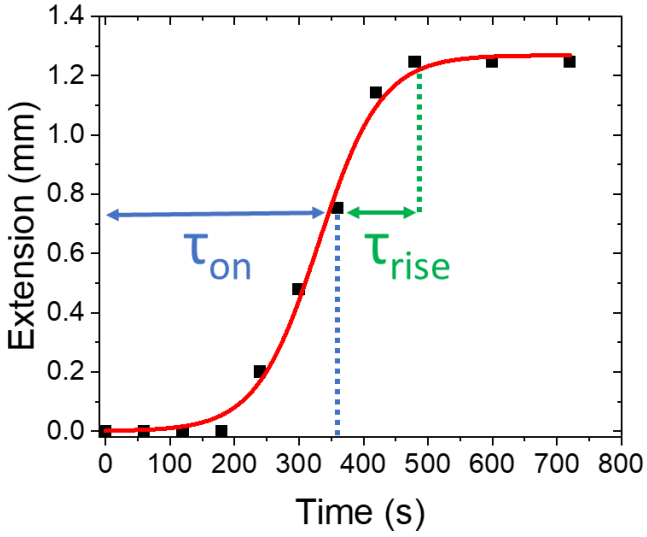

Figure 5.9 Extension versus time for an actuator is filled with pure eicosane (black squares) along with a fit to the data using Equation (1) in the text.

Using Equations (1)-(4), we characterized the on-off dynamics using five different heating methods:

A) pure eicosane that is heated by 10 W passed through a 150 Ω resistor attached to the bottom aluminum cap using heat-sink compound. The aluminum cap holds the glass window, which is in contact with the eicosane.

B) pure eicosane under 2 W of 532 nm irradiation that is incident on a black aluminum plate in contact with the eicosane. The black aluminum plate has replaced the glass window in **Figure 5.5A**.

C) pure eicosane irradiated by 2 W of 532 nm laser light that passes through the glass window into the wax chamber.

D) eicosane with 20 mM GAZ absorber irradiated by 2 W of 532 nm laser light that passes through the glass window into the wax chamber.

E) eicosane with 0.23 mM LO absorber irradiated by 2 W of 532 nm laser light that passes through the glass window into the wax chamber.

Method A) is the standard way to melt wax through resistive heating. Note that 10 W of electrical power was required to obtain a response time comparable to the laser-powered actuators. For 2 W of electrical power, no melting or actuation was observed, presumably because of thermal losses through the large resistor and the actuator casing. Methods B) and C) rely on absorption by an external black plate or the interior of the metal cylinder to heat the wax. In both cases, heat transfer to the wax must occur at a metal-wax interface. Methods D) and E), on the other hand, allow the laser light to be directly deposited into the wax interior, although some fraction of the incident light is probably scattered and absorbed by the cylinder walls. The τ_{ext} and τ_{ret} times are summarized in **Table 5.1** for all five Methods.

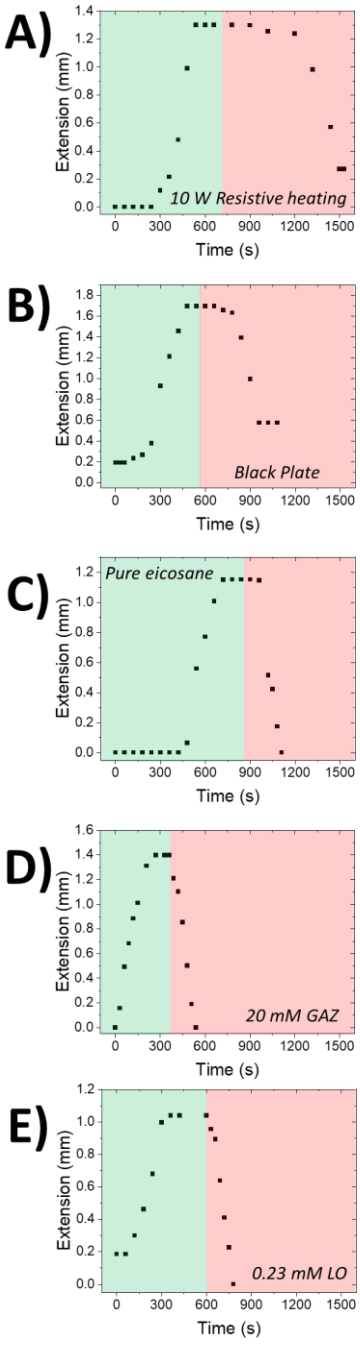

Figure 5.10 Extension and retraction dynamics of Method **A)** 10 W resistive heating; Method **B)** laser irradiation of a black aluminum plate; Method **C)** laser irradiation of pure eicosane through a window, Method **D)** laser irradiation of 20 mM GAZ-eicosane mixture through a window, and Method **E)** laser irradiation of 0.23 mM LO-eicosane through a window. The green portion of the graph indicates when the laser is on, while the red portion indicates when the laser is off.

From **Figure 5.10** and **Table 5.1**, we can see that applying heat to the actuator exterior, either by resistive heating or laser absorption, results in relatively slow extensions, τ_{ext}=480 s and 410 s, respectively. Allowing the laser light to enter the eicosane chamber without an absorbing dopant result in an even longer τ_{ext} =603 s. In this method, the incoming light is scattered by the undoped eicosane and some fraction is absorbed by the aluminum casing. The eicosane is then melted by thermal diffusion from the casing back into the wax, so it is no surprise that this indirect process takes the longest to melt the wax. The use of GAZ and LO absorbers shorten the extension times to τ_{ext} =137 s and τ_{ext} =295 s, respectively. When the input power is turned off and the piston is allowed to retract, there is an even more dramatic difference between the Methods. Methods A-C have much longer τ_{ret} values than D and E. We suspect that the slower recovery for Methods A-C reflects the fact that the actuator casing must heat up before the heat flows to the wax. Thus, there is more heat contained in the casing, which must be dissipated before the wax can cool. In Methods D and E, on the other hand, the wax is directly heated, and the casing can remain at a lower temperature, so the cooling and resolidification can occur more rapidly.

Table 5.1 Tabulated τ_{ext} and τ_{ret} values for Methods **A)-E)** as obtained from fits to Equations (1) and (3).

Method	**τ_{ext} (s)**	**τ_{ret} (s)**
A. 10 W resistive heating	480±10	1500±30
B. Black aluminum plate	410±30	990±30
C. Pure eicosane	600±10	1050±10
D. 20 mM GAZ	140±10	490±10
E. 0.23 mM LO	300±30	740±10

The fastest overall response is found for Method D using GAZ as the absorber. This is perhaps not surprising, since it has the highest optical density with an absorption depth of 0.02 cm versus 0.5 cm for LO, as well as the highest internal conversion yield. What is more surprising is that LO also performs reasonably well, even though the majority of absorbed photon energy is re-emitted as fluorescence and not heat. Based on the absorption, Stokes shift, and quantum yield, we estimate that it should only deposit 15% the heat that GAZ deposits in the wax (**Section 5.6.2**). However, it is possible that much of the fluorescence is absorbed by the metal walls of the actuator, providing an alternative path for heat transfer to the wax. It is also possible that there is some amount of intermolecular energy transfer and quenching at these concentrations, which would decrease the fluorescence quantum yield and increase heating of the surrounding matrix. The exact mechanism of LO's heating effect requires further investigation.

It is instructive to estimate the lower limit for τ_{ext} given our 2 W of laser input. Given 250 mg of eicosane with a heat capacity Cp= 1.9 J g^{-1} K^{-1}, an enthalpy of fusion

ΔH_{fus}=70 kJ mol^{-1}, and a melting point of 38°C,[29] we calculate that 68 J is required to completely melt the wax plug if heating starts from 25°C. If we assume that the 2 W of input power only heats the eicosane with no thermal or optical losses, the fastest possible melting time is 34 s (**Section 5.6.3**). Our results indicate that our reported melt times are at least 4 times slower than what is theoretically possible, so the response time is not currently limited by the input laser power.

5.5 Conclusion

In this chapter, we have explored the properties and performance of light-powered wax motors. Using a simple actuator geometry, we measured force-displacement curves for eicosane-GAZ blends, finding that the work density of 0.12 MJ m^{-3} can be maintained for 100 cycles. The main advantage of using small molecule absorbers dissolved in the wax is that they enable faster heating and cooling which improves the dynamic response of the motor. The response is still slow, on the timescale of minutes, but it should be straightforward to decrease the response time by employing higher laser powers. The fact that a perylenediimide dye can also give rise to the laser-induced expansion suggests that chromophores that are extremely photostable can be used as photothermal agents. Overall, direct laser heating of the wax through embedded absorbers has clear advantages in terms of response time and input power requirements. It should be emphasized that this actuator concept is still in its early stages of development, and there is still much room to improve figures-of-merit like response speed and work output.

5.6 Calculations for wax actuator

5.6.1 Theoretical work density of wax motors

Using the equations to calculate the work generated from a wax actuator from Srinivasan and Spearing,[20] the following equations and glossary are presented:

Bulk modulus of liquid (wax)	k	1.6	GPA
Elastic modulus of solid (wax)[30]	E	63.2×10^3	MPA
Allowable volumetric strain	ε_{rec}	15	%
Thickness of membrane	h_d	0.5	mm
Height of cavity	h_c	8	mm
Radius of cavity	R	3.545	mm
Block force	F_{block}		N
Average displacement	$d_{average}$		m
Work	W		J

$$d_{average} = \frac{\varepsilon_{rec} R^2}{h_d}\sqrt{\frac{2k}{E}} \tag{5}$$

$$F_{block} = \pi R^2 \varepsilon_{rec} k \tag{6}$$

$$W = \frac{F_{block} d_{average}}{8\pi R^2 h_c} \tag{7}$$

From the equations above, the theoretical maximum work attainable (with actuator dimensions from this work) is **3.2 MJ m^{-3}**.

5.6.2 Calculations for heat generation from internal conversion from LO

The amount of heat generated from irradiating 250 mg of the 0.23 mM LO-eicosane mixture is calculated from the following equations:

$$E_{stoke\ shift} = \frac{hc}{\lambda_{abs\ max}} - \frac{hc}{\lambda_{fl}} \tag{8}$$

$$E_{laser\ wavelength} = \frac{hc}{\lambda_{laser\ wavelength}} \tag{9}$$

$$Stoke\ shift\ scaling\ factor = \frac{E_{stoke\ shift}}{E_{laser\ wavelength}} \quad (10)$$

Here, h is Planck's constant and c is the speed of light. The total energy E_{total} is calculated by multiplying the laser input power (2 W) and τ_{ext} (**Table 5.1**). The heat generated from the stoke shift (**Figure 5.11**) can be calculated by *Stoke shift scalar*×E_{total}. So the conversion of photons to heat via internal conversion in LO is expressed as (1-φ_{fl})E_{total}+(*Stoke shift scalar*×E_{total}).

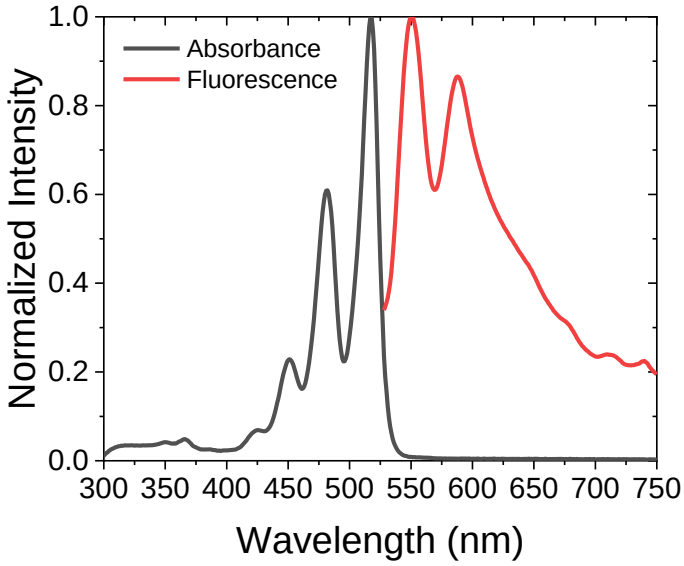

Figure 5.11 The absorbance of liquid (black) and solid film fluorescence (red) of 0.23 mM LO-eicosane are show. $\lambda_{abs\ max}$=518 nm and λ_{fl}=551 nm.

$\lambda_{abs\ max}$	518	nm
λ_{fl}	551	nm
$\lambda_{laser\ wavelength}$	532	nm
φ_{fl}[22]	0.99	

From the above equations, the energy from internal conversion for LO is **42.2 J**. The same calculation can be done for GAZ, but it is worth noting GAZ has an internal conversion

efficiency of 100% when excited to S_1, so E_{total} = energy of internal conversion. GAZ yields **274 J**, so LO produces **15.4%** of the heat that GAZ produces.

5.6.3 Theoretical time limit for photomelting of wax

From the main text, eicosane with heat capacity Cp=1.9 J g^{-1} K^{-1}, ΔH_{fus}=70 kJ mol^{-1}, and a Δ13 K, we calculated the amount of energy required to melt 250 mg of eicosane. Calculating the amount of energy required to raise eicosane 13 K is as follows:

$$1.9\ \frac{J}{g\ K} \times 0.250\ g \times 13\ K = \mathbf{6.175\ J}$$

Calculating the amount of energy required to melt eicosane is as follows:

$$70{,}000\ \frac{J}{mol} \times 0.250\ g \times \frac{1}{282.55}\frac{mol}{g} = \mathbf{61.94\ J}$$

So, the total amount of energy needed to melt eicosane from 25-38°C is **68.11 J**.

5.7 References

(1) Kim, T.; Zhu, L.; Al-Kaysi, R. O.; Bardeen, C. J. Organic Photomechanical Materials. *ChemPhysChem* **2014**, *15* (3), 400–414. https://doi.org/10.1002/cphc.201300906.

(2) Tong, F.; Kitagawa, D.; Bushnak, I.; Al-Kaysi, R. O.; Bardeen, C. J. Light-Powered Autonomous Flagella-Like Motion of Molecular Crystal Microwires. *Angewandte Chemie - International Edition* **2021**, *60* (5), 2414–2423. https://doi.org/10.1002/ANIE.202012417.

(3) Dong, X.; Tong, F.; M. Hanson, K.; O. Al-Kaysi, R.; Kitagawa, D.; Kobatake, S.; J. Bardeen, C.; Hanson, K. M.; Al-Kaysi, R. O.; Kitagawa, D.; Kobatake, S.; Bardeen, C. J. Hybrid Organic-Inorganic Photon-Powered Actuators Based on Aligned Diarylethene Nanocrystals. *Chemistry of Materials* **2019**, *31* (3), 1016–1022. https://doi.org/10.1021/acs.chemmater.8b04568.

(4) Tong, F.; Xu, W.; Al-Haidar, M.; Kitagawa, D.; Al-Kaysi, R. O.; Bardeen, C. J. Photomechanically Induced Magnetic Field Response by Controlling Molecular Orientation in 9-Methylanthracene Microcrystals. *Angewandte Chemie International Edition* **2018**, *57* (24), 7080–7084. https://doi.org/https://doi.org/10.1002/anie.201802423.

(5) Tong, F.; Xu, W.; Guo, T.; Lui, B. F.; Hayward, R. C.; Palffy-Muhoray, P.; Al-Kaysi, R. O.; Bardeen, C. J. Photomechanical Molecular Crystals and Nanowire Assemblies Based on the [2+2] Photodimerization of a Phenylbutadiene Derivative. *J Mater Chem C Mater* **2020**, *8* (15), 5036–5044.

(6) Xu, T. Y.; Tong, F.; Xu, H.; Wang, M. Q.; Tian, H.; Qu, D. H. Engineering Photomechanical Molecular Crystals to Achieve Extraordinary Expansion Based on Solid-State [2 + 2] Photocycloaddition. *J Am Chem Soc* **2022**, *144* (14), 6278–6290. https://doi.org/10.1021/jacs.1c12485.

(7) Ikeda, T.; Mamiya, J. I.; Yu, Y. Photomechanics of Liquid-Crystalline Elastomers and Other Polymers. *Angewandte Chemie - International Edition* **2007**, *46* (4), 506–528. https://doi.org/10.1002/anie.200602372.

(8) McDermott, E. J.; Wirnhier, E.; Schnick, W.; Virdi, K. S.; Scheu, C.; Kauffmann, Y.; Kaplan, W. D.; Kurmaev, E. Z.; Moewes, A. Band Gap Tuning in Poly(Triazine Imide), a Nonmetallic Photocatalyst. *Journal of Physical Chemistry C* **2013**, *117* (17), 8806–8812. https://doi.org/10.1021/jp4002059.

(9) Xu, W. C.; Sun, S.; Wu, S. Photoinduced Reversible Solid-to-Liquid Transitions for Photoswitchable Materials. *Angewandte Chemie - International Edition* **2019**, *58* (29), 9712–9740. https://doi.org/10.1002/anie.201814441.

(10) Oliver, A. D.; Vigil, S. R.; Gianchandani, Y. B. Photothermal Surface-Micromachined Actuators. *IEEE Trans Electron Devices* **2003**, *50* (4), 1156–1157. https://doi.org/10.1109/TED.2003.812505.

(11) Han, B.; Zhang, Y. L.; Chen, Q. D.; Sun, H. B. Carbon-Based Photothermal Actuators. *Adv Funct Mater* **2018**, *28* (40), 1–23. https://doi.org/10.1002/adfm.201802235.

(12) Kuenstler, A. S.; Kim, H.; Hayward, R. C. Liquid Crystal Elastomer Waveguide Actuators. *Advanced Materials* **2019**, *31* (24), 1901216. https://doi.org/10.1002/adma.201901216.

(13) Liang, J.; Xu, Y.; Huang, Y.; Zhang, L.; Wang, Y.; Ma, Y.; Li, F.; Guo, T.; Chen, Y. Infrared-Triggered Actuators from Graphene-Based Nanocomposites. *Journal of Physical Chemistry C* **2009**, *113* (22), 9921–9927. https://doi.org/10.1021/jp901284d.

(14) Ma, H.; Xiao, X.; Zhang, X. Recent Advances for Phase-Transition Materials for Actuators. *J. Appl. Phys* **2020**, *128*, 101101. https://doi.org/10.1063/5.0020596.

(15) Verpaalen, R. C. P.; Varghese, S.; Froyen, A.; Pilz da Cunha, M.; Pouderoijen, M. J.; Severn, J. R.; Bhatti, M. R.; Peijs, T.; Bastiaansen, C. W. M.; Debije, M. G.; Engels, T. A. P.; Schenning, A. P. H. J. Fast, Light-Responsive, Metal-Like Polymer Actuators Generating High Stresses at Low Strain. *Matter* **2020**, *2* (6), 1522–1534. https://doi.org/10.1016/j.matt.2020.03.001.

(16) Li, Z.; Myung, N. V.; Yin, Y. Light-Powered Soft Steam Engines for Self-Adaptive Oscillation and Biomimetic Swimming. *Sci Robot* **2021**, *6* (61), eabi4523. https://doi.org/10.1126/scirobotics.abi4523.

(17) Shahsavan, H.; Aghakhani, A.; Zeng, H.; Guo, Y.; Davidson, Z. S.; Priimagi, A.; Sitti, M. Bioinspired Underwater Locomotion of Light-Driven Liquid Crystal Gels. *Proc Natl Acad Sci U S A* **2020**, *117* (10), 5125–5133. https://doi.org/10.1073/pnas.191795211.

(18) Templin, P. R. Coefficient of Volume Expansion for Petroleum Waxes and Pure N-Paraffins. *Ind Eng Chem* **1956**, *48* (1), 154–161. https://doi.org/10.1021/ie50553a043.

(19) Lui, B. F.; Bardeen, C. J. Using Small Molecule Absorbers to Create a Photothermal Wax Motor. *Small* **2021**, *2105356*, 1–7. https://doi.org/10.1002/smll.202105356.

(20) Srinivasan, P.; Spearing, S. M. Material Selection for Optimal Design of Thermally Actuated Pneumatic and Phase Change Microactuators. *Journal of*

Microelectromechanical Systems **2009**, *18* (2), 239–249. https://doi.org/10.1109/JMEMS.2009.2013385.

(21) Do, J. Y.; Son, N.; Shin, J.; Chava, R. K.; Joo, S. W.; Kang, M. N-Eicosane-Fe3O4@SiO2@Cu Microcapsule Phase Change Material and Its Improved Thermal Conductivity and Heat Transfer Performance. *Mater Des* **2021**, *198*, 109357. https://doi.org/10.1016/j.matdes.2020.109357.

(22) Sanguineti, A.; Sassi, M.; Turrisi, R.; Ruffo, R.; Vaccaro, G.; Meinardi, F.; Beverina, L. High Stokes Shift Perylene Dyes for Luminescent Solar Concentrators. *Chemical Communications* **2013**, *49* (16), 1618–1620. https://doi.org/10.1039/C2CC38708E.

(23) Al-Kaysi, R. O.; Sang Ahn, T.; Müller, A. M.; Bardeen, C. J. The Photophysical Properties of Chromophores at High (100 MM and above) Concentrations in Polymers and as Neat Solids. *Physical Chemistry Chemical Physics* **2006**, *8* (29), 3453–3459. https://doi.org/10.1039/b605925b.

(24) Ogden, S.; Klintberg, L.; Thornell, G.; Hjort, K.; Bodén, R. Review on Miniaturized Paraffin Phase Change Actuators, Valves, and Pumps. *Microfluid Nanofluidics* **2014**, *17* (1), 53–71. https://doi.org/10.1007/s10404-013-1289-3.

(25) Mann, A.; Germann, T.; Ruiter, M.; Groche, P. The Challenge of Upscaling Paraffin Wax Actuators. *Mater Des* **2020**, *190*, 108580. https://doi.org/10.1016/J.MATDES.2020.108580.

(26) Liu, B.; Yang, J.; Zhang, Z.; Yang, J.; Li, D. A Phase Change Microactuator Based on Paraffin Wax/Expanded Graphite/Nickel Particle Composite with Induction Heating. *Sens Actuators A Phys* **2018**, *275*, 129–136. https://doi.org/https://doi.org/10.1016/j.sna.2018.04.006.

(27) Klintberg, L.; Karlsson, M.; Stenmark, L.; Schweitz, J.-Å.; Thornell, G. A Large Stroke, High Force Paraffin Phase Transition Actuator. *Sens Actuators A Phys* **2002**, *96* (2), 189–195. https://doi.org/https://doi.org/10.1016/S0924-4247(01)00785-3.

(28) Qi, C.; Han, D.; Shinshi, T. A MEMS-Based Electromagnetic Membrane Actuator Utilizing Bonded Magnets with Large Displacement. *Sens Actuators A Phys* **2021**, *330*, 112834. https://doi.org/https://doi.org/10.1016/j.sna.2021.112834.

(29) van Miltenburg, J. Cees.; Oonk, H. A. J.; Metivaud, V. Heat Capacities and Derived Thermodynamic Functions of N-Nonadecane and n-Eicosane between 10 K and 390 K. *J Chem Eng Data* **1999**, *44* (4), 715–720. https://doi.org/10.1021/je980231+.

(30) Tesař, V.; Kordík, J. Melting N-Eicosane in Scaled-up Model of Capsule for Use in Hot Climate Thermal-Comfort Garments. *EPJ Web Conf* **2019**, *213*, 02086. https://doi.org/10.1051/epjconf/201921302086.

6. Conclusion and Outlook

6.1 Conclusion

Two methods were discussed to promote a solid→solid or solid→liquid phase transition using light: a photochemical reaction and the photothermal effect. In Chapter 3, the photochemistry of a novel photoswitch, DASA, was discussed. DASA is a photochromic molecule with numerous attractive properties such as reversible photochemistry, negative photochromism, and large polarity and molecular volume changes. It was reported that DASA's photochemistry is inhibited at high concentrations in both solid and liquid mediums, which limit the usage of this molecule as a photomechanical material. This inhibition of DASA's chemistry must be understood and remedied so that future generations of DASA photoswitches could be incorporated in the chemist's photomechanical toolbox.

In Chapters 4 and 5, alkane solids such as waxes were discussed as solid→liquid photomechanical phase change materials (PCMs). Traditionally, waxes are melted using convection or resistive heating, techniques which both require electricity. Here in this thesis, light is used to melt a low molecular weight wax, eicosane ($C_{20}H_{42}$), eliminating the need for electrical heaters. Although only eicosane has been discussed, in principle any alkane wax can be used as the active PCM. Doping waxes with small molecule absorbers allow the waxes to absorb incident photons and convert light into heat through the photothermal effect. These small molecule-wax composites were then incorporated inside wax actuators, which are built and designed in our lab. The work output, temporal response,

cyclability, and stability of the actuators were benchmarked, and it was demonstrated that our wax motors performed better in all categories listed above compared to similar devices in the literature. However, studies are still ongoing to further improve the work output and response times of such devices to match theoretical limitations.

It has been shown that light activated PCMs are effective candidates in the regime of photomechanical materials. Through the use of such PCMs, the need for physical connections to deliver power to traditional piston-type motors is no longer required due to the ability for these materials to transform photons directly into a volume expansion, which is then harnessed for mechanical work. The development of these new smart materials provide a way to create scalable actuators and devices which have higher energy densities compared to similar existing devices, like piezoelectrics and other soft actuators.

6.2 Outlook: photochemical solid→liquid phase change materials

Despite the photothermal effect being an effective method for inducing a solid→liquid phase change, it still relies on thermal diffusion to propagate the transformation. This may limit applications in situations where it may be difficult to deliver heat or electricity to a system, like underwater or in outer space. As discussed in Chapter 1, a photochemical reaction circumvents this problem: photomechanochemistry uses light to elicit a mechanical response in a material through photochemistry. In other words, heat diffusion is not the driving force here. There are a variety of commercially available azobenzene-based solid→liquid photochromes used as adhesives,[1–3] but the one that will be discussed here is (E)-1-(4-(dodecyloxy)-3-methylphenyl)-2-(4-(dodecyloxy)phenyl)diazene (referred to as AZO, **Figure 6.1a**).

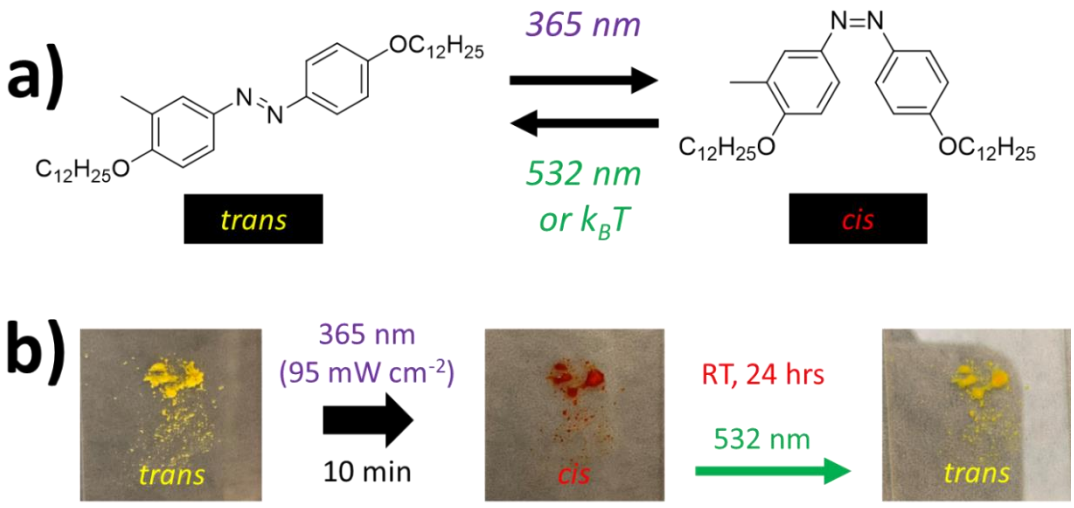

Figure 6.1 a) Schematic of AZO's trans-cis isomerization. **b)** Upon irradiation with UV light, *trans* AZO converts to *cis* AZO, which is a liquid at room temperature. Heat or Visible light will revert *cis* AZO back to the *trans* isomer.

AZO's photochemistry is similar to that of neat azobenzene in that it undergoes reversible trans-cis isomerization.[4] However, due to the methyl group disrupting the π-π interactions in the molecular crystal, it is capable of liquefying at room temperature when irradiated with UV light (**Figure 6.1b**).[2] Experiments are still in progress to quantitatively determine the volume change of this isomerization, but preliminary evidence indicates that the *cis* variant is less dense than the *trans* isomer. We hypothesize that we can use the volume expansion of AZO and similar photochromes to drive photomechanical work as we did with the small molecule-wax composites. Photoactive polymers have been used to demonstrate photomechanical behavior in the past,[5–7] and the incorporation of AZO in a polymer host is no different.

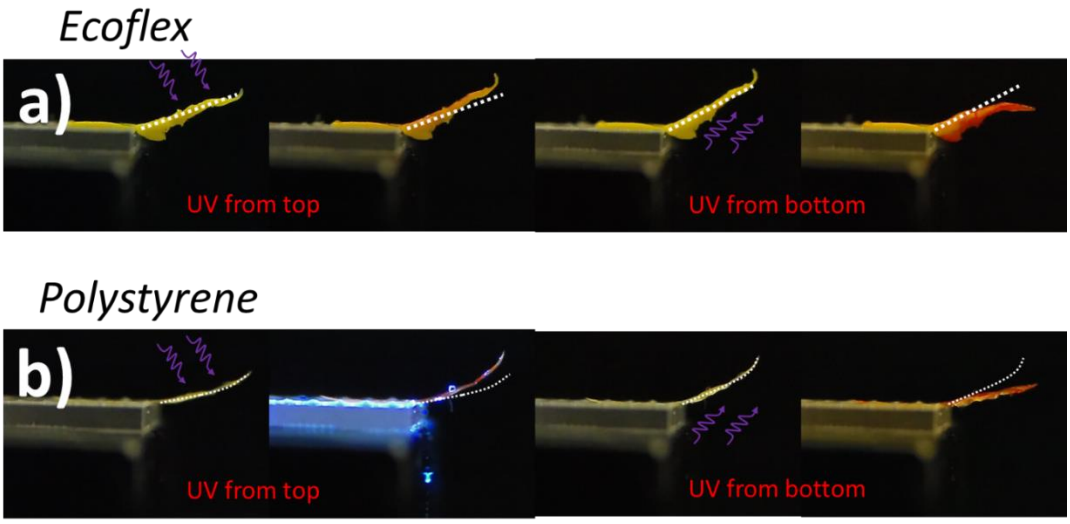

Figure 6.2 20% w/w loading of AZO in an **a)** Ecoflex and a **b)** polystyrene host. In both cases, the polymer bends towards the direction of illumination. The white dotted line denotes the initial starting position of the polymer strip.

Figure 6.2 shows the photomechanical behavior of the AZO-doped polymers bending upon photoisomerization from the *trans* to *cis* isomer. Two different polymer hosts, Ecoflex and polystyrene are shown, though this photomechanical behavior can also be demonstrated in other polymers like polymethylmethacrylate (PMMA), polyvinyl alcohol (PVA), and polyvinylidene fluoride (PVDF). The incorporation of AZO inside a variety of polymers turn them into photoactive polymers, suggesting that this could be a low cost, processable, and general way of creating photomechanical polymers. As shown in **Figure 6.2**, the polymers bend towards the direction of illumination, however the polymer strips do not recapture their initial geometry despite the cis→trans back reaction, other than PVDF. PVDF is the only polymer that is mechanically cyclable, as shown in **Figure 6.3**. The mechanism of bending of these photoactive polymers is still being studied,

but the color change suggests that the photochemistry is not affected by the polymer host. The mechanical response of the polymer and the photochemistry of AZO appear to be decoupled in certain polymer hosts, but the proof-of-concept of photochemical solid→liquid phase change producing mechanical work in polymers is still demonstrated.

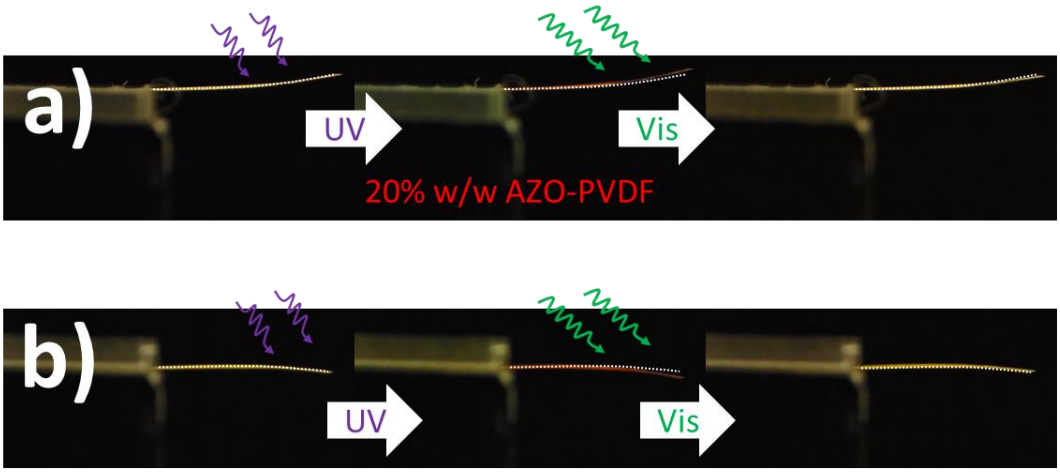

Figure 6.3 20% w/w loading of AZO in PVDF. **a)** The composite is irradiated from the top with UV light and the film bends upwards, but upon irradiation with visible light (from the top) the film defaults to its initial shape. **b)** The same film is shown but flipped upside down. The film is irradiated with UV from the top once again but bends downwards this time. Upon irradiation with visible light from the top, the film resets to its initial state, indicating that the bending is insensitive to the direction of illumination. The white dotted line denotes the initial starting position of the polymer strip.

Though this work is still in the preliminary stages, this sets the foundation to graduate from photothermal actuation to photochemical actuation. There are still some issues that need to be addressed for this method to become viable, such as addressing the optical penetration of these materials and positive photochromism, the response times of actuation and kinetics of the photochemistry, and the possibility of utilizing a different photochrome

which does not require UV photons to initiate the chemistry. Nevertheless, photochemical solid→liquid PCMs can be used in photomechanical actuation.

6.3 References

(1) Norikane, Y.; Uchida, E.; Tanaka, S.; Fujiwara, K.; Nagai, H.; Akiyama, H. Photoinduced Phase Transitions in Rod-Shaped Azobenzene with Different Alkyl Chain Length. *Journal of Photopolymer Science and Technology* **2016**, *29* (1), 149–157. https://doi.org/10.2494/PHOTOPOLYMER.29.149.

(2) Norikane, Y.; Uchida, E.; Tanaka, S.; Fujiwara, K.; Koyama, E.; Azumi, R.; Akiyama, H.; Kihara, H.; Yoshida, M. Photoinduced Crystal-to-Liquid Phase Transitions of Azobenzene Derivatives and Their Application in Photolithography Processes through a Solid-Liquid Patterning. *Org Lett* **2014**, *16* (19), 5012–5015. https://doi.org/10.1021/ol502223u.

(3) Blelloch, N. D.; Yarbrough, H. J.; Mirica, K. A. Stimuli-Responsive Temporary Adhesives: Enabling Debonding on Demand through Strategic Molecular Design. *Chem Sci* **2021**, *12* (46), 15183–15205. https://doi.org/10.1039/D1SC03426J.

(4) Hartley, G. S. The Cis-Form of Azobenzene. *Nature* **1937**, *140* (3537), 281. https://doi.org/10.1038/140281a0.

(5) Ikeda, T.; Mamiya, J. I.; Yu, Y. Photomechanics of Liquid-Crystalline Elastomers and Other Polymers. *Angewandte Chemie - International Edition* **2007**, *46* (4), 506–528. https://doi.org/10.1002/anie.200602372.

(6) Matějka, L.; Ilavský, M.; Dušek, K.; Wichterle, O. Photomechanical Effects in Crosslinked Photochromic Polymers. *Polymer (Guildf)* **1981**, *22* (11), 1511–1515. https://doi.org/10.1016/0032-3861(81)90321-9.

(7) Hu, J.; Ma, S.; Yu, H.; Li, Q. Photomechanical Soft Nanocomposites: Synergies Between Soft Matrix and Energy Conversion Additives. In *Photoactive Functional Soft Materials*; 2019; pp 285–317. https://doi.org/10.1002/9783527816774.ch8.